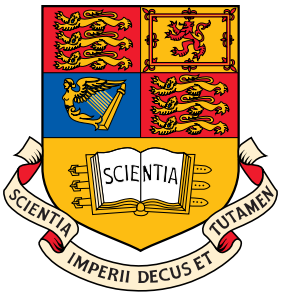
Linear feedback control for form-drag reduction on bluff bodies with a blunt trailing edge

Jeremy Dahan

Department of Aeronautics

Imperial College London



A dissertation submitted for the degree of

Doctor of Philosophy

January 2013

Abstract

The work described in this thesis is a computational investigation applying linear feedback control to reduce form-drag on bluff bodies with a blunt trailing edge. For such bodies, a large portion of the aerodynamic drag is associated with an unsteady separated region or wake downstream of the body. The development of tractable feedback strategies to control unsteady wakes promises strong benefits, both in terms of industrial applications and for furthering our understanding of the flow mechanisms at play.

For this purpose, large-eddy simulations are carried out where a linear feedback controller targets an increase in the mean pressure force on the rear (base) of the body. The flows over two distinct geometries are examined: a backward-facing step and a bluff body with a rounded leading edge, often referred to as a D-shaped body. The control is effected by zero-net-mass-flux slot jets, responding to sensors located on the body base. Open-loop characterization provides information on the effects of actuation and some physical insight into the relation between the base pressure and wake dynamics. System identification is used to obtain a low-order model of the flow's response to actuation that can be used for control.

The control strategy is based on the premise that reducing the fluctuations in the near-wake will cause an increase in the mean base pressure, hence a reduction in form-drag. The controllers are designed with classical frequency-domain methods, using a sensitivity transfer function to attenuate the size of the pressure force fluctuations.

The influence of parameters such as the Reynolds number and the location and type of actuators is studied. For all cases, low-order linear feedback controllers successfully reduce the pressure force fluctuations and achieve sensible drag reductions. They do so with higher efficiency than the open-loop forcing considered. Uncertainties in the model and flow conditions can be to some extent mitigated by the robustness of the controller. The results support the conjecture linking the fluctuating and mean base pressure, although it is observed that further work is needed before such an approach can be used for optimization.

The copyright of this thesis rests with the author and is made available under a Creative Commons Attribution Non-Commercial No Derivatives licence. Researchers are free to copy, distribute or transmit the thesis on the condition that they attribute it, that they do not use it for commercial purposes and that they do not alter, transform or build upon it. For any reuse or redistribution, researchers must make clear to others the licence terms of this work.

Preface

The work presented in this dissertation is the result of my own research and I have endeavoured to acknowledge prior contributions. The findings reported throughout this thesis have been presented at four international conferences and the results described in chapters 6 and 7 have been published in the *Journal of Fluid Mechanics* (Dahan et al. [28]).

I would like to express my profound gratitude to my supervisor, Dr Aimee Morgans, for her support, patience and encouragements in guiding me through this project. Her diligent approach to research has been helpful and inspiring. My thanks also go to Dr Sylvain Lardeau for introducing me to StreamLES and for many fruitful discussions on numerical fluid dynamics.

This work also benefited from discussions with Prof. Michael Leschziner, Dr Joaquim Peiro, Prof. Sergei Chernyshenko, Simon Burbidge and Dr Ning Li. Financial support from the EPSRC and travel grants from the Royal Academy of Engineering, the Royal Aeronautical Society and the Imperial College Trust are gratefully acknowledged.

I am indebted to the dwellers of the E256 office in the Department of Aeronautics (and 476 in Mechanical Engineering) for creating such a nice atmosphere and for their friendship.

This thesis is dedicated to my four constants: Gill, Albert, Laura & Ben.

Contents

1 Introduction **13**

1.1 Motivation 13

1.2 Overview 14

2 Relevant flow control issues **17**

2.1 Background 17

2.2 Flow control for bluff body drag reduction 17

2.3 Strategies for linear closed-loop flow control 19

2.3.1 Essential ingredients 19

2.3.2 Reduced-order modelling 20

2.3.3 Controller design 22

3 Numerical simulations **24**

3.1 Background 24

3.2 Governing equations for LES 25

3.2.1 Navier-Stokes equations 25

3.2.2 Scale separation 26

3.2.3 Leonard's decomposition 28

3.2.4 Schumann's approach 29

3.3 Subgrid-scale modelling 29

3.3.1 Background 29

3.3.2 Smagorinsky model 30

3.3.3 WALE model 31

3.3.4 Dynamic procedure 31

3.3.5 Implicit LES 32

3.4 LES applied to bluff body flows: a brief review . . . 33
3.5 LES solver . . . 35
3.5.1 Overview . . . 35
3.5.2 Spatial discretization . . . 36
3.5.3 Time-marching strategy . . . 38
3.5.4 Resolution of the Poisson equation . . . 40
3.5.5 Parallelization issues and boundary conditions . . . 41
3.5.6 Additions to the code . . . 43
3.5.7 Performance on parallel platforms . . . 43

4 Flows over 2D bluff bodies **45**
4.1 Main features of reattaching shear layers . . . 45
4.1.1 Near-separation region . . . 46
4.1.2 Recirculation bubble . . . 47
4.1.3 Reattachment . . . 49
4.1.4 Redeveloping boundary layer . . . 50
4.2 Flow instabilities . . . 50
4.3 Bluff body pressure drag mechanisms . . . 53
4.4 Review of actuation strategies . . . 54

5 Overview **56**
5.1 Description of test cases . . . 56
5.2 Actuation and sensing . . . 57
5.2.1 Actuators . . . 57
5.2.2 Sensors . . . 59
5.3 System identification and control . . . 60

6 Laminar backward-facing step **64**
6.1 Background . . . 64
6.2 Setup . . . 64
6.3 Flow description and validation . . . 65
6.4 Open-loop forcing . . . 68
6.4.1 Background . . . 68

6.4.2 Harmonic synthetic jet forcing . . . 68
6.4.3 System identification . . . 70
6.4.4 Momentum source . . . 73
6.5 Feedback control . . . 74
6.6 Summary . . . 77

7 Turbulent backward-facing step **78**
7.1 Background . . . 78
7.2 Inflow generation . . . 78
7.3 Computational domain and mesh . . . 81
7.4 Baseline flow . . . 85
7.4.1 Main time-averaged features . . . 86
7.4.2 Spectral analysis . . . 88
7.5 Open-loop forcing . . . 91
7.5.1 Physical insight . . . 91
7.5.2 System identification . . . 96
7.6 Closed-loop control . . . 99
7.6.1 Control synthesis . . . 99
7.6.2 Flow mechanisms . . . 101
7.7 Summary . . . 105

8 Reynolds number effects and flow mechanisms **106**
8.1 Background . . . 106
8.2 Grid resolution . . . 107
8.3 Baseline flow . . . 108
8.3.1 Time-averaged flow . . . 109
8.3.2 Spectral analysis and correlation . . . 110
8.3.3 Instantaneous pressure field . . . 113
8.4 Open-loop forcing . . . 114
8.4.1 Physical insight . . . 115
8.4.2 System identification . . . 116
8.5 Closed-loop control . . . 117
8.5.1 Control synthesis . . . 117

8.5.2 Flow mechanisms . . . 118
8.5.3 Efficiency considerations . . . 121
8.6 Summary . . . 123

9 D-shaped bluff body **124**
9.1 Background . . . 124
9.2 Grid resolution . . . 125
9.3 Baseline flow . . . 126
9.4 System identification and feedback control . . . 129
9.5 Summary . . . 132

10 Conclusions & outlook **134**
10.1 Summary . . . 134
10.2 Outlook . . . 135

List of Figures

2.1 Passive boat tail device to reduce form-drag and fuel consumption 18
2.2 Diagram of closed-loop flow control system. 19

3.1 LES filtering 27
3.2 LES of bluff body flows 34
3.3 Diagram of cell locations 37
3.4 Information exchange between two neighbouring blocks. 41
3.5 Scalability of the code, characteristic speedup curves 44

4.1 Schematic of flow downstream of a backward-facing step 46
4.2 Profiles of time-averaged streamwise velocity 47
4.3 Pressure coefficient along lower wall 48
4.4 RMS pressure fluctuations along lower wall 49

5.1 Computational domains and boundary conditions 57
5.2 Schematic of control configuration and dominant flow features for Ω_1. 58
5.3 Schematic of control configuration and dominant flow features for Ω_2. 58
5.4 Spatial averaging of base pressure fluctuations and discrete sensors 60
5.5 Frequency-domain control models 61

6.1 Main grid 65
6.2 Contours of time-averaged streamfunction Ψ. 65
6.3 Amplitude spectra of pressure along lower wall, upstream and downstream of reattachment 66
6.4 Phase-averaged contours of vorticity ω_z. 67
6.5 Phase-averaged distribution of pressure coefficient $C_P(y)$ on the step base . . . 67

6.6 Diagram of actuator locations for backward-facing step flow. Not to scale. . . . 68
6.7 Amplitude spectra for open-loop harmonic forcing 69
6.8 Contours of fractional change in time-averaged base pressure for actuator locations 1 and 2 70
6.9 Bode plots of frequency responses 71
6.10 Frequency response models for actuators 1 and 2 72
6.11 Measure of the quality of the fits against denominator order of the fitted transfer function. (•) Actuator 1 and (◦) actuator 2. 72
6.12 Frequency response for momentum forcing 74
6.13 Time series of sensor signal for two simple controllers 75
6.14 Characteristics of closed-loop systems and time-domain control results 76

7.1 Schematic of precursor boundary layer simulation with recycling 79
7.2 Time-averaged characteristics of precursor inflow boundary layer 81
7.3 Two-dimensional slice of the nominal grid 82
7.4 Characteristics of computational cells forming the grid and skin friction and wall pressure distributions 83
7.5 Flow profiles at separation compared to DNS data 84
7.6 Two-point spanwise correlation coefficients R_{uu} and R_{pp} 85
7.7 Time-averaged contours of flow properties and eddy viscosity 86
7.8 Second moments in the near-base flow compared to PIV data 87
7.9 Growth of the separated shear layer 88
7.10 Pressure spectra in the recirculation bubble 90
7.11 Effect of open-loop harmonic forcing on reattachment length and base pressure 92
7.12 Spectra of sensor signal with harmonic forcing 94
7.13 Flow characteristics downstream of separation for low-frequency and medium-frequency forcing 95
7.14 Bode plots of frequency responses for actuators 1 and 2 97
7.15 Characteristics of closed-loop systems for both actuator locations 100
7.16 Input and output signals for controller K_1 101
7.17 Input and output signals for controller K_2 102

7.18 Time-averaged flow characteristics downstream of separation for the controlled case . . . 103
7.19 Contours of time-averaged streamfunction Ψ . . . 103
7.20 Instantaneous contours of pressure coefficient C_P for the baseline and controlled flows . . . 104

8.1 Characteristics of computational cells forming the grid and skin friction and wall pressure distributions . . . 108
8.2 Flow characteristics downstream of separation . . . 109
8.3 Pressure spectra in the recirculation bubble . . . 110
8.4 Contours of autocorrelation function $R_{pp}(\mathbf{x}, \Delta t)$ downstream of separation. (a) x=0, (b) x=2, (c) x=4 and (d) x=6. . . . 112
8.5 Instantaneous isosurfaces of pressure coefficient C_P for the baseline flow . . . 114
8.6 Description of pseudo-periodic bursting event . . . 115
8.7 Effect of open-loop harmonic forcing on reattachment length and base pressure 116
8.8 Bode plots of frequency responses $G(i\omega)$ . . . 117
8.9 Frequency-domain characteristics of the closed loop system . . . 118
8.10 Input and output control signals . . . 119
8.11 Autocorrelation function $R_{pp}(\mathbf{x}, \Delta t)$ of pressure signals downstream of separation for the controlled flow. (a) x=0, (b) x=2, (c) x=4 and (d) x=6. . . . 120
8.12 Instantaneous isocontours of Q=5 for (a) the baseline and (b) controlled flows, obtained with grid *Fine_z*. . . . 121

9.1 Two-dimensional slice of the nominal grid . . . 125
9.2 Characteristics of computational cells forming the grid . . . 127
9.3 Instantaneous isosurfaces of (a) vorticity magnitude and (b) pressure coefficient 128
9.4 Characteristics of the dominant unsteady modes . . . 128
9.5 Instantaneous vorticity contours and corresponding base pressure distributions 130
9.6 Bode plots of frequency responses . . . 131
9.7 Frequency-domain characteristics of the closed-loop system . . . 132
9.8 Line contours of streamfunction for the baseline and controlled flows . . . 133

List of Tables

4.1 Dominant instabilities in reattaching shear flows 52
4.2 Most effective forcing frequency for reattaching shear layers. 55

7.1 Effects of domain size and grid resolution 82

8.1 Effects of domain size and grid resolution 107
8.2 Comparison of open-loop and closed-loop control results 122

9.1 Effects of domain size and grid resolution 126

Chapter 1

Introduction

1.1 Motivation

The majority of modern transportation systems rely on fossil fuels as their primary source of energy, thus generating polluting gases and perpetuating our dependence upon finite resources. According to a communication by the European Commission in 2007 [111], road transportation alone represents about a fifth of the European Union's (EU) CO_2 emissions—with passenger cars responsible for about 12%. While the EU-25 generated 5% less greenhouse gases in 2004 than in 1990, CO_2 emissions from road transport rose by 26% during that period. Under the Kyoto protocol, the EU committed to achieving at least a 20% reduction of greenhouse gases emissions by 2020, as compared to the levels of 1990. Consequently, there is an obvious need to explore new strategies to reduce the carbon emissions generated by road vehicles.

The energy consumed by road vehicles is lost in several ways, including engine inefficiencies, kinetic energy lost to braking, transmission losses, rolling friction and aerodynamic drag. At motorway speeds, the aerodynamic drag is generally dominant. In fact, for heavy trucks travelling on a highway, two-thirds of the fuel consumption result from the aerodynamic drag [123], while the rolling friction and transmission losses represent about 20-25% and 10-15% respectively [99].

The traditional aerodynamic design of ground transport systems has reached a mature state and remains subject to stringent compromise with other requirements such as safety, aesthetics, usability and cost. The more recent field of active flow control, in particular closed-loop (or feedback) flow control, offers a promising alternative. Feedback flow control draws on techniques developed by the control systems community and applies them to shape the

behaviour of the flow. It consists of introducing local perturbations into the flow via small actuators that can be added to an existing design without substantial changes in the geometry. These perturbations respond to sensor measurements and generally target resonance with particular features of the dynamics. Therefore, this approach potentially allows for a strong response from the flow and high efficiency, as well as adaptability to changing conditions.

Wind-tunnel experiments or numerical simulations of flows past complex road vehicle shapes at high Reynolds numbers remain prohibitively expensive or time-consuming; in particular where detailed aerodynamic investigations are to be carried out. Therefore, generic shapes that can reproduce the features of interest are often preferred for such studies [81]. Blunt-based bluff bodies, in particular, are well adapted for studying some aspects of the relevant fundamental dynamics. This class of bodies exhibits at least two essential features of road vehicles, namely a fixed separation point and a highly unsteady recirculation region forming at the trailing edge and leading to a large form-drag.

The objective of this thesis is to investigate numerically the use of linear feedback control to achieve a sensible form-drag reduction on a blunt-based bluff body. The work is based on detailed numerical computations which grant access to information and techniques that are out of reach in an experimental setting. However, a strong emphasis has been placed on developing a strategy that can be reproduced experimentally. For example, methods requiring adjoint computations or real-time information from the flow away from the body are not relied upon for the control action. The control is effected via synthetic jets because these are convenient and efficient from an experimental point of view.

1.2 Overview

The present computational study considers flow control on two distinct bluff bodies. The major part of the thesis is concerned with a wall-mounted body with a blunt trailing edge that reduces to a backward-facing step, after which a D-shaped body is investigated. The effect of parameters such as the actuator location and the Reynolds number are explored.

According to Ahmed [2], the typical Reynolds numbers encountered by full-scale automotive vehicles exceed $Re_h = U_0 h/\nu = 10^6$, where U_0 is the freestream velocity, h is a characteristic length scale of the vehicle and ν is the kinematic viscosity of the stream. Such high Reynolds numbers are currently out of reach for time-resolved numerical simulations, even with the most

advanced computer facilities. Consequently, lower Reynolds numbers were selected in this work. For the turbulent backward-facing step flow, two Reynolds numbers are considered: $Re_h = 2 \cdot 10^4$ and $Re_h = 4 \cdot 10^4$, where h is the step height. The Reynolds number can also be scaled with the boundary layer developing upstream of separation. Based on the momentum thickness of the boundary layer θ at separation, the Reynolds examined are $Re_\theta = U_0\theta/\nu = 1500$ and $Re_\theta = 3000$. These Reynolds numbers are chosen to ensure that the upstream boundary layer is close to being fully turbulent. This is important because the dynamics of bluff body wakes are sensitive to the state of the boundary layer at separation. Also, statistical features of the boundary layer become less dependent on the Reynolds number when it is fully turbulent. According to Schlichting & Gersten [121], flat-plate boundary layers can be considered as fully turbulent for $Re_\theta > 2000$. Note that the Reynolds numbers considered remain a challenge for well-resolved simulations and call for computations on massively parallel supercomputers.

The main contributions of this thesis are as follows:

- Large-eddy simulations of the incompressible flow past a backward-facing step at two Reynolds numbers $Re_h = 2 \cdot 10^4$ and $4 \cdot 10^4$.
- Investigations into the effects of unsteady open-loop actuation on reattaching shear layers and recirculation bubbles.
- Development of a feedback control strategy to reduce form-drag on bluff bodies based on a hypothesis about the link between base pressure force fluctuations and mean.
- Application of linear system identification and classical feedback control tools to three distinct flow cases, including turbulent wakes.

Chapters 2 to 4 introduce important concepts that will be used in later chapters and each provide a discussion on one of the three key elements of this work: (i) low-order modelling and flow control, (ii) numerical simulations and (iii) bluff body flow dynamics.

In chapter 2, we give an overview of control strategies applied in fluid dynamics, with a focus on the studies applied for drag reduction on bluff bodies.

Chapter 3 provides an introduction to the main concepts relating to the numerical simulations carried out during this work. The technique of large-eddy simulation (LES) is explained and the flow solver StreamLES is described.

Some aspects of bluff body flows are discussed in chapter 4, with an emphasis on reattaching shear layers (pertinent in the case of wall-mounted bodies). The main features of backward-facing step flows are scrutinized, including flow instabilities and previous control attempts.

Chapter 5 acts as a bridge between introductory chapters and the main results. It provides an overview of the problem setup, including a description of the three flow cases considered and an outline of the system identification and control strategies used in this work.

Chapter 6 considers a two-dimensional (2D) laminar backward-facing step flow at $Re_h = 2000$. This simple configuration is considered first in order to validate the numerical simulations and the control strategy. Open-loop characterization and feedback control are performed, and lead to a 70% increase in time-averaged base pressure.

In chapter 7, we turn our attention to a three-dimensional (3D) turbulent backward-facing step flow, at a Reynolds number $Re_h = 2{\cdot}10^4$. We examine the uncontrolled flow and the effects of open-loop harmonic forcing. System identification and feedback control are carried out. Further insight into the fluid mechanisms and the impact of the Reynolds number, including system identification and feedback control performed at $Re_h = 4 \cdot 10^4$, are studied in chapter 8. We extend our control strategy to reduce form-drag on the D-shaped bluff body in chapter 9.

Finally, concluding remarks and suggestions for future work are given in chapter 10.

Chapter 2

Relevant flow control issues

2.1 Background

The goal of this chapter is to provide a brief but general review on the marriage of control theory with fluid dynamics. The discussion is divided into two parts. The first part attempts to provide a flavour of the work that has been done on using flow control to reduce form-drag on bluff bodies. This section is on purpose kept concise; the interested reader is referred to Gad-el-Hak et al. [47] and Gad-el-Hak [46] for general surveys on flow control. A slightly more recent discussion on active flow control is provided by Collis et al. [25]. Since the main contribution of the present study is concerned with closed-loop control, the second part describes general strategies for closed-loop control applied to fluid flows. Some relevant concepts from control theory and model reduction are discussed, with a focus on the control approach that is used in the present work.

2.2 Flow control for bluff body drag reduction

One may distinguish three types of control actions: passive, active open-loop and active closed-loop (feedback) control. Passive control, sometimes referred to as flow management [47], uses actuation without power input. Passive control for reducing the form-drag of bluff bodies has been extensively studied. For example, it is well known that addition of a splitter plate along the wake centerline is an efficient means to delay vortex shedding and increase the base pressure [115]. Strategies based on disrupting the spanwise coherence of rollers in the wake can achieve important drag reductions. For instance, Tanner [132] investigated the flow behind a wing



Figure 2.1: Boat tail device developed at Technische Universiteit Delft and commercialized by Ephicas; from Van Raemdonck [140].

with a blunt trailing edge. He introduced a broken separation line using a segmented trailing edge and measured drag reductions of up to 64%. More recently, Park et al. [107] found that adding small tabs to the upper and lower trailing edges of a blunt body yields significant drag reductions. Unfortunately, these techniques are essentially limited to 2D bodies. A few passive devices have been tested on full-scale road vehicles. For instance, Modi et al. [99] installed trip fences on the front face of a truck trailer and hence obtained drag reductions of up to 16%. Figure 2.1, from Van Raemdonck [140], illustrates a large passive boat tail device that can be added to an existing truck. Fuel savings of up to 7.5% have been recorded during on-road tests [140].

However, passive devices require complex geometry changes and may have adverse effects away from their design point. Open-loop control (corresponding to powered actuation without sensing) can reproduce the beneficial effects of passive devices and widen the operating range. Wood [146] notably showed that base bleed displaces the vortex formation region further downstream from the trailing edge of a two-dimensional bluff body, resulting in base pressure increase. Extensive wind-tunnel testing on truck models by Seifert et al. [123] has shown open-loop control to be capable of net fuel reductions exceeding 10%. Englar [39] also achieved significant drag reductions on model trucks and streamlined vehicles using circulation control.

Closed-loop control is achieved via powered actuators responding to sensors in the flowfield. By contrast to open-loop actuation, feedback control can modify the dynamics of a system, for instance stabilizing flows with unstable modes such as cavity resonances [17] or thermoacoustic instabilities [33]. In addition, closed-loop control offers further degrees of freedom to deal with uncertainty and increase efficiency. Feedback control strategies for bluff body drag reduction

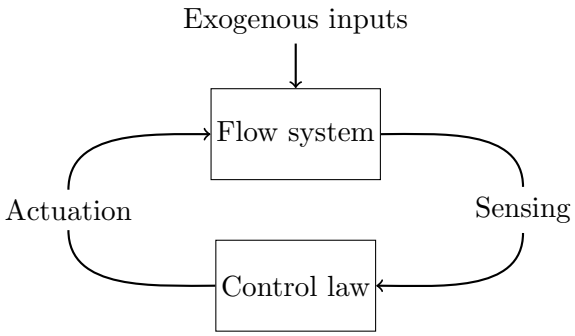


Figure 2.2: Diagram of closed-loop flow control system.

are usually categorized into separation control or direct wake control. The former apply only to bodies with moveable separation points such as the circular cylinder [124] or a step with a rounded edge [74]. Significantly less work has been carried out on using direct wake control to reduce form-drag on bluff bodies with a blunt trailing edge, although a few examples do exist. For instance, Henning & King [56] used quantitative feedback theory to increase the base pressure of a D-shaped wind-tunnel model. Pastoor et al. [108] also examined feedback strategies for drag reduction on the same bluff body and achieved a 15% drag reduction. Stalnov et al. [130] performed an experimental investigation aimed at stabilizing the wake of a D-shaped bluff body with a proportional-integral control law. They showed their controller to lead to a concomitant drag reduction associated with a delayed roll-up of the separating shear layers, hence a reduction in the streamwise momentum transferred to the recirculation region.

2.3 Strategies for linear closed-loop flow control

2.3.1 Essential ingredients

Feedback flow control involves a closed-loop relation between the actuation, the sensing and the flow system to be controlled (called the plant in control theory). The actuation produces changes in the flow which are measured by the sensor, and this information is in turn used to adjust the actuation. This leads to the closed-loop dynamical system sketched in figure 2.2.

The loop is built by connecting two dynamical sub-systems: the flow and the control law. The ultimate design of any attempt at closed-loop flow control is to synthesize a control law that will perturb the flow system towards a desired behaviour or state. The requirements for a successful controller depend on the properties of the flow system, the control objective and

exogenous influences. Exogenous influences include all perturbations affecting the flow system other than the predictable control inputs. Some examples are actuator or sensor noise and eddies naturally present in the flow considered. In practice, some level of uncertainty about the boundary conditions always exists and the properties of the flow system can not be known exactly. This is also an important factor to be taken into account for successful control. In fact, uncertainty and exogenous influences form the justification for resorting to closed-loop control instead of pre-determined actuation.

There are essentially two distinct frameworks to construct a control system. The first approach is called model-based control. It requires a mathematical model approximating the behaviour of the plant, before a controller can be designed and implemented. The second approach, model-free control, treats the flow response as an unknown and uses a controller that adapts to a real-time observation of the behaviour of the plant. There are some successful examples of this second method. For instance, Henning & King [56] used extremum-seeking feedback to reduce form-drag on a bluff body. More general details on this approach can be found in King [76].

The present work only considers model-based control. The design of a control system can thus be divided into two areas of focus: the plant and the controller. The treatment of uncertainty and noise is also a key element, but it can be dealt with during the controller synthesis. We first review techniques to construct a flow model and then discuss control design.

2.3.2 Reduced-order modelling

In fluid dynamics, the equations governing the flow are generally known, albeit as a system of non-linear partial differential equations with no known closed-form solution for complex flows. Discrete numerical solutions or time-resolved experimental datasets can be obtained, but their high-dimensionality precludes direct use for control, at least in the case of turbulent flows. It is thus necessary to obtain a low-order model of the flow dynamics.

Projection-based methods work by projecting the dynamics that evolve on a high-dimensional space onto a low-dimensional subspace formed by a set of modes. Common examples include proper orthogonal decomposition (POD) [60], balanced truncation [100] and balanced POD [118]. POD can be applied to non-linear systems, and balancing of non-linear systems can be achieved with the method of empirical gramians (see Lall et al. [84]). However, projection methods generally rely on information about a large portion of the flow which is often not

available in real-life applications.

Even though the dynamics of fluid flows are non-linear, there have been some attempts to represent certain key processes by dynamic linear models (Farrel & Ioannou [40], Kwong & Dowling [83]). A strong incentive behind a linear approach is that linear control provides a wide range of tools which are not available for non-linear systems. Furthermore, as highlighted by Kim & Bewley [72], modelling for control is different than modelling for simulation, in that the model need not necessarily describe all the dynamics accurately for the control to work. This is the perspective that is followed in this thesis. We aim to investigate whether linear control can be applied to reduce form-drag in turbulent flows.

There are three main routes to building linear reduced-order flow models. The first approach is to linearize the Navier-Stokes equations about a base flow, and numerically study small perturbations in its neighbourhood. Cortelezzi & Speyer [26] presented a model reduction method based on linearization of the 2D Poiseuille flow. Using linear quadratic gaussian (LQG) control, they managed to reduce skin friction drag in the laminar channel flow. This framework was extended to a 3D turbulent channel flow by Lee et al. [88]. More recently, Jones et al. [70] developed a method to derive a linear low-order state-space model of transient growth in a 3D unsteady boundary layer flow. Using a Kalman filter, they were able to reconstruct the velocity field in the boundary layer based on wall sensor information.

The second method consists of constructing models based on physical insight into large-scale processes that contribute to the dynamics. For example, Pastoor et al. [109] and Henning et al. [57] developed vortex models to control a transitional backward-facing step and a bluff body wake, respectively.

The last approach is system identification, where so-called black-box models are built using input-output data from the flow system. One of the earliest attempts to derive a linear flow model using system identification was by Kwong & Dowling [83]. They considered the unsteady flow in a diffuser and used harmonic forcing to evaluate the transfer function between a wall jet actuator and a pressure measurement. They were able to use the resulting linear model to design a controller, via loop-shaping, for reducing unsteadiness in the flow. A good agreement between the control results and the predictions of linear control theory were observed, despite the non-linear effects existing in the flow. Their approach forms part of the motivation for the present work, in which we use system identification to identify the response of the flow to actuation.

Other examples of system identification being used to develop flow models for control include Huang & Kim [62], who modelled the 2D (laminar) separated flow over a flat plate. They started by assuming a model structure and then used input-output data sequences to calibrate the parameters of this model. Finally, an LQG controller was designed to reduce the extent of the separated region. In a recent study on a 2D (laminar) backward-facing step flow at a Reynolds of 500, Hervé et al. [58] used linear system identification to estimate the coefficients of an auto-regressive moving-average exogenous model (ARMAX). The model approximates the response of a skin friction sensor to an actuator located near separation. The observable influence of a noise source is taken into account thanks to an upstream *observer* sensor and a feedforward strategy is then used. Illingworth et al. [67] used the Eigensystem Realization Algorithm (ERA) as a system identification and model reduction technique to control flow resonances. Balanced models of very low-order were obtained, leading to efficient control within a wide range of operating conditions.

System identification based on input-output data has been used more widely for modelling rather than control purposes. It has been applied to diverse flow problems, ranging from combustion oscillations (Zhu et al. [149]) to helicopter rotor noise (Morgans & Dowling [101]). System identification has the advantage of providing a level of accuracy that is often not available via first-principles modelling when complex phenomena, such as turbulence, are involved.

2.3.3 Controller design

For all control systems, a mathematical relation governing the response of the actuators to the sensors needs to be defined, with a view to perturbing the flow system towards a desired state. Control theory offers a vast panel of simple control laws (such as proportional or integral control), as well as tools to construct sophisticated controllers based on specified objectives, including stability, robustness and optimality constraints.

Historically, two theoretical frameworks have developed separately: classical and modern control. Before the advent of modern control, classical theory only dealt with single-input single-output (SISO) systems, using differential equations in the time-domain or Laplace transforms in the frequency domain. The development of modern control in the 1960's helped to overcome some of the limitations of classical theory by expressing a system as a set of first-order differential equations with state variables. Since then, a revival of classical control has

been observed, thanks in part to the evolution of robust control theory, which blends concepts from both approaches.

The fact that many control tools are based on the theory of linear dynamical systems has so far limited their use in fluid dynamics [118]. But successful attempts, some of which have been cited above, are burgeoning in different directions. Excellent reviews and discussions on linear closed-loop control for fluid dynamics are given in Bewley [8] and Kim & Bewley [72]. For a general introduction to control theory, the reader is referred to Jacobs [68] and robust and optimal control are discussed in Zhou et al. [148].

Chapter 3

Numerical simulations

3.1 Background

In this chapter, we first introduce the computational approach used in the present work: large-eddy simulation. We expand over its main features, including the issue of subgrid-scale modelling, and review its applications for bluff body flows. Then, we go on to describe the numerical solver.

The importance of numerical methods in fluid dynamics has greatly increased over the last few decades thanks to the fast development of computing speeds and storage capacity. Computational Fluid Dynamics (CFD) has become an invaluable component of industrial design and an indispensable tool to complement theoretical and experimental research. Nevertheless, the capabilities of CFD for modelling turbulent flows are still challenged by the dominance of non-linear effects and the wide spectrum of observed scales.

The most accurate numerical representation of turbulence is Direct Numerical Simulation (DNS). It consists of solving the Navier-Stokes equations without approximations other than numerical discretizations whose errors can be controlled. In such simulations, all scales of motion are resolved numerically which constrains the domain to be sufficiently large and the grid sufficiently fine. The computational requirements of DNS at high Reynolds numbers remain far out of the reach of current computer resources, both in terms of processing speed and storage. To illustrate the obstacles involved in performing DNS at large Reynolds numbers, consider the simple case of a statistically homogeneous and isotropic turbulent flow. The ratio

between the largest scales L and the smallest scales η co-existing in such a flow is given by

$$\frac{L}{\eta} = O(Re^{3/4})$$

in which Re is the Reynolds number. In three-dimensional space, we therefore require at least $O(Re^{9/4})$ degrees of freedom to represent all the scales. In addition, the use of explicit time-integration methods imposes a linear condition between the time-step and the mesh size. This may lead to very long integration times in order to capture the full characteristic periods of the largest scales.

At the other side of the range, statistical modelling techniques provide the least detail. This approach is based on a decomposition of the flow variables into a steady and a fluctuating part, where the steady part corresponds to an ensemble averaging (Reynolds-averaging). Applying the Reynolds-averaging operator to the Navier-Stokes equations results in a new set of equations, the Reynolds-Averaged Navier-Stokes (RANS) equations, describing the spatial evolution of the mean velocity and pressure fields. The majority of numerical turbulent flow problems solved in industry rely on RANS methods.

An intermediate approach between DNS and RANS is large-eddy simulation (LES). In LES, only the large, most energetic scales are directly computed while the interaction with the small, more universal scales is modelled. In contrast with RANS methods, only the small scales are modelled which may lead to simpler closure models since those scales are expected to be more homogeneous. The distinction between resolved and unresolved scales is obtained through the application of a spatial filter.

3.2 Governing equations for LES

3.2.1 Navier-Stokes equations

The dynamics of an incompressible flow for a non-reacting Newtonian fluid are described by the conservation laws for mass and momentum, known as the Navier-Stokes equations:

$$\frac{\partial u_i^*}{\partial x_i^*} = 0 \tag{3.1a}$$

$$\frac{\partial u_i^*}{\partial t^*} + \frac{\partial u_i^* u_j^*}{\partial x_j^*} = -\frac{1}{\rho^*}\frac{\partial p^*}{\partial x_i^*} + \nu^* \frac{\partial^2 u_i^*}{\partial x_j^{*2}} \tag{3.1b}$$

where ρ^* is the constant fluid density, p^* is the static pressure, ν^* is the laminar kinematic viscosity, u_i^* is the component of the velocity in the i^{th} spatial direction, x_i^* is the Cartesian

coordinate in the i^{th} spatial direction and t^* is time. In LES and turbulence modelling in general, it has become standard practice to work with non-dimensional parameters and equations. Thus, the flow variables are expressed in terms of a characteristic velocity U_0 and length scale of the flow L_0:

$$t = \frac{t^* U_0}{L_0} \ , \ x = \frac{x^*}{L_0} \ , \ u_i = \frac{u_i^*}{U_0} \ , \ p = \frac{p^*}{\rho^* U_0^2} \ , \ Re = \frac{U_0 L_0}{\nu^*},$$

where Re is the Reynolds number. This leads to the non-dimensional incompressible Navier-Stokes equations:

$$\frac{\partial u_i}{\partial x_i} = 0 \tag{3.2a}$$

$$\frac{\partial u_i}{\partial t} + \frac{\partial u_i u_j}{\partial x_j} = -\frac{\partial p}{\partial x_i} + \frac{1}{Re}\frac{\partial^2 u_i}{\partial x_j^2} \tag{3.2b}$$

Note that from now on and for the remainder of this thesis, all variables considered are non-dimensionalized with the characteristic scales given above, unless otherwise stated. The velocity scale U_0 is the freestream velocity and L_0 will be taken as the step height h in the case of the backward-facing step and the body height (also called h) for the D-shaped body.

3.2.2 Scale separation

The governing equations for LES are obtained by applying a scale high-pass filter, i.e. low-pass in wavenumber, to (3.2) so as to decompose the flow variables into two terms representing the resolved and unresolved scales. The filter is applied via a convolution integral over the flow domain Ω:

$$\overline{f(\mathbf{x}, t)} = \int_\Omega \overline{G}(\mathbf{x,x'}) f(\mathbf{x'}, t) \mathbf{dx}' \tag{3.3}$$

where $f(\mathbf{x'}, t)$ is the function to be filtered and $\overline{G}$ is a rapidly decaying filtering function with $\int_\Omega \overline{G}(\mathbf{x})\mathbf{dx} = 1$ and filter width $\overline{\Delta}$. The filtering operation must be constant-preserving, linear and must commute with differentiation. Provided the filter width is constant, the last property is satisfied. For inhomogeneous flows the filter width should be a function of space to account for the varying average size of turbulent eddies in different regions of the flow, generally leading to a commutation error. Ghosal and Moin [51] have shown that this error is typically second-order in the filter width, so that it can usually be neglected for first and second-order discretization schemes.

Figure 3.1a illustrates the three most common filters in physical space: the top-hat or box filter, the Gaussian filter and the sharp cut-off filter. In Fourier space the convolution with a

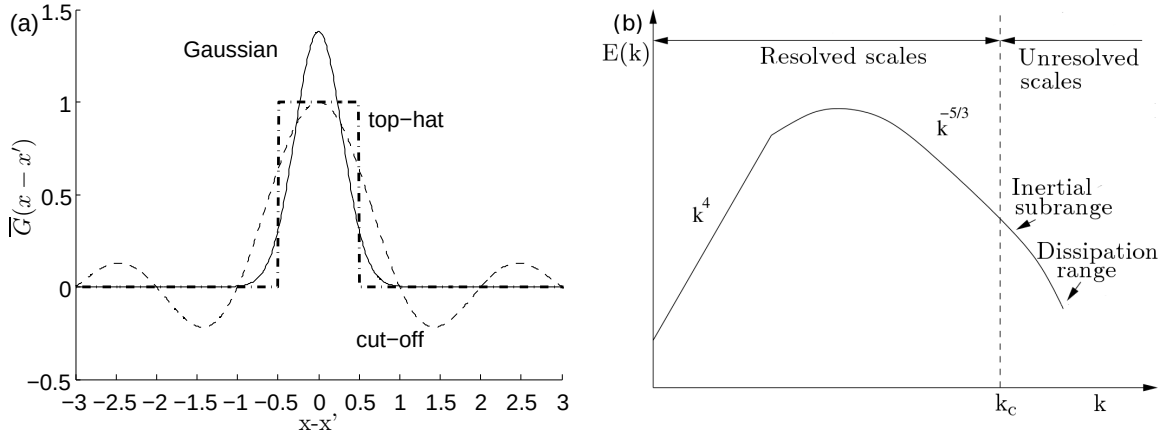


Figure 3.1: (a) Common filters for LES and (b) principle of the cut-off in the 1D energy spectrum from Temmerman [133].

homogeneous (constant width) filter becomes a product:

$$\widehat{\overline{f}}(k) = \widehat{\overline{G}}(k)\widehat{f}(k) \tag{3.4}$$

where the notation $\widehat{(\cdot)}$ denotes the Fourier transform of the quantity $(\cdot)$. This allows for a more intuitive view of the filtering effect. Consider, for example, the sharp cut-off filter defined as $\widehat{\overline{G}}(k) = 1$ if $k \leq \pi/\overline{\Delta}$ and zero elsewhere. The resulting $\widehat{\overline{f}}(k)$ only contains information for wavenumbers below the cut-off. Figure 3.1b from Temmerman [133] shows the effect of the cut-off filter on the energy spectrum. The scales corresponding to wavenumbers higher than k_c are truncated.

The decomposition operated by the filter is described by (3.5).

$$f(\mathbf{x},t) = \underbrace{\overline{f(\mathbf{x},t)}}_{resolved\ scales} + \underbrace{f'(\mathbf{x},t)}_{unresolved\ scales} \tag{3.5}$$

Note that despite the apparent similarity with Reynolds averaging, filtering in LES is an operation in space. In addition, with a general filtering operation $\overline{\overline{u}} \neq \overline{u}$ and $\overline{u\overline{v}} \neq \overline{u}\,\overline{v}$, which distinguishes LES filtering from Reynolds averaging. The application of a homogeneous filter verifying the conditions listed above to the Navier-Stokes equations (3.2) results in the following:

$$\frac{\partial \overline{u_i}}{\partial x_i} = 0 \tag{3.6a}$$

$$\frac{\partial \overline{u_i}}{\partial t} + \frac{\partial \overline{u_i u_j}}{\partial x_j} = -\frac{\partial \overline{p}}{\partial x_i} + \frac{2}{Re}\frac{\partial \overline{S_{ij}}}{\partial x_j} \tag{3.6b}$$

where $S_{ij} = 0.5(\frac{\partial u_i}{\partial x_j} + \frac{\partial u_j}{\partial x_i})$ is the strain rate. These equations dictate the dynamics of the large scales of motion and the effect of the small scales on the resolved ones is included in the nonlinear convection term $\overline{u_i u_j}$. This term can not be computed and has to be expressed in terms of $\overline{u}$ and u'.

3.2.3 Leonard's decomposition

Decomposing the velocity into its resolved and unresolved parts, $u_i = \overline{u_i} + u_i'$, leads to the following expression:

$$\overline{u_i u_j} = \overline{\overline{u_i}\,\overline{u_j}} + \overline{\overline{u_i} u_j'} + \overline{u_i' \overline{u_j}} + \overline{u_i' u_j'} \tag{3.7}$$

The terms that are not exclusively dependent on the large scales are grouped into the subgrid-scale tensor τ_{ij}. Leonard [89] proposed a decomposition of τ_{ij} into three terms as follows:

$$\tau_{ij} = \overline{u_i u_j} - \overline{u_i}\,\overline{u_j} = \underbrace{\overline{\overline{u_i}\,\overline{u_j}} - \overline{u_i}\,\overline{u_j}}_{L_{ij}} + \underbrace{\overline{\overline{u_i} u_j'} + \overline{u_i' \overline{u_j}}}_{C_{ij}} + \underbrace{\overline{u_i' u_j'}}_{R_{ij}} \tag{3.8}$$

The Leonard stresses L_{ij} represent interactions between the large scales that result in small-scale contributions, the cross-terms C_{ij} represent interactions between large and small scales and the subgrid-scale Reynolds stresses R_{ij} account for interactions between the small scales. Difficulties arise with subgrid-scale models that represent each of these terms separately due to the fact that L_{ij} and C_{ij} are not Galilean invariant [133]. As a result, Leonard's decomposition is not often used in practice but rather serves as a conceptual tool to examine the influence of each term separately.

Introducing τ_{ij} into (3.6) leads to the governing equations for LES as they are solved today:

$$\frac{\partial \overline{u_i}}{\partial x_i} = 0 \tag{3.9a}$$

$$\frac{\partial \overline{u_i}}{\partial t} + \frac{\partial \overline{u_i}\,\overline{u_j}}{\partial x_j} = -\frac{\partial \overline{p}}{\partial x_i} + \frac{2}{Re}\frac{\partial \overline{S_{ij}}}{\partial x_j} - \frac{\partial \tau_{ij}}{\partial x_j} \tag{3.9b}$$

The LES equations are not closed because of the presence of the subgrid-scale tensor τ_{ij}. Thus a so-called subgrid-scale model is required to account for the effects of the unresolved scales. Note that in the limit as the filter width tends to zero, the contribution of the subgrid-scale stresses τ_{ij} vanishes and the LES equations tend to the original Navier-Stokes equations.

3.2.4 Schumann's approach

Besides the convolution operation described above, the discretization of the equations also acts as a filter segregating scales larger and smaller than the grid size. The 'volume balance procedure' detailed by Schumann [122] shows that the modified discrete equations obtained by averaging the equations over fixed finite volume cells (and applying the divergence theorem to the volume integrals) contain an additional term that represents the effect of the scales smaller than the grid cells. In practice, the filtering convolution is often left out and the grid is used instead to control the scale separation. This justifies the prevalence of the terminology *subgrid-scales* rather than *subfilter-scales*. This implicit filtering approach represents a benefit in terms of the complexity of the code implementation and computational cost. On the other hand, explicit filters allow a better control of the numerical error.

3.3 Subgrid-scale modelling

3.3.1 Background

Subgrid-scale modelling is a distinctive feature of LES. Its primary role is to dissipate the energy cascading from the large to the small scales, effectively reproducing the role of the kinetic energy drain occurring at the high end of the wave number band. But the cascading is an average process: locally and instantaneously the transfer of energy can be larger or smaller than the average and can also occur in the opposite direction (backscatter). Hence, ideally, the model should also be able to represent this local behaviour.

The importance of the subgrid-scale model in yielding an accurate behaviour for the unresolved scales depends on the grid size (or filter width). If the grid is very fine, even a crude model could suffice. On the contrary, a coarse grid should be made up for by using a higher quality model. This is mainly a consequence of the more homogeneous and isotropic character of the finer scales which respond better to modelling. Thus a compromise arises between the grid size and the sophistication of the model to obtain the desired level of accuracy at an acceptable computational cost.

A plethora of different formulations for the subgrid-scale stresses have been developed in the last few decades, ranging from relatively simple algebraic expressions to models involving the resolution of one or several transport equations. As is the case in the RANS community, only a few of these models are used in practice [137]. Models based on the eddy-viscosity

concept, also called the Boussinesq hypothesis, are very popular among LES practitioners owing to their conceptual simplicity, ease of implementation and dissipative properties. This formulation translates the role of the subgrid-scale stresses as an agent increasing transport and dissipation, by relating the traceless part of τ_{ij} to the strain rate via a proportionality coefficient ν_t, known as the turbulent or eddy viscosity:

$$\tau_{ij} - \frac{\delta_{ij}}{3}\tau_{kk} = -2\nu_t\overline{S_{ij}}. \tag{3.10}$$

Two eddy-viscosity models that were considered in this work are presented below: the Smagorinsky and the wall-adapted local eddy-viscosity models. Both are in common use in LES today. In addition, the dynamic procedure of Germano et al. [49], designed to enhance models with constant calibration coefficients, is discussed. The Implicit LES (ILES) approach is also mentioned in passing as it is gaining growing support in the LES community. For a detailed account of subgrid-scale modelling and a rich list of models, the reader is referred to Sagaut [120].

3.3.2 Smagorinsky model

The earliest and most widely used model was introduced by Smagorinsky [127]. Dimensional analysis arguments yield that the eddy viscosity ν_t is proportional to the product of the length and velocity scales of the unresolved motion, l_s and q_s. The characteristic length scale $l_s = C_s\overline{\Delta}$ is proportional to the filter width via the Smagorinsky constant C_s, which requires calibration. The velocity scale is constructed from the gradients of the resolved velocity field, $q_s = l_s(2\overline{S_{ij}}\,\overline{S_{ij}})^{1/2} = l_s|\overline{S}|$. These assumptions result in the following equation for the eddy viscosity:

$$\nu_t = l_s q_s = (C_s\overline{\Delta})^2|\overline{S}| \tag{3.11}$$

The local filter width $\overline{\Delta} = (\Delta x\Delta y\Delta z)^{1/3}$ is based on the dimensions of the computational cell. A notable advantage of the Smagorinsky model is its ease of implementation into an existing Navier-Stokes solver.

Unfortunately, this model suffers from a few significant deficiencies. Firstly, it is limited by the assumption of a constant value for C_s (generally $C_s = 0.1$). Secondly, ν_t is allowed to be non-zero at the wall, although the no-slip condition requires τ_{ij} to vanish at solid boundaries. An exponential damping function can be used to counteract this near-wall behaviour. Thirdly, the model generates non-zero eddy viscosity in a laminar flow with pure shear which

causes problems for simulating transition. Finally, the spatial operator $|\overline{S}|$ identifies regions of high dissipation associated with irrotational strain but neglects the contribution of vorticity-dominated zones [105].

3.3.3 WALE model

The wall-adapted local eddy-viscosity (WALE) model, proposed by Nicoud and Ducros [105], attempts to address some of the limitations of Smagorinsky's formulation. It is constructed with an operator based upon the square of the velocity gradient tensor $\overline{g}_{ij} = \frac{\partial \overline{u_i}}{\partial x_j}$:

$$S_{ij}^d = \frac{1}{2}(\overline{g}_{ij}^2 + \overline{g}_{ji}^2) - \frac{1}{3}\delta_{ij}\overline{g}_{kk}^2 \tag{3.12}$$

where $\overline{g}_{ij}^2 = \overline{g}_{ik}\overline{g}_{kj}$. In contrast to $\overline{S_{ij}}$, Nicoud and Ducros [105] show that operators built upon S_{ij}^d:

- take into account the effects of the small-scale strain rates as well as rotation rates;
- produce vanishing ν_t at the wall.

Scaling considerations to reproduce the cubic wall-asymptotic behaviour of the eddy viscosity lead to the following model:

$$\nu_t = (C_w\Delta)^2 \frac{(S_{ij}^d S_{ij}^d)^{3/2}}{(\overline{S_{ij}}\,\overline{S_{ij}})^{5/2} + (S_{ij}^d S_{ij}^d)^{5/4}} \tag{3.13}$$

The constant C_w is determined in reference with the Smagorinsky constant and is usually set to $C_w^2 = 0.1$. The authors show that the model is successful at handling transition. Temmerman [133] reports good results for fully developed channel flow simulations with the WALE model compared with a range of other models. In addition, he showed that the WALE model returns lower values of the eddy viscosity than the Smagorinsky model.

3.3.4 Dynamic procedure

The dynamic procedure of Germano et al. [49] allows the calibration constant of a functional model to vary in space and time. This method is based upon the interaction between two filters: the grid filter $\overline{G}$ introduced in §3.2.2, with filter width equal to the grid size, and the test filter $\widetilde{G}$ with a larger width (typically $\widetilde{\Delta} = 2\overline{\Delta}$). The application of the grid filter to the

Navier-Stokes equations leads, as noted earlier, to the LES equations (3.9). Applying the test filter to (3.9b) results in a similar set of equations:

$$\frac{\partial \widetilde{\overline{u_i}}}{\partial t} + \frac{\partial \widetilde{\overline{u_i}}\,\widetilde{\overline{u_j}}}{\partial x_j} = -\frac{\partial \widetilde{\overline{p}}}{\partial x_i} + \frac{2}{Re}\frac{\partial \widetilde{\overline{S_{ij}}}}{\partial x_j} - \frac{\partial T_{ij}}{\partial x_j}$$

where the subgrid-scale stress is now $T_{ij} = \widetilde{\overline{u_i u_j}} - \widetilde{\overline{u_i}}\,\widetilde{\overline{u_j}}$. The effects of the scales that lie in between the two filter widths are characterized by the resolved turbulent stresses

$$\mathcal{L}_{ij} = T_{ij} - \widetilde{\tau_{ij}} = \widetilde{\overline{u_i}\,\overline{u_j}} - \widetilde{\overline{u_i}}\,\widetilde{\overline{u_j}} \tag{3.14}$$

which can be computed explicitly. If one assumes that the two unknown stress tensors τ_{ij} and T_{ij} can be modelled with the same functional form (e.g. the Smagorinsky model), then the coefficient appearing in this model can be computed from equation (3.14), known as the Germano identity. Consequently, this approach relieves the LES user from the need to set a constant calibration coefficient. Instead, the latter is computed dynamically based on local information about the smallest resolved scales.

The dynamic procedure coupled with the Smagorinsky model is an important improvement over the original Smagorinsky formulation. The subgrid-scale stresses vanish at walls and in laminar flow, and the cubic wall-asymptotic behaviour of ν_t is reproduced. In addition, the coefficient can become negative locally, so that backscatter can be represented. The main disadvantage, however, is the extra cost associated with the second filtering operation.

3.3.5 Implicit LES

The traditional view treats the subgrid-scale model and discretization as two separate issues, although the two are inevitably coupled in practice. This implies the assumption that the numerical scheme provides an accurate solution to the resolved-scale equations; i.e. that the truncation error is small. Otherwise the subgrid-scale model will interfere with the numerical scheme and vice-versa. This coupling can be exploited by considering that the numerical scheme itself can act as a subgrid-scale model; this is the idea behind Implicit LES (ILES).

During the initial phase of the present project, three subgrid-scale models were tested: the Smagorinsky model, the dynamic Smagorinsky model (Smagorinsky coupled with the dynamic procedure) and the WALE model. Comparisons with DNS and experimental datasets were performed to compare the accuracy of the three models for the turbulent backward-facing step flow. The dynamic Smagorinsky model indeed improves upon the Smagorinsky formulation,

although at a high computational cost. The WALE model exhibits the highest accuracy of the three and only represents a modest added cost compared to that of the Smagorinsky formulation. For these reasons, the LES simulations presented in this work use the WALE model.

3.4 LES applied to bluff body flows: a brief review

LES was initiated by meteorologists in the 1960's to simulate the general circulation of the earth's atmosphere (Smagorinsky [127]). The relative success that they encountered encouraged engineers to use LES for the study of simple turbulent flows of interest. Since then, the continuous and steady increase in available computer power and storage has permitted the development of LES for fundamental flow problems. Significant advances have been made both in terms of theoretical issues and with respect to the complexity of the flow cases being investigated.

More recently, LES has reached a sufficient degree of maturity to be applied with confidence to specific applied problems [137]; for example road and rail vehicles (Krajnović [80]), turbomachinery (Eastwood et al. [36]) and weather forecasting (Cullen & Brown [27]). Turbulent flows past bluff bodies, in particular, give rise to complex unsteady phenomena which pose significant problems to RANS methods. This was a strong factor promoting the use of LES to investigate these flows. In this section we give a brief overview of the development of LES to study bluff body flows.

Deardorff [31] pioneered the use of LES for simple engineering flows. His numerical study was applied to plane Poiseuille flow driven by a uniform pressure gradient. His grid consisted of less than 7000 nodes and the near-wall layer had to be modelled. He concluded that this approach to studying turbulence at high Reynolds number was already profitable and that its benefits would grow with increasing computer power.

The 1980's and 1990's saw a fast increase in the number of LES practitioners [133]. First attempts were made at computing flows over sharp-edged obstacles with separated zones and reattachment. Murakami et al. [102] performed an LES of a cubic model inside a channel, representative of the turbulent flow past a building (see figure 3.2a). They compared their solution with experimental results and concluded that LES has great potential to compute the flow around buildings. Werner & Wengle [144] examined the flow over a square rib in-

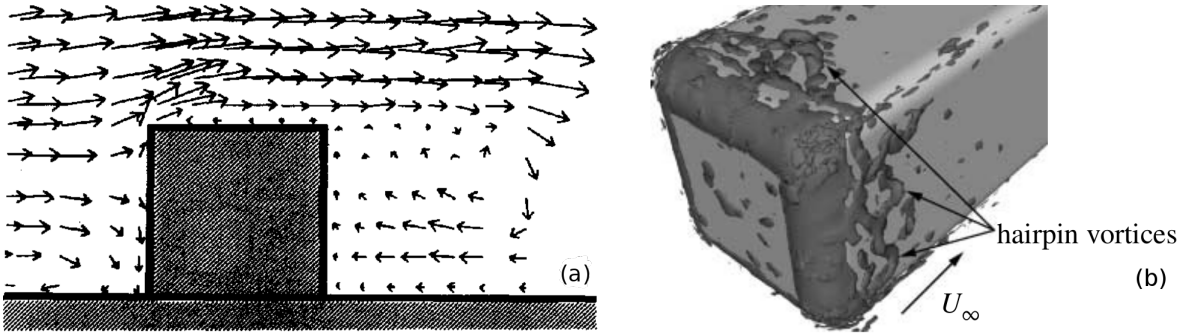


Figure 3.2: Results from an LES of (a) a cubic model inside a channel by Murakami [102] and of (b) a simplified bus by Krajnović [81].

side a channel at a Reynolds of 40000 (based on bulk velocity and obstacle height). They reported good agreement with experimental results for the downstream flow, even though the reattachment length was underpredicted by the LES. Their study was among the first to use information from a separate fully-developed channel flow computation for the inflow instead of the traditional streamwise-periodic boundary condition. Friedrich & Arnal [43] performed a three-dimensional LES simulation of a backward-facing step flow and showed a relatively good agreement with experimental data using a coarse grid.

Rodi et al. [113] reported on a workshop on LES past bluff bodies that took place in Germany in 1995. Three flow cases were considered by the participants: the flow over a square cylinder at $Re = 22000$ and a wall-mounted cube at $Re = 3000$ and $Re = 40000$. Most participants used finite-volume methods together with the Smagorinsky or dynamic-Smagorinsky models. The general conclusion, brought to light by comparison of the different computations, was that good results are not automatic and rely upon numerous factors. It was noted that the wall-mounted cube was generally predicted much better than the square cylinder due to the presence of a transitional region and higher sensitivity to controlling parameters for the latter flow. In addition, the wall models used did not yield very reliable results whilst a high resolution in regions where significant turbulence production takes place was recognized to be important.

The rich dynamics of the circular cylinder flow and wide availability of experimental data have sparked an abundance of numerical computations. Beaudan & Moin [7] were the first to attempt a comprehensive large-eddy simulation of this flow. Breuer [11] also obtained a solution of the cylinder flow at Re=3900, evaluating the impact of numerous parameters, such

as the subgrid-scale model and discretization scheme, on the quality of the results. Unlike sharp-edged bodies, the circular cylinder presents the additional challenge that the location of separation is not exclusively determined by geometry.

Throughout the last two decades, applications of LES have diversified. Today, both sharp-edge and smooth-surface separations are being considered as well as increasingly complex geometries. A parallel trend has been the resolution of the near-wall layer, the development of realistic boundary conditions and of new subgrid-scale models, as well as a steady increase in the Reynolds numbers considered. Relatively simple bluff-body flows that exhibit some of the phenomena observed in industrial applications remain extremely useful in an effort to understand and control these phenomena. Some examples are the curved-ramp (Wasistho & Squires [142]), the two-dimensional hill (Temmerman [133]), the finite cylinder (Fröhlich & Rodi [45]) which contains both sharp-edge and smooth separations and the three-dimensional axisymmetric hill (Krajnović [79]). The flows around simplified vehicles have also been examined successfully in the last decade, albeit not at operational Reynolds numbers. Finally, Krajnović [80] reviews interesting applications performed by his research group: the simplified bus [81] (see figure 3.2b), the Ahmed body [82] and the generic train [55].

3.5 LES solver

3.5.1 Overview

This work employs an in-house parallel LES code called StreamLES to solve the incompressible Navier-Stokes equations [134]. A detailed description and validation can be found in Temmerman [133]. It has been successfully used to simulate transitional separated flow over a compressor blade [85] and turbulent channel flow [135], among numerous other studies.

The procedure is based on a general non-orthogonal grid, block-structured, finite-volume method with fully-collocated storage. Pressure-velocity decoupling, arising from the collocated formulation is counteracted by the Rhie & Chow interpolation practice [112].

The main numerical scheme of the StreamLES solver is described in this section, with the minor additions and modifications that have taken place during this work listed in §3.5.6.

3.5.2 Spatial discretization

Several frameworks exist for discretizing the governing equations in space. The most common are the finite-difference, finite-volume, spectral-element and finite-element methods. Stream-LES uses the finite-volume (or control volume) approach. The domain of interest is subdivided into a finite number of control volumes fixed in space. The equations are then integrated over each of these cells to solve for the unknown flow variables at every cell.

Assuming that the subgrid-scale tensor τ_{ij} is expressed with a model based on the eddy-viscosity hypothesis, the LES equations in integral form become:

$$\int_\Omega \frac{\partial \overline{u_i}}{\partial x_i} d\Omega = 0 \tag{3.15a}$$

$$\int_\Omega \frac{\partial \overline{u_i}}{\partial t} d\Omega + \int_\Omega \frac{\partial \overline{u_i}\,\overline{u_j}}{\partial x_j} d\Omega = -\int_\Omega \frac{\partial \overline{p}}{\partial x_i} d\Omega + \int_\Omega \frac{\partial}{\partial x_j}\left[(2/Re + 2\nu_t)\overline{S_{ij}} - \frac{\delta_{ij}}{3}\tau_{kk}\right] d\Omega. \tag{3.15b}$$

The symbol Ω may denote the flow domain as a whole or any of the computational cells since (3.15) are conservation laws and should be satisfied for any fixed volume within the flow. The deviatoric part of the subgrid-scale tensor is included into the pressure gradient so that the momentum balance can be written more compactly as

$$\int_\Omega \frac{\partial \overline{u_i}}{\partial t} d\Omega = \underbrace{-\int_\Omega \frac{\partial \overline{u_i}\,\overline{u_j}}{\partial x_j} d\Omega}_{C} - \int_\Omega \frac{\partial \overline{p}}{\partial x_i} d\Omega + \underbrace{2\int_\Omega \frac{\partial (\nu_{tot}\overline{S_{ij}})}{\partial x_j} d\Omega}_{D}, \tag{3.16}$$

where $\overline{p}$ stands for $\overline{p} + \delta_{ij}\tau_{kk}/3$, $\nu_{tot} = 1/Re + \nu_t$ and C and D denote the convective and diffusive terms respectively.

The finite-volume method can handle both structured and unstructured grids. The relation between the cells and the grid may be defined as either a cell-centered or a cell-vertex relation [59]. Here, a collocated cell-centered approach is used so that the grid lines define the edges of the finite volumes and the unknowns (p and $\mathbf{u}$) are located at the centroid of the volumes. The values stored inside a cell are held to represent an average over the cell. The essence of the spatial discretization relates to the approximation of the spatial derivatives. In addition, the finite volume method involves two other levels of spatial approximations: the evaluation of the integrals via quadrature formulas and interpolation of nodal variables to the midpoint of cell faces.

Figure 3.3 shows the arrangement of the control volumes on a 2D mesh. Consider a given cell with centroid P and volume Ω_P. Its direct neighbours (where N stands for north, S for south, E for east and W for west) are also depicted. Certain flow properties are also required

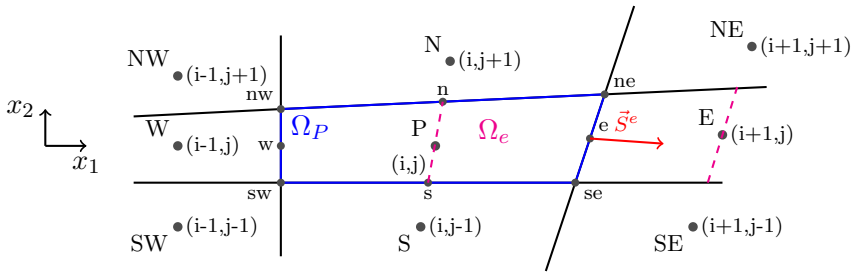


Figure 3.3: Diagram of cell locations for a 2D non-uniform, non-orthogonal mesh.

at the faces of the cell, so the centroid values are interpolated to the midpoints of the faces. The face velocities are stored as mass fluxes since this greatly simplifies the treatment of the convective and diffusive terms. The mass flux through face f (where f=e,w,n,s) is computed as

$$C^f = L(\mathbf{u})|_f \cdot \mathbf{S}^f \tag{3.17}$$

where L is a linear interpolation operator (between the centroids of the two cells sharing the face) and $\mathbf{S}^f = (S_1^f, S_2^f)$ is the vector normal to the face with magnitude equal to its area. For example, the flux through the eastern face of cell P is $C^e = u_1^e S_1^e + u_2^e S_2^e$. In order to reduce memory usage, the code only stores the fluxes at the eastern and northern faces, since the western and southern faces of cell P correspond respectively to the eastern face of cell W and the northern face of cell S.

Let us briefly describe the spatial treatment of individual terms in (3.15a) and (3.16) for cell P. The mass conservation equation represents a constraint that the velocity be divergence-free; i.e. that the net mass flux out of cell P be zero. Using the divergence theorem, mass conservation becomes:

$$\int_\Omega \frac{\partial \overline{u_i}}{\partial x_i} d\Omega = \oint_S \overline{u_i} n_i dS \approx \sum_{f=e,w,n,s} C^f = 0 \ , \tag{3.18}$$

where S is the surface of the cell and n_i is the i^{th} component of the vector normal to the surface. This constraint is not solved directly but imposed via the pressure Poisson equation, as will be explained in §3.5.3.

Since the velocities and pressure stored at P are assumed to represent an average over the cell, the volume integral of the time derivative is approximated as the product of the derivative evaluated at point P with Ω_P,

$$\int_\Omega \frac{\partial \overline{u_i}}{\partial t} d\Omega \approx \left.\frac{\partial \overline{u_i}}{\partial t}\right|_P \Omega_P \ . \tag{3.19}$$

The convective term is approximated by first applying the divergence theorem

$$\int_\Omega \frac{\partial \overline{u_i}\,\overline{u_j}}{\partial x_j} d\Omega = \oint_S (\overline{u_i}\,\overline{u_j}) n_j dS \ . \tag{3.20}$$

A second order midpoint-rule is used to evaluate the surface integral over the four faces of the cell,

$$\oint_S (\overline{u_i}\,\overline{u_j}) n_j dS \approx \sum_{f=e,w,n,s} \overline{u_i}^f\,\overline{u_j}^f S_j^f = \sum_{f=e,w,n,s} \overline{u_i}^f\, C^f \ . \tag{3.21}$$

The discretization of the diffusive term follows the same approach but is slightly more complex because of the second order derivative. The divergence theorem is first applied after which the integral is approximated with the midpoint-rule,

$$\int_\Omega \frac{\partial^2 \overline{u_i}}{\partial x_j^2} d\Omega = \oint_S \frac{\partial \overline{u_i}}{\partial x_j} n_j dS \approx \sum_{f=e,w,n,s} \left(\frac{\partial \overline{u_i}}{\partial x_j}\right)^f S_j^f. \tag{3.22}$$

The derivative at the face needs to be expressed in terms of known velocities and geometric factors. It is written as a volume integral so that the divergence theorem can be applied again and a discrete form is thus obtained:

$$\left(\frac{\partial \overline{u_i}}{\partial x_j}\right)^f \approx \frac{1}{\Omega_f} \int_{\Omega_f} \left(\frac{\partial \overline{u_i}}{\partial x_j}\right)^f d\Omega = \frac{1}{\Omega_f} \oint_S \overline{u_i} n_j dS \approx \frac{1}{\Omega_f} \sum_f \overline{u_i}^f S_j^f \tag{3.23}$$

Here, since the derivative is defined at the face and not at the centroid, a staggered volume Ω_f is considered (drawn as dashed lines for the eastern face in figure 3.3). The staggered surfaces are computed as cell-averages, e.g. $S_j^P = (S_j^w + S_j^e)/2$.

The procedure described above is repeated for every finite volume forming the mesh, with special treatment at the domain boundaries that are mentioned in §3.5.5. Extension of the above to a 3D mesh is straightforward and hence not discussed here.

3.5.3 Time-marching strategy

In LES, the solution at time level n $(\overline{u_i}^n, \overline{p}^n)$ is assumed known and the discrete governing equations are used to compute the solution at the next level $(\overline{u_i}^{n+1}, \overline{p}^{n+1})$. A major difficulty for incompressible flows arises from the fact that the continuity equation does not contain a time-derivative. The constraint of mass conservation is hence achieved via a coupling with the pressure term in the momentum equation.

In StreamLES time-marching is based on the fractional step method [20]. This strategy is made up of two main steps and can be viewed as a splitting of the momentum equation with

a change of variables. An intermediary velocity field $\overline{u_i}^{int}$, related to the true velocity and pressure, is introduced:

$$\int_\Omega \frac{\partial \overline{u_i}^{int}}{\partial t} d\Omega = \int_\Omega \frac{\partial \overline{u_i}}{\partial t}\bigg|^{n+1} d\Omega + \int_\Omega \frac{\partial \overline{p}}{\partial x_i}\bigg|^{n+1} d\Omega \tag{3.24}$$

The momentum equation rewritten for $\overline{u_i}^{int}$ does not include the pressure term explicitly,

$$\int_\Omega \frac{\partial \overline{u_i}^{int}}{\partial t} d\Omega = -\int_\Omega \frac{\partial \overline{u_i}\,\overline{u_j}}{\partial x_j}\bigg|^{n+1} d\Omega + 2\int_\Omega \frac{\partial (\nu_{tot}\overline{S_{ij}})}{\partial x_j}\bigg|^{n+1} d\Omega \ . \tag{3.25}$$

The first step is to solve (3.25) for $\overline{u_i}^{int}$, which is not divergence free. Despite appearances, this step is fully explicit because the convective and diffusive terms at the forward time level are constructed with a third-order approximation based on the known values at previous times. The time derivative is discretized with a third-order Gear-like scheme, shown to possess advantageous stability over a corresponding second-order time-advancement scheme [41].

The second step of the fractional step method is an iterative procedure to compute $\overline{p}^{n+1}$ and $\overline{u_i}^{n+1}$ from $\overline{u_i}^{int}$. Taking the divergence of (3.24) and applying continuity leads to a Poisson equation for the pressure:

$$\int_\Omega \frac{\partial^2 \overline{p}}{\partial x_i^2}\bigg|^{n+1} d\Omega = \int_\Omega \frac{\partial^2 \overline{u_i}^{int}}{\partial x_i \partial t} d\Omega \ . \tag{3.26}$$

The spatial discretization of the pressure term is dealt with in the same way as the diffusive term. Once the pressure is known, $\overline{u_i}^{n+1}$ is obtained from (3.24). The numerical resolution of the elliptic pressure Poisson equation is the most expensive step of the solver, so that the overall efficiency of the code depends on its performance.

The time step $\Delta t = t^{n+1} - t^n$ is limited by two criteria, associated with the convection and diffusion terms, in order to ensure numerical stability. The Courant-Friedrichs-Lewy (CFL) condition imposes that $\Delta t \leq c\Delta/V$, where Δ is the cell volume, V is the local velocity and c is a limit dependent on the numerical scheme. The diffusion constraint requires that $\Delta t \leq d\Delta^2/\nu$, where d is also dependent on the numerical scheme. The time step is determined dynamically at every iteration to ensure that the two stability constraints are satisfied, using $c = 0.25$ and $d = 0.1$ (see Hirsch [59]). Note that the controller implemented into StreamLES requires a constant time step. Consequently, when the control is on, Δt is fixed to the minimum value reached without the control. A routine checks every iteration whether the CFL and diffusion numbers remain below the desired bounds ($c = 0.25$ and $d = 0.1$).

3.5.4 Resolution of the Poisson equation

In discrete form, (3.26) is an algebraic system with a number of unknowns equal to the number of computational nodes. Let us consider a 2D mesh with $m \times m$ nodes and denote the pressure solution of the system at node (i, j) by $\overline{p}_{i,j}$. We can assemble the solution into a vector

$$P = [\overline{p}_{11}, \overline{p}_{21}, ..., \overline{p}_{m1}, \overline{p}_{12}, \overline{p}_{22}, ..., \overline{p}_{m2}, ..., \overline{p}_{mm}]^T.$$

The algebraic system can be written in matrix form:

$$D\,P = Q \tag{3.27}$$

where D is the matrix of the coefficients for the discretization scheme and Q contains the right-hand side terms, including boundary conditions. The direct method consists of solving for P by inverting D, but this is too costly for a realistic CFD problem. The alternative is to use iterative methods, starting with an initial guess P^1 and correcting it by successive sweeps through the mesh until convergence to within a selected accuracy.

StreamLES uses the successive line overrelaxation (SLOR) scheme with an alternate direction implicit technique in which the solution is computed by sweeping alternately in the x_1 and x_2 directions. SLOR is similar to the common Gauss-Seidel method, but instead of going through the mesh point by point, better efficiency is achieved by solving three adjacent points simultaneously with the Thomas algorithm. If, for example, the sweep takes place in the west-east direction, the equation for node P is:

$$d_W\overline{p}_W^{n+1} + d_P\overline{p}_P^{n+1} + d_E\overline{p}_E^{n+1} = (1-\omega)(d_W\overline{p}_W^{n} + d_P\overline{p}_P^{n} + d_E\overline{p}_E^{n}) + \\ \omega[Q_P - (d_N\overline{p}_N^{n} + d_S\overline{p}_S^{n+1} + d_{ne}\overline{p}_{ne}^{n} + d_{se}\overline{p}_{se}^{n} + d_{sw}\overline{p}_{sw}^{n})] \tag{3.28}$$

where all d_x are the discretization coefficients, n is the iteration number and ω is the relaxation factor (set to $\omega = 1.3$ throughout this work). The solver sweeps through the mesh repeatedly until the residual $R^n = |D\,P^n - Q^n|$ becomes small enough.

Conventional iterative techniques tend to damp out the high frequencies of the residual much faster than its low frequencies. This is due to the fact that the largest eigenvalues of the amplification factor of common iterative schemes are often associated with the large-scale perturbations. StreamLES uses the multigrid method to accelerate convergence. Instead of performing a large number of sweeps on the original fine mesh until convergence, only a few sweeps are performed to damp out the highest frequencies. Since the residual has been

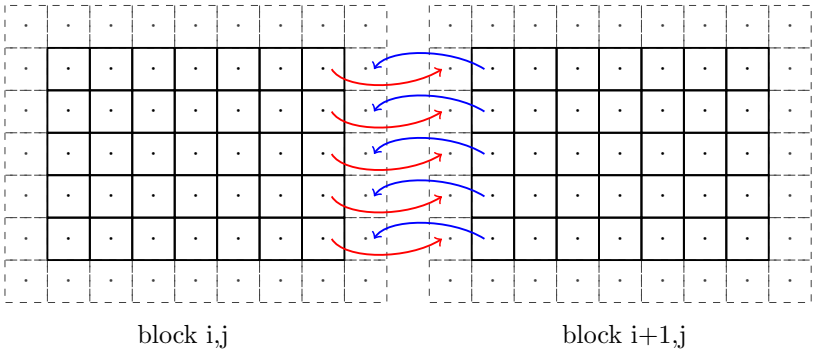


Figure 3.4: Information exchange between two neighbouring blocks.

made smoother, it can be accurately represented on a coarser mesh. Thus a coarser mesh is constructed by removing every other node in each direction of the original mesh. The highest frequencies that can be represented on the coarser mesh are damped out in a few sweeps. Then, an even coarser mesh is constructed and so on until all frequencies of the residual have been damped. Finally the solution is transferred back to the original grid. Note that the inner iterations on the coarser grids are much cheaper than sweeping through the original mesh, which confers the multigrid method its high efficiency. The interested reader is referred to chapter 10 of Hirsch [59] for an excellent account of iterative methods, including descriptions of the SLOR and multigrid techniques.

3.5.5 Parallelization issues and boundary conditions

StreamLES is parallelized via domain decomposition. The flow domain is divided into N_B blocks so that, if N_P processors are available, each processor computes the solution of N_B/N_P blocks. Each block requires information from neighbouring blocks at various stages of the solution. To this effect, the Message Passing Interface (MPI) protocol is used to govern communication between the processors. Extra layers of cells, called halo layers, are available around each block to receive information from neighbours. At internal boundaries between blocks, the flow properties inside halo cells are assigned the values from the last column or row of cells from the appropriate neighbour block, as shown in figure 3.4. For example, the west halo layer of the eastern block is assigned the values of the last cells of the western block and vice-versa. This in turn allows the fluxes on the block boundaries to be computed. When a block has a boundary which coincides with the domain boundary, its halo cells lie outside the computational domain. The halo cells then serve to impose the boundary conditions.

There are essentially three types of boundary conditions applied in StreamLES and all use halo cells: the conditions on the mass fluxes, on the nodal velocities and on the pressure. The mass-flux constraint must always be defined as a Dirichlet condition and reads

$$C = \mathbf{a} \cdot \mathbf{n} \tag{3.29}$$

where $\mathbf{a}$ is a prescribed vector and $\mathbf{n}$ is the surface normal vector. At the inflow, for instance, $\mathbf{a}$ should be set to the incoming velocity, whereas it is set to the zero vector at walls.

Once the end-of-step nodal velocity u^{n+1} and mass flux C^{n+1} are known, one needs to determine the nodal velocity in the halo cells, which are used to compute the convection and diffusion terms in the cells adjacent to the boundary. This is done by solving a 2×2 (3×3 in 3D) linear system arising from the boundary condition. Let us suppose that cell P has its eastern face lying on the domain boundary, so that cell E is a halo cell. $\mathbf{S}^e$ is the vector normal to face e, and $\mathbf{t_1}$ is the tangential vector defined by:

$$\mathbf{S^e} \cdot \mathbf{t_1} = 0$$

Two different linear systems arise according to whether the condition at the boundary is of Dirichlet or Neumann type. For Dirichlet, the system to solve for $\mathbf{u}^E$ is

$$\mathbf{S}^e \cdot \frac{\mathbf{u}^P + \mathbf{u}^E}{2} = \mathbf{S}^e \cdot \mathbf{a}^e \tag{3.30}$$

$$\mathbf{t_1} \cdot \frac{\mathbf{u}^P + \mathbf{u}^E}{2} = \mathbf{t_1} \cdot \mathbf{a}^e \tag{3.31}$$

where $\mathbf{a^e}$ is the vector prescribed at the boundary. Homogeneous Neumann boundary conditions for the tangential component may also be used for slip and symmetry conditions. In this case the system becomes:

$$\mathbf{S}^e \cdot \frac{\mathbf{u}^P + \mathbf{u}^E}{2} = \mathbf{S}^e \cdot \mathbf{a}^e \tag{3.32}$$

$$\mathbf{t_1} \cdot (\mathbf{u}^P - \mathbf{u}^E) = 0 \tag{3.33}$$

Finally, the boundary condition for the pressure is a Neumann condition expressing overall mass conservation for the flow domain:

$$\frac{\partial \overline{p}}{\partial x_i} n_i = 0 \tag{3.34}$$

This condition is built into the discrete Laplace equation.

3.5.6 Additions to the code

A few minor additions and modifications have been brought to StreamLES during the course of this PhD. This is a convenient place to document them briefly.

1. Firstly, a new subroutine (perturb_lws.f) performs the recycling-rescaling procedure of Lund et al. [94] for a flat plate boundary layer. This routine is used to generate an inflow database. It initializes the flow with a turbulent boundary layer using the velocity-defect law of Coles superimposed with random fluctuations and performs recycling (see section 7.2 for more details on the recycling process).

2. Synthetic jet actuation is added as an unsteady mass flux through selected cell faces. An existing momentum forcing routine was also corrected and completed to allow one to consider additional forcing terms in the momentum equation (see define_flow.f).

3. A sensing routine (sensor.f) now permits one to select an array of single or averaged sensors and output time-series to files, every n iterations.

4. Finally, a profiling of the code was carried out in order to identify possible bottle-necks with the computations and parallel communications between processors. As expected, the largest cost is associated with the Poisson solver and the treatment of the convective and diffusive terms. Large arrays in one the most expensive routines (convdif.f) have been reshaped in order to optimize memory allocation for FORTRAN, which is column-major order.

3.5.7 Performance on parallel platforms

The code was ported to four different high-performance computing machines for this work: Concorde, CX1, CX2 and HECToR. Concorde is a small cluster of 64 cores, or processes, run and maintained by the Aeronautics department at Imperial College London (ICL). CX1 and CX2 are the two main clusters at ICL. CX1 is a PC cluster formed of a number of subclusters from Dell, Viglen and Supermicro. CX2 is a massively parallel SGI ICE system with 4120 cores in total. It is dedicated to jobs larger than 64 cores and can accommodate jobs using up to 768 cores. Finally, HECToR (High End Computing Terascale Resource) is the main British national supercomputer, funded by a group of research councils. In its current phase, it is a Cray XE6 system connecting 90102 cores.

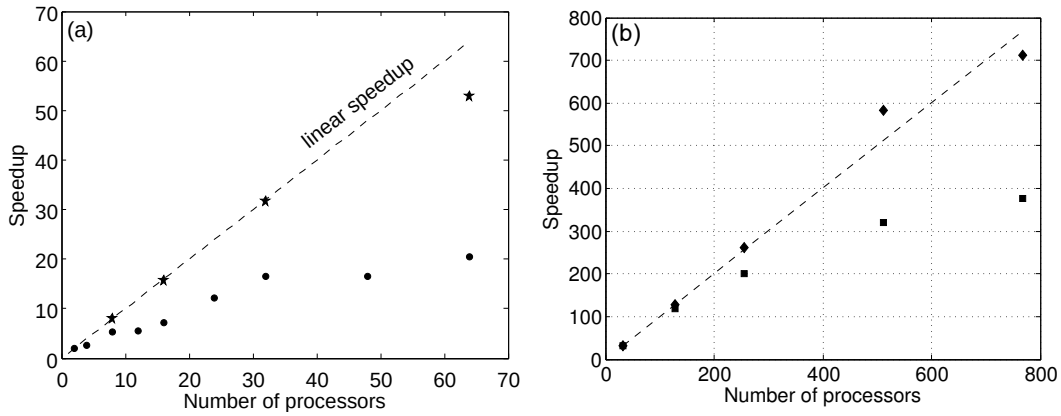


Figure 3.5: Characteristic speedup curves against number of processor cores used for the computation. (a) Speedup for the small problem on CX1 (•) and CX2 (★). (b) Speedup for the small (■) and large problems (♦) on HECToR.

A profiling study was performed on the last three super-computers of this list, in order to evaluate the gain of parallelization. A standard test case of a flat plate boundary layer in two 3D domains is considered. The small domain is formed by $96 \times 48 \times 48$ computational cells and the large domain contains $192 \times 192 \times 96$ cells. A good measure of the scalability of a code for a given problem is the speedup S, defined as:

$$S_p = \frac{T_1}{T_p} \approx \frac{nT_n}{T_p}, \tag{3.35}$$

where T_1 is the execution time of the sequential algorithm and T_p is the execution time for the parallel code with p processors. Here the sequential run time T_1 is approximated by nT_n where n is a small number of processors.

The speedup curves for CX1 and CX2 are plotted in figure 3.5a. CX2 scales very well at least up to 64 processors. On the other hand, the speedup curve for CX1 is less smooth and further off from linearity. This happens because CX1 is a heterogeneous cluster formed of various subclusters with different scales of performance.

Finally, the results of the profiling on HECToR are illustrated in figure 3.5b. The small problem does not scale very well because the relative importance of communications compared to computations is high in that case. On the other hand, the large problem has a linear speedup curve, even achieving super-linear speedup for 512 cores. This effect is associated with a particularly efficient use of cache memory.

Chapter 4

Flows over 2D bluff bodies

This chapter gives a brief overview of some aspects of flows over 2D bluff bodies that are relevant to this work. Although the primary interest here is in bluff body flows, a strong focus is put on reattaching shear layers, and backward-facing step flows in particular, because this is the main test case examined in this thesis. The backward-facing step flow captures the essential unsteadiness in flows around wall-mounted bluff bodies with a blunt trailing edge. Furthermore, it also shares some key characteristics with the recirculation region and wake developing behind a 2D bluff body such as the D-shaped body studied in chapter 9. Therefore, backward-facing step flows are highly relevant to the form-drag reduction problem.

A small part of the extensive literature on reattaching shear layers is reviewed in §4.1, with a strong focus on the backward-facing step flow. In §4.2, we discuss the main instabilities that lead to flow unsteadiness and, to a large extent, dominate the dynamics of the separated region of the flow. These instabilities hence affect the base pressure force significantly and are thus highly relevant for our control problem. This leads us naturally onto a brief analysis of the mechanisms responsible for form-drag in 2D bluff bodies in §4.3. Finally, in §4.4, we review strategies for open-loop forcing of reattaching shear layers.

4.1 Main features of reattaching shear layers

Some salient features of the wake developing behind a downstream-facing step are presented in figure 4.1, adapted from Driver et al. [35]. The incoming boundary layer flow separates at the sharp step corner, forming a free shear layer. If the upstream boundary layer is laminar, the flow transitions promptly, unless the Reynolds number is very low. The flow downstream

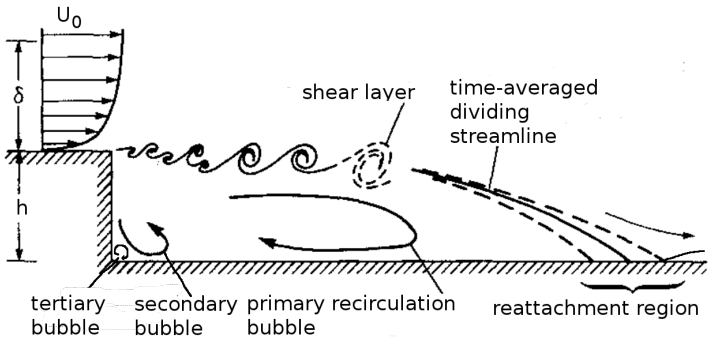


Figure 4.1: Schematic of the flow downstream of a backward-facing step, adapted from Driver et al. [35].

of separation consists of four main regions: a growing shear layer, a recirculation bubble with backflow velocities exceeding $0.2U_0$, a reattachment region and a redeveloping boundary layer downstream of reattachment. In addition, Bradshaw & Wong [10] make a distinction between the original shear layer and the new shear layer (formed at separation) expanding within it. The main features noted above are common to most instances of reattaching shear flows.

4.1.1 Near-separation region

Upstream of the reattachment region, the separated shear layer behaves in some respects similarly to a traditional plane mixing layer [126]. Comparisons of experimental data for mixing layers and reattaching shear layers, including velocity profiles, Reynolds stress profiles and growth rate, have shown good agreement in the region before reattachment (see, e.g., Eaton & Johnston [38]). Troutt et al. [136] have shown that streamwise growth of the shear layer occurs due to pairing of vortical structures aligned in the spanwise direction, as in a plane mixing layer.

An important distinction remains, however; namely that the flow on the low-speed side of the shear layer is highly turbulent. Consequently, the peak streamwise turbulent stress is generally larger in a reattaching shear layer than in a plane mixing layer [10], due to the higher shear. In addition, several studies suggest that the strength and organization of the vortices in the shear layer are modulated by a global low-frequency motion of the bubble. For instance, Kiya & Sasaki [77] proposed that this low-frequency flapping motion is associated with a pseudo-periodic short-term breakdown in the spanwise coherence of the vortical structures forming in the shear layer. Spazzini et al. [129] observed that the secondary recirculation

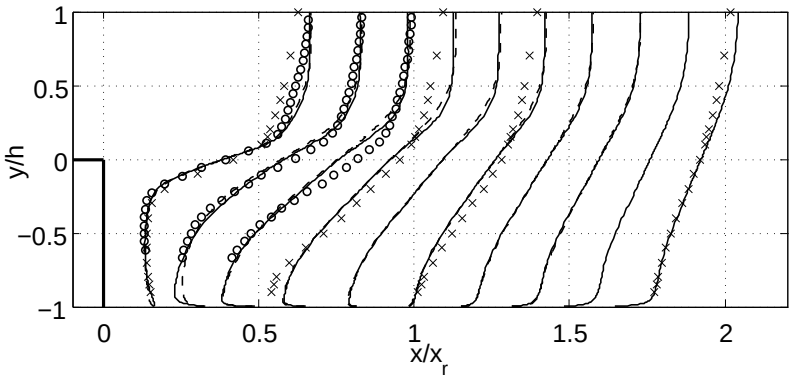


Figure 4.2: Profiles of time-averaged streamwise velocity. $Re_h = 2 \cdot 10^4$ (—); $Re_h = 4 \cdot 10^4$ (----); Brosco [12] (○); Driver & Seegmiller [34] (×).

bubble goes through cycles of growth and intermittent bursts associated with the flapping. The bursts appear to momentarily disrupt the coherence of the near-separation region, including the mixing-layer. The experiment of Hudy et al. [63] provided some new insights, challenging the classic view of mixing-layer-like spatial growth of the shear layer vortices. They observed that coherent structures grow and convect downstream only until midway to the reattachment point, where a large-scale structure starts growing in place and suddenly sheds when it reaches a size $l = O(h)$. These studies reveal complex instantaneous features which are difficult to observe from the time-averaged fields.

4.1.2 Recirculation bubble

The recirculation bubble is subject to strong backflow. This can be observed from time-averaged profiles of the streamwise velocity, as shown in figure 4.2. The agreement between LES solutions at two Reynolds numbers and experimental data shows that the time-averaged velocity profiles are not very sensitive to variations in the flow parameters. The largest region of backflow is observed around $x/x_r = 0.4$ (where x_r denotes the reattachment length), after which the flow starts its recovery and the shear layer reattaches to the lower wall.

Figure 4.3 compares the time-averaged distribution of static pressure along the lower wall for a set of experimental and numerical studies. The scaling proposed by Roshko & Lau [117] is used here, $\tilde{C_P} = (C_P - C_{P,min})/(1 - C_{P,min})$. They claimed that pressure distributions in long separation bubbles collapse under this scaling. Figure 4.3 suggests that this is the case for leading edge separations only (denoted by full symbols). A large scatter exists in the data

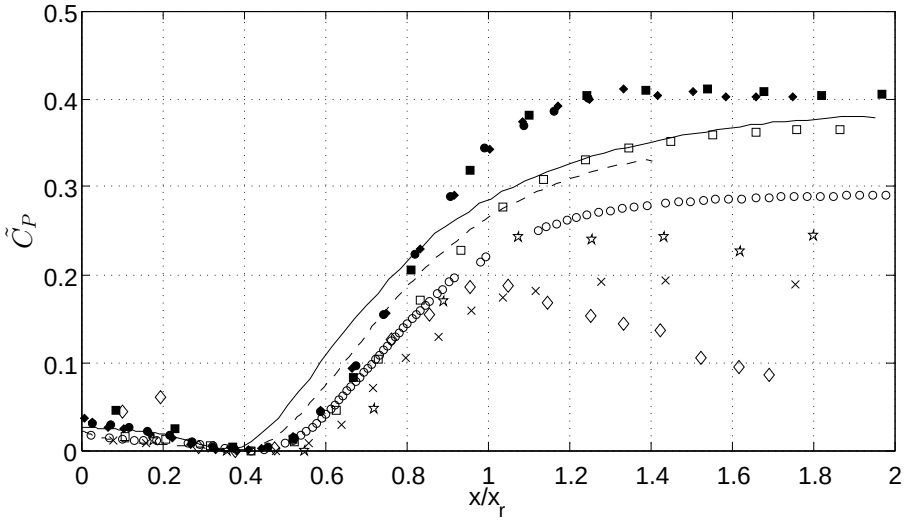


Figure 4.3: Normalized static pressure coefficient $\tilde{C_P}$ along lower wall. $Re_h = 2 \cdot 10^4$ (——); $Re_h = 4 \cdot 10^4$ (----); Hudy et al. [64] (●); Ruderich & Fernholz [119] (■); Cherry et al. [18] (♦); Driver & Seegmiller [34] (×); Hasan [53] (◇); Chun & Sung [21] (□); Le et al. [86] (○); Heenan & Morrison [54] (☆). Full symbols denote leading-edge separation and hollow symbols correspond to backward-facing step flows.

for trailing edge separations. In the latter case the recirculation bubble is extremely sensitive to the details of the boundary layer at separation and, most importantly, the strong pressure gradient is not taken into account by this scaling. Thus, factors that may account for the differences observed are the state and thickness of the separating boundary layer, expansion ratio and differences in methods used to define the reattachment point.

Nonetheless, a qualitative trend common to both leading-edge and trailing-edge separations can be distinguished. Immediately downstream of the step, the pressure coefficient decreases until about $x = 0.5x_r$, where the pressure begins a steep recovery. The recovery zone ends about one or two step heights downstream of reattachment, after which it is not clear whether the wall pressure rises, decreases or remains constant.

Figure 4.4 shows the root-mean-square (RMS) distribution of wall pressure fluctuations, using a new scaling introduced here, $\tilde{C_P}' = (C'_P - C'_{P,min})/C'_{P,max}$. A good agreement in the data is obtained for both separation types, at least up to the peak just upstream of reattachment. This suggests that this scaling is appropriate for long separation bubbles. There is a quiet zone in the region corresponding to the secondary recirculation bubble ($0 \leq x \leq 0.3x_r$) followed by a sharp rise in $\tilde{C_P}'$. The pressure fluctuations fall sharply in the reattached

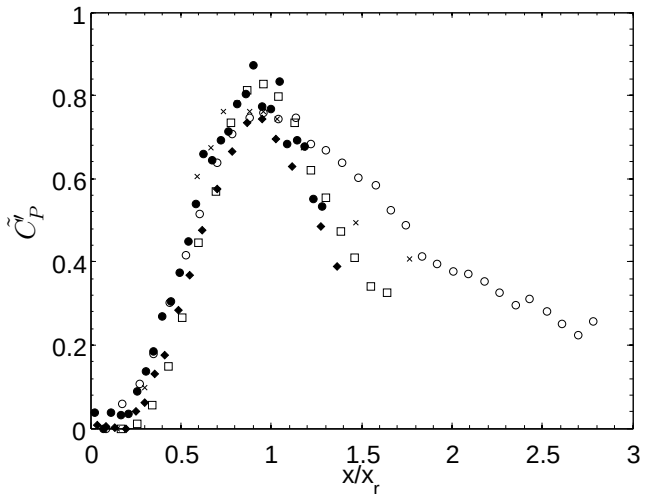


Figure 4.4: RMS pressure fluctuations coefficients $\tilde{C_P}' = (C'_P - C'_{P,min})/C'_{P,max}$ along lower wall. Hudy et al. [63] (○); Heenan & Morrison [54] (□); Driver et al. [35] (×); Cherry et al. [18] (♦); Hudy et al. [64] (●).

boundary layer after reattachment.

4.1.3 Reattachment

As the shear layer grows, the presence of the wall becomes influential and the flow reattaches. In the region near reattachment, a strong curvature and pressure gradient distort the flow and the shear layer ceases to behave like a plane mixing layer. The behaviour of the shear layer approaching the wall has long been subject to controversy and is not fully understood yet. The turbulence intensity and maximum shear stress decrease abruptly close to reattachment, even though the time-mean transverse gradient $\frac{\partial \overline{U}}{\partial y}$ remains relatively constant.

Bradshaw & Wong [10] suggested that the shear layer splits roughly in half at reattachment, with a part being deflected upstream and supplying entrainment to the shear layer near separation. Together with the stabilizing curvature, this could explain the sudden decrease in shear stress. Hasan [53] concluded from his flow visualizations that the shear layer splitting is linked to a sudden upstream burst of the recirculation bubble, which compresses the flow inside the bubble. The bubble then grows again under the pressure of the flow trapped within it. This cycle repeats periodically at a low frequency and forms a feedback mechanism via flow ingested into the bubble at reattachment and fed to the separating shear layer via entrainment. McGuinness [98], however, argued that large-scale eddies do not split, but are alternately swept

upstream and downstream.

A plausible explanation for the sudden decrease in shear stress is that the presence of the wall inhibits vortex pairing [136]. Indeed, Browand & Ho [13] have shown that vortex pairing is an important Reynolds stress generation mechanism in plane mixing layers.

The flow is highly unsteady in the reattachment region and the reattachment location oscillates by up to $2h$ (where h is the step height) around its mean. The length of the separated region varies with the Reynolds number, the state and thickness of the boundary layer at separation, the level of freestream turbulence, the aspect ratio and the expansion ratio of the step. Armaly et al. [5] showed that the reattachment length x_r increases with Reynolds number for a laminar boundary layer, whilst it slowly decreases for transitional flow and becomes independent of the Reynolds number for a fully turbulent boundary layer. High levels of freestream turbulence result in high mixing, a fast growth of the separated shear layer hence a shorter reattachment length. The extent of the separated region x_r seems to increase linearly with the expansion ratio [38]. This conjecture is supported by results from Driver & Seegmiller [34] who found that x_r increases with the level of adverse pressure gradient. The effect of the aspect ratio (channel width/step height) has been studied by de Brederode & Bradshaw [30]. They found that x_r increases with aspect ratio for a laminar separation and the reverse happens for a turbulent separation, though the effect becomes negligible for aspect ratios greater than ten. Finally, the effect of the incoming boundary layer thickness on reattachment length was investigated by Adams & Johnston [1].

4.1.4 Redeveloping boundary layer

After reattachment, the bounded flow readjusts very slowly to a fully turbulent profile, with some features of the separated shear layer still present at $x/h = 50$. This phenomenon has been linked to the persistence of large scale structures being shed from the reattachment region into the bounded flow [136].

4.2 Flow instabilities

Flow instabilities in reattaching shear flows lead to strong unsteadiness and have been recognized to be highly relevant for flow control purposes, in terms of beneficial resonance between unsteady actuation and natural instability modes of the flow. Despite the strong interest that

this issue has generated during the past three decades, our understanding of the natural modes of reattaching flows remains incomplete.

In terms of energy content, the two dominant instabilities recognized in reattaching shear layers are the shear-layer mode and the shedding, or step, mode. The shear layer instability is of Kelvin-Helmholtz (K-H) type and amplifies upstream disturbances in the initial separated shear layer, leading to a mixing layer behaviour. Hasan [53] observed that the shear layer mode reduces to the step mode via a series of vortex pairings. In addition, a global low frequency flapping has also been observed.

Table 4.1 lists values for the three main instabilities from a set of experimental and numerical studies. The shear-layer mode scales with the local momentum thickness, which can be approximated by the momentum thickness at separation θ, and is approximately $St_\theta = 0.01$. The different studies agree well on the shear-layer mode, although Neumann [104] reports a higher frequency.

The vortical structures generated in the shear layer grow by coalescence and entrainment of the surrounding fluid and eventually reach a size close to the step height. The large-scale structures are then abruptly shed from the reattachment region, giving rise to the shedding instability. It can be observed from table 4.1 that there is a rather large scatter in the frequencies reported for this mode, in part due to some confusion in its definition and high levels of turbulence obstructing its visibility at high Reynolds numbers. A large number of workers find non-dimensional frequencies $F^+ \equiv f x_r/U_0$ (where f is frequency in Hertz) scaling with the reattachment length in the range $0.4 \leq F^+ \leq 1$. For the typical range of reattachment lengths, this corresponds to $St_h \approx 0.1$. This value corresponds to half of the shedding frequency observed on bluff bodies with two separating shear layers (on the upper and lower trailing edges). The studies investigating unsteady actuation have generally concluded that the most effective frequency to modify the shear layer growth rate is linked to the shedding mode. However, the frequencies they find exceed the typical range suggesting that the *optimal* perturbation is in fact a harmonic of the shedding. Another factor accounting for the disagreement in the data might be a coupling between the shedding and flapping modes. It seems plausible that the low-frequency flapping mode modulates the shedding and thus gives it a more broadband character.

Finally the absolutely unstable flapping mode has been associated with an imbalance in the feedback mechanism created by fluid pushed into the bubble at reattachment and feeding

Study	Geometry	K-H (St_θ)	Step (F^+)	Flapping (F^+)
Mabey [96]	Review	-	0.6	-
Eaton & Johnston [37]	BFS	0.013	0.52	-
Driver et al. [35]	BFS	-	0.6	0.1
Simpson [126]	BFS	-	$0.6 - 0.8$	< 0.1
Hasan [53]	BFS	0.012	1	-
Neto et al. [103]	BFS	-	0.65	-
Le et al. [86]	BFS	-	0.38	0.16
Huang & Fiedler [61]	BFS	-	0.2	-
Heenan & Morrison [54]	BFS	-	1	0.1
Spazzini et al. [129]	BFS	-	1	0.08
Lee & Sung [87]	BFS	-	0.48	0.1
Neumann [104]	BFS	0.028	0.8	< 0.2
Wee et al. [143]	BFS	-	0.37	-
Liu et al. [91]	BFS	-	0.54	0.16
Cherry et al. [18]	BLE	-	0.7	-
Sigurdson [125]	BLE	-	$0.5 - 0.6$	-
Kiya et al. [78]	BLE	-	0.5	-
Troutt et al. [136]	BFS	-	1.75	-
Bhattacharjee et al. [9]	BFS	-	$1.2 - 2.4$	
Roos & Kegelman [114]	BFS	-	$0.4 - 1.2$	-
Chun & Sung [21]	BFS	0.01	1.95	-
Chun & Sung [22]	BFS	-	3.64	-

Table 4.1: Dominant instabilities in reattaching shear flows. (BFS = backward-facing step, BLE = blunt leading edge separation)

the shear layer upstream by entrainment [38]. The frequencies listed in table 4.1 fall within a relatively narrow range around $F^+ \approx 0.1$, which is roughly an order of magnitude below the shedding mode. The flapping is responsible for a growth-decay cycle of the whole recirculation bubble that leads the shear layer to oscillate vertically. Spazzini et al. [129] observed that the secondary recirculation bubble is linked to this instability. They argued that the large primary bubble creates a jet towards the base of the step. Part of the jet is deflected upwards and feeds the shear layer whilst the other part induces a downwards motion responsible for the anti-clockwise secondary bubble. They further argued that the latter follows cycles of growth and intermittent bursts, causing short-term breakdowns in the spanwise coherence of the vortical structures in the shear layer.

4.3 Bluff body pressure drag mechanisms

For bluff bodies with a blunt trailing edge, pressure drag largely dominates over skin friction drag [3]. The pressure drag force F_{PD} arises from the distribution of static pressure over the surface S of the body,

$$F_{PD} = \iint_S p \, dS.$$

In the case of bluff body flows, an imbalance between high pressure at the front and a low pressure region on the rear side leads to a high value of F_{PD} opposing the body's motion. The shear layers forming after separation are subject to the convective Kelvin-Helmholtz instability. This produces vortical coherent structures entraining low momentum fluid from near the body base and pumping high momentum fluid towards the base. The vortical shear layer structures responsible for this intensive mixing grow by pairing and dissipate energy, causing high losses in stagnation pressure [42]. Entrainment and the pressure difference between the outer and inner regions surrounding the shear layers forces these to curve inwards and interact with each other. This process leads to the creation of a recirculation region and alternative shedding of large vortices.

Roshko [116] discusses the drag and base suction over circular cylinders and bluff plates. He shows that the evolution of base suction with Reynolds number over a cylinder is complex due to several instabilities leading to unsteadiness and three-dimensionality. The movement of the separation point, the shedding (2D or 3D) and the wake dimensions are all affected by the Reynolds number and thereby modify the base suction. He concludes that the available

models for the forces on cylinders or bluff plates are too simplistic; they mostly apply to steady flow without shedding. An excellent discussion on the drag of bluff bodies and road vehicles is provided in [128]. More recently, Choi et al. [19] reviewed general control methods to reduce drag on bluff bodies.

4.4 Review of actuation strategies

A number of studies have focused on active open-loop control of reattaching shear layers with various control targets. For instance, Bhattacharjee et al. [9] used acoustic forcing to affect the spanwise vortices and vortex merging interactions in the separated shear layer. Their results suggested that forcing at a frequency corresponding to the local vortex passage frequency tends to regulate vortex spacing and hence inhibit merging. On the other hand, forcing at a subharmonic tends to enhance the vortex merging process, thereby increasing the spreading rate of the shear layer.

Steady suction or blowing have been considered as control methods to reduce the size of the separated bubble. Uruba et al. [138] used a slot jet with steady suction or blowing at the foot of the step. Their experimental results showed significant reductions in reattachment length for both configurations. In the suction case, the dominant mechanism is the removal of low-velocity fluid from the recirculation region, whilst blowing may supply additional entrainment to the shear layer. However, they noted the high input energy required by this control method.

Pulsating jets are now known to be more energy efficient than steady jets for the control of separated and reattaching shear layers. So far, unsteady active open-loop forcing studies have mainly focused on simple actuation signals. In particular, single-frequency harmonic forcing was used extensively, both as a tool to examine the flow physics and as a direct means for control. For example, Roos & Kegelman [114] studied experimentally the behaviour of coherent structures in a reattaching shear layer, under forcing via an oscillating flap. They noted the organizing influence of gentle forcing, leading to a reduced separated region. Liu et al. [91] examined the influence of local forcing on the wall pressure fluctuations. Double-frequency forcing was considered by Kim et al. [75]. They found that vortex pairing can be controlled by double-frequency forcing, whereas single frequency forcing is ineffective. In terms of open-loop harmonic actuation, table 4.2 shows that there is some level of agreement on the most efficient frequency to enhance the growth rate of the shear layer and hence reduce the

Study	Frequency (St_h)
Bhattacharjee et al. [9]	0.2
Roos & Kegelman [114]	0.29
Chun & Sung [21]	0.27
Liu et al. [91]	0.275
Neumann [104]	0.1

Table 4.2: Most effective forcing frequency for reattaching shear layers.

reattachment length. However, actuation targeting a larger band of frequencies may provide a more efficient mechanism to achieve certain control objectives and may bring some new insights into the dynamics of the reattaching shear layer.

Consequently, one of the aims of the present work is to use feedback control which can systematically target many frequencies simultaneously. As well as eliminating the ad-hoc nature of open-loop forcing, this will allow flow changes to be achieved with robustness to disturbances and with consideration towards efficiency in terms of the actuator input. Zero-net-mass-flux (or synthetic) jets have been favoured in several of the studies cited above, mainly because they do not require any mass influx and thereby eliminate the need for complex internal piping. For this reason the present work relies on synthetic jet actuation.

Chapter 5

Overview

This chapter stands as an overview of the problem setup and also provides a roadmap of the steps involved in constructing the control framework. The numerical test cases that are considered in this thesis are described in §5.1. Then, issues pertinent to the actuators and the sensors are discussed in §5.2. Finally the procedures followed for system identification and control design are explained in §5.3

5.1 Description of test cases

Three distinct computational flow cases are considered in this work, all relating to the two schematics in figure 5.1. The two domains shown are a backward-facing step Ω_1 and a D-shaped bluff body Ω_2. For Ω_1, both a 2D domain and a 3D domain with turbulent separation are investigated. The 2D domain ($L_z = 0$) is considered first, in order to validate the numerical approach and provide an initial evaluation of the feedback control strategy.

The boundaries of the domains are decomposed into $\partial\Omega = \partial\Omega_{in} \cup \partial\Omega_{wall} \cup \partial\Omega_{top} \cup \partial\Omega_{out}$, where $\partial\Omega_{in}$ is the inflow boundary, $\partial\Omega_{wall}$ represents the lower surfaces and the step face modelled with no-slip, $\partial\Omega_{top}$ is the upper surface set with a free-slip condition and $\partial\Omega_{out}$ is the outflow boundary where an advection equation for the velocity is imposed. For the 3D domains, spanwise periodic conditions are imposed on the sidewalls. The dimensions of the 2D and 3D domains for Ω_1 were chosen so as to avoid errors related to a constricted computational domain. The 2D flow is found to be more sensitive to confinement due to the free-slip condition and to the inlet length L_i. Therefore $\Omega_{1,2D}$ and $\Omega_{1,3D}$ have different L_i and L_y dimensions. For $\Omega_{1,2D}$, $(L_i, L_x, L_y, L_z) = (4h, 24h, 9h, 0)$ and for $\Omega_{1,3D}$, $(L_i, L_x, L_y, L_z) = (2h, 14h, 3h, 4h)$.

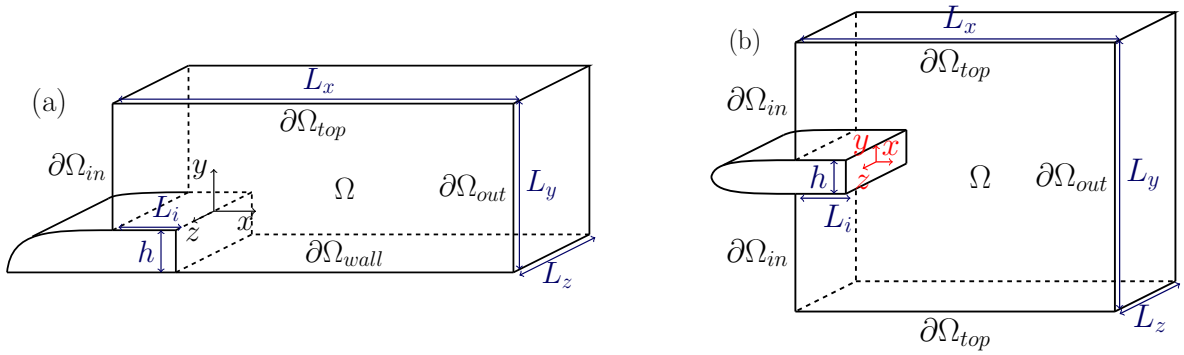


Figure 5.1: The computational domains considered in this work. (a) The first domain Ω_1 is a backward-facing step and (b) the second domain Ω_2 is a D-shaped bluff body with a blunt trailing edge.

Finally, the dimensions of Ω_2 are $(L_i, L_x, L_y, L_z) = (4, 24, 9, 4)$.

5.2 Actuation and sensing

A fundamental consideration in any feedback control strategy is the selection of the actuation-sensing couple. Once this parameter is fixed, there are various routes towards the design of a controller. The type and configuration of actuators and sensors have a strong impact on the control and its limitations.

5.2.1 Actuators

There are a number of actuator types in use in flow control (see, e.g., Cattafesta & Sheplak [16]). In the present work, zero-net-mass-flux (ZNMF) slot jets, also called synthetic jets, are selected. These devices function by ingestion and suction of the working fluid, hence they do not require any external fluid source or complex piping. In addition, various types of drivers and sizes can be used. For these reasons, synthetic jets are a popular choice for experimental flow control.

The dominant flow features and actuator locations for the backward-facing step are shown in figure 5.2. Two actuator locations were examined separately and compared. The first slot jet is located just upstream of the step corner and injected at an angle of 45° whilst the second actuator is placed near the step foot and injected in the streamwise direction. All actuators

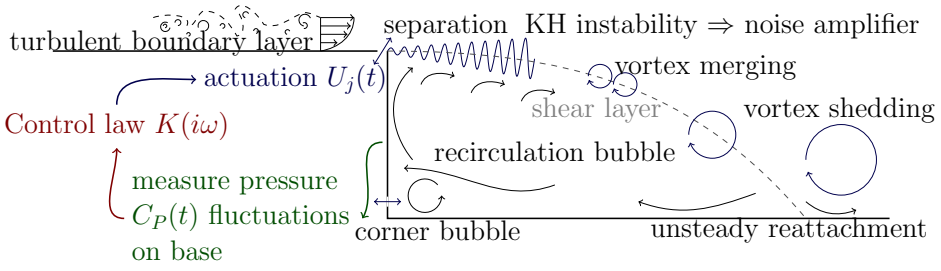


Figure 5.2: Schematic of control configuration and dominant flow features for Ω_1.

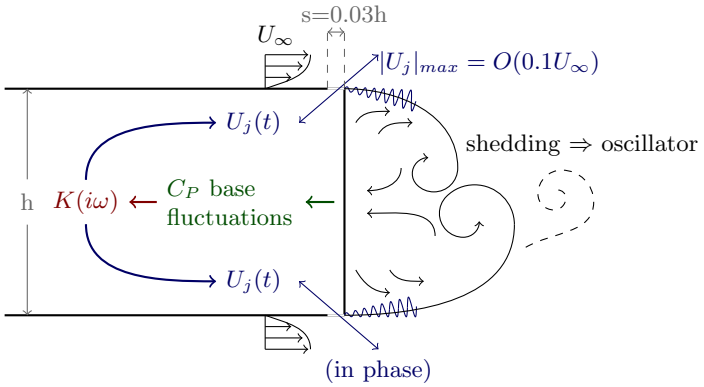


Figure 5.3: Schematic of control configuration and dominant flow features for Ω_2.

extend along the entire domain span and have a slot width $s = 0.03$. For the backward-facing step, the first slot jet is located over $(-0.03 \leq x \leq 0, y = 0)$ and the second is located over $(x = 0, -0.94 \leq y \leq -0.91)$. The first location corresponds to a well-known region of high sensitivity due to amplification of the perturbations by the separating shear layer (see, e.g., Hasan [53], Chun & Sung [21], Yoshioka et al. [147] and Dejoan & Leschziner [32]). On the other hand, the second location has been chosen to examine the effect of the actuation on the secondary recirculation bubble and the resulting impact on the base pressure.

The control configuration for the D-shaped body is sketched in figure 5.3. Here a single actuator placement configuration was tested. Two synthetic jets, at the upper and lower trailing edges, are operated simultaneously and in phase. Again, the width $s = 0.03$ and the injection angle is $45°$ or $-45°$ respectively for the upper and lower jets.

The modelling of the actuators is kept simplistic and the jet cavity is not resolved. The discharge conditions are instead described by an imposed mass flux at the jet orifice with a top-hat spatial velocity profile. This is a numerical simplification which is widely used in the literature [73, 32] and it has been shown that the details of the cavity and the slot are not

critical for slot jets [139, 90]. At least in the case of a laminar inflow, the effects of the jet cavity can be modelled using more sophisticated velocity profiles [4] but this is not considered here. The actuation amplitude A_j is characterized by the maximum ejection velocity at the slot if the actuation signal is periodic. If the actuation signal is not periodic, as is to be expected with closed-loop control, the actuation amplitude is time-dependent and equal to the slot velocity $A_j(t) = U_j(t)$.

5.2.2 Sensors

The choice of the sensing arrangement –including the measured quantity, the number of sensors and their location– depends on the control objectives and on physical constraints. A heuristic method based on POD was introduced by Cohen et al. [23] to find an efficient configuration sufficient for closed-loop control. Here, intuition and practical constraints are deemed sufficient to determine the sensing configuration. Body-mounted sensors are preferred to sensors in the flowfield, because they are more convenient for real-time control in experiments and industrial applications. The sensor measurement should correlate with the target flow quantity, the mean base pressure force, which is to be increased so as to reduce the form-drag.

Investigations of flow control on blunt-based bluff bodies indicate that a reduction in the amplitude of the base pressure force fluctuations is associated with a time-mean base pressure force increase [54, 110]. The present feedback control approach utilizes this hypothesis and aims to attenuate the fluctuations in base pressure force with a view to consequentially increase the mean base pressure force. Hence, the sensor signal $y(t)$ used as input to the controller is the fluctuating part of the instantaneous base pressure, averaged spatially over the step base area; i.e. the base pressure force divided by the base area. Note that the choice of a zero-mean sensor signal is convenient since it will automatically lead to zero-net-mass-flux actuation.

The spatial averaging is done continuously (using all the computational nodes covering the base). In practical applications, however, discrete pressure transducers are used. It is thus important to examine the impact of this averaging. We consider here the 2D and 3D backward-facing step domains. Figure 5.4a shows the evolution, for the baseline flow in $\Omega_{1,2D}$, of the root-mean square of the error $e(t) = y(t) - y_n(t)$, with the number of sensors used for averaging n (y_n denotes the signal obtained by averaging pressure with n sensors). Using a single sensor at the center of the base results in a small error, which falls sharply if more points are used. The continuous average is recovered by using only 8 sensors.

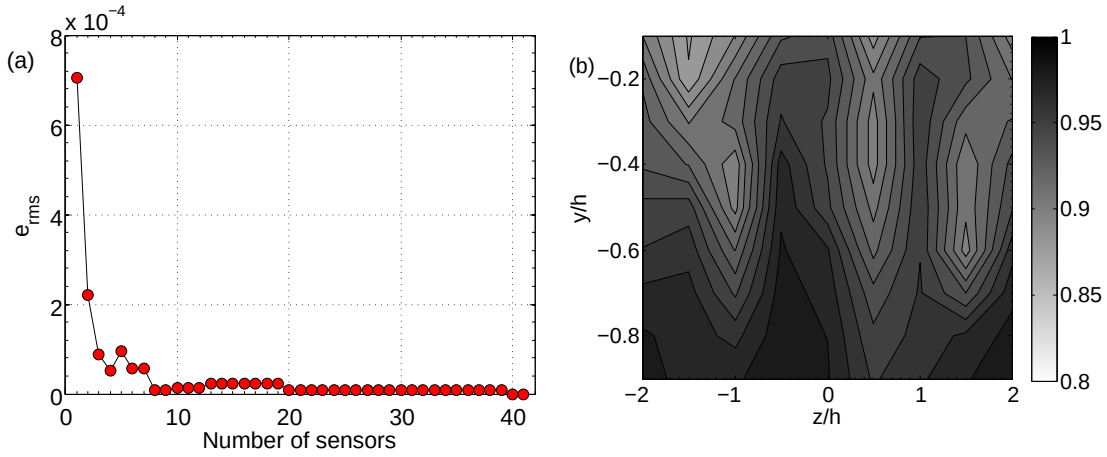


Figure 5.4: (a) Root-mean square of the *error* $e(t) = y(t) - y_n(t)$ against number of sensors, n, for the baseline flow in $\Omega_{1,2D}$. Base pressure averaged continuously in space is denoted by $y(t)$ and $y_n(t)$ is the pressure signal averaged over n uniformly spread sensors on the base. (b) Map of cross-correlation coefficient, for baseline flow in $\Omega_{1,3D}$ between $y(t)$ and single-point pressure signal located at given (0,y,z) position on the base.

For the flow in the 3D backward-facing step, figure 5.4b plots contours of the cross-correlation coefficient between the continuous average and single point sensors on the base. The correlations are everywhere very high which means the continuous average does not hide any important localized structures. Furthermore, it implies that the flow near the base does not see significant 3D effects; this provides support for the use of 2D actuation.

5.3 System identification and control

As mentioned above, a founding pillar of our control strategy is the assumption regarding the link between the fluctuations and time-mean base pressure force on the base. We postulate that attenuating the pressure force fluctuations leads to an increase in the mean pressure force. Note that this key nonlinear phenomenon can not be predicted by our control model. In theory, since the control model is linear, a zero-mean actuation signal can not affect the mean of the sensor measurement. This assumption will be assessed by testing the controller on the non-linear LES simulations of the flow.

The models used for the control design are sketched in figure 5.5. They assume that the fluctuations in the base pressure are caused both by actuation and by disturbances present in

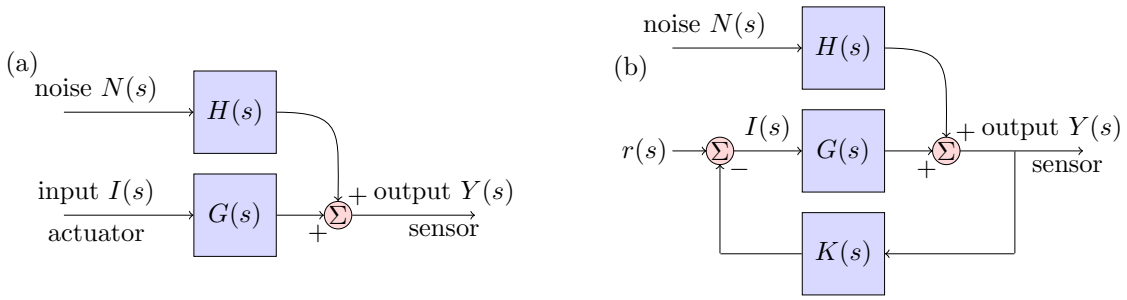


Figure 5.5: Frequency-domain models for the (a) open-loop and (b) closed-loop control systems.

the uncontrolled flow. The latter are collectively represented as *noise*.

$I(s)$, $N(s)$ and $Y(s)$ denote respectively the actuation input, noise and plant output (sensor) signals. Note that s is the complex Laplace transform variable. The input $I(s)$ is the Laplace transform of the actuation signal $U_j(t)$. The noise represents the upstream flow structures which affect the output signal. Finally, the output $Y(s)$ is the Laplace transform of $y(t) = \frac{1}{S_b}\int_{S_b} C'_P(t)\,dS$, where C'_P is the fluctuating part of the pressure coefficient $C_P = 2(P - P_0)/(\rho U_0^2)$ and S_b is the area of the base. $G(s)$ and $H(s)$ are the unknown transfer functions from the forcing input and the noise to the output, respectively. The reference input $r(s)$ is set to zero throughout this work, since we are striving to minimize the output.

Based on figure 5.5, one can infer the ratio of outputs $Y(s)$ with and without control.

$$\frac{Y(s)|_{\text{with control}}}{Y(s)|_{\text{without control}}} = \frac{1}{1 + G(s)K(s)} = S(s). \tag{5.1}$$

As the objective of the feedback control is to reduce the amplitude of base pressure fluctuations, it is clear that the ratio (5.1) needs to have magnitude less than unity. That is, a reduction in the output amplitude can be achieved via a controller $K(s)$ such that the denominator in (5.1) has magnitude larger than 1. This synthesis for fluctuations attenuation translates into a condition on the sensitivity transfer function $S(s)$ to have a gain below unity over the range of frequencies at which the system operates.

Although $H(s)$ does not need to be explicitly evaluated, the design of a feedback controller, $K(s)$, requires a low-order model for $G(s)$, the response of the sensor to actuation. Assuming that the forcing amplitude is sufficiently small for the flow response to be dynamically linear (this assumption will later be checked), this can be achieved via linear system identification [93]. Dynamic linearity implies that sinusoidal input modes are present in the sensor measurement with a gain and phase shift. The latter two may be measured from the LES and they define

the frequency response $G(i\omega)$ as a function of the angular frequency $\omega = 2\pi St_h$.

The gain and phase shift of the response are found using spectral analysis, by expanding the base pressure signal into a Fourier series,

$$C_P(t) = \sum_{n=0}^{N} a_n \sin(\omega_n t) + b_n \cos(\omega_n t), \tag{5.2}$$

and evaluating the magnitude and the argument of the term corresponding to the forcing, $a_f \sin(\omega_f t) + b_f \cos(\omega_f t)$. Given that the forcing frequency ω_f (corresponding to a period $T_f = 2\pi/\omega_f$) is known, the expansion coefficients can be obtained directly:

$$b_f - ia_f = \frac{2}{T_f} \int_t^{t+T_f} C_P(\theta) e^{-i\omega_f \theta} \, d\theta. \tag{5.3}$$

There exist a wide variety of input signals available for system identification (see Ljung [93]). One may, for example, actuate the flow harmonically at various frequencies and measure the gain and phase shift from the sensor output in each case. The main drawback of this approach is that each calculation yields information for a single frequency, so that many computations are required. Although a more economical solution is to select an input signal that contains a range of frequencies, such as a finite-time impulse or a sum-of-sines signal, harmonic forcing holds two important advantages. It allows one to derive physical insight into the effect of the forcing (at specific frequencies) on various aspects of the flow and it also allows weak non-linearities to be characterized via the *describing functions* methodology [48]. Therefore, harmonic forcing is used in the present work for system identification. A linearity check is carried out by forcing at several different amplitude levels and verifying that the gain and phase shift remain within a close bound.

Once a suitable model is available for $G(s)$, a control law $K(s)$ can be built to achieve a set goal. In this work, we mainly use tools from classical control theory, where the control system is analyzed in terms of transfer functions. We resort to frequency-domain tools such as loop-shaping and Nyquist diagrams for stability. These tools will be described further along as they are introduced. Note that the system identification step and the control design tools usually result in continuous-time models or transfer functions. Before implementing such models into the LES, they must be discretized. The transfer functions correspond to ordinary differential equations and there are simple transformations that allow to pass from continuous to discrete time and vice-versa (this will be discussed in section 6.5, and the reader is referred to Jacobs

[68] for more details). Similarly, one may wish to express the plant dynamics as a state-space model in order to apply tools from modern control theory such as linear quadratic (LQ) control. Again, simple transformations allow one to find a corresponding state-space realization for a given transfer function.

We close this chapter with a remark about the numerical implementation of the sensing signal. The fluctuating base pressure signal $y(t)$ needs to be available in real-time to be fed to the controller. But the baseline time-averaged value of the base pressure load is expected to change under the influence of the control, due to the non-linearity of the flow. In order to account for this change, we use an exponentially weighted moving average. Let us consider a discrete-time setting and denote the spatially-averaged base pressure signal, n iterations after the control is turned on, by $\langle C_P^n \rangle_{S_b}$, where $\langle\,\rangle_{S_b}$ denotes spatial averaging over the base. Then we have that the sensor signal $y(n\Delta t) = \langle C_P'^n \rangle_{S_b}$, and we can consider a moving average at iteration n, $\left\langle \overline{C_P}^n \right\rangle_{S_b}$. The exponential moving average is initially set equal to the baseline time-average, and then updated according to

$$\left\langle \overline{C_P}^{n+1} \right\rangle_{S_b} = \alpha \left\langle C_P^{n+1} \right\rangle_{S_b} + (1-\alpha) \left\langle \overline{C_P}^n \right\rangle_{S_b}, \tag{5.4}$$

such that the weighting factors for older data points decrease exponentially. The coefficient α controls the rate of weighting decrease. We use $\alpha = \Delta t/T$, with T set to the characteristic time of the largest scales observable in the baseline flow. This may lead to a rather slow evolution of the average, but it ensures that the low frequencies are taken into account.

Chapter 6

Laminar backward-facing step

6.1 Background

Before considering the turbulent flow cases, a 2D laminar backward-facing step flow is investigated. Although the imposed 2D confinement of the flow prevents the development of turbulence that would arise at the present Reynolds number ($Re_h = 2000$) in a 3D domain, the results provide an initial evaluation of the feedback control strategy targeting the pressure fluctuations.

The configuration is briefly depicted in section 6.2 before studying the baseline flow in section 6.3. We look at the effect of open-loop actuation with synthetic jet forcing in section 6.4. The effect of an unsteady momentum source is also examined. Finally, the control design is discussed in section 6.5.

6.2 Setup

Figure 6.1 illustrates the grid used for the 2D simulations, with only one in every four nodes in each direction shown for clarity. The dimensions of the domain are $(L_i, L_x, L_y, L_z) = (4h, 24h, 9h, 0)$. These dimensions have been chosen so as to ensure that the solution is independent of the domain size, after an extensive sensitivity study. A relatively coarse grid of roughly $24 \cdot 10^3$ computational nodes has been found to suffice to resolve the laminar flow fully.

A laminar Blasius boundary layer profile of thickness $\delta = 1$ is imposed at the inlet. Recall that all quantities are non-dimensionalized by characteristic length and velocity scales (here

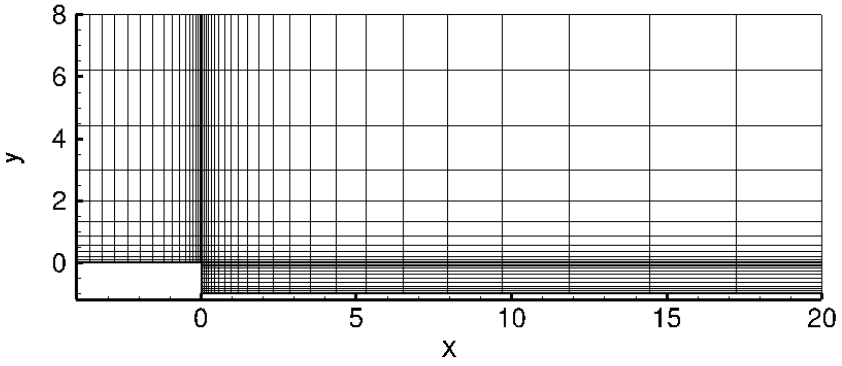


Figure 6.1: Main grid with only one in every four nodes shown in each direction.

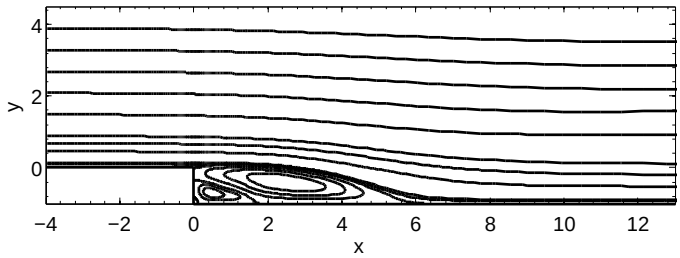


Figure 6.2: Contours of time-averaged streamfunction Ψ.

the step height h and the freestream velocity U_0). Thus, $\delta = 1$ implies a boundary layer thickness equal to the step height. The Reynolds number based on the momentum thickness at separation is then $Re_\theta = 280$. Given that the flow is constrained to remain laminar by the two-dimensionality of the domain, no subgrid-scale model is necessary. The simulation is akin to a DNS, albeit the range of scales is very limited compared to a turbulent flow.

6.3 Flow description and validation

The baseline flow is first examined to elucidate the mechanisms governing the base pressure and to establish a reference against which to contrast the control results. Figure 6.2 shows the time-averaged streamlines for the unforced flow. As described in chapter 4, the shear layer emanating from the step edge grows and rolls up into a large-scale vortical structure under the combined influence of an adverse pressure gradient and presence of the lower wall. Note that both the secondary and a small tertiary bubble are captured. The mean reattachment point is observed at $x_r = 6.1$, corresponding to the location of zero wall shear stress.

The coherent structures of the shear layer and the bubble are known to produce an ob-

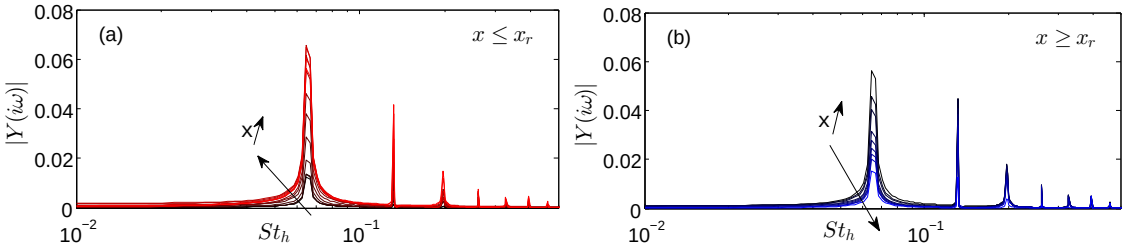


Figure 6.3: Amplitude spectra of pressure along lower wall. (a) Upstream of reattachment and (b) downstream of reattachment. The direction of increasing x is indicated by the large arrows.

servable footprint on the pressure distribution along the lower wall [63]. Pressure signals were recorded at 30 positions along the wall ($y = -1$). The first and last probes are located at $x = 0.1$ and $x = 14.6$ respectively, with a spacing of $\Delta x = 0.5$ between successive probes. The amplitude Fourier spectra of the signals are plotted in Figure 6.3. The data is separated into the regions before and after reattachment to highlight the opposing trends observed. Throughout the domain downstream of separation, the pressure spectra are very similar in shape indicating a strongly dominant mode at $St_h = 0.065$ associated with the shedding of very large-scale structures near reattachment. This frequency corresponds to $F^+ = 0.4$ which falls within the range established in §4.2. Unsurprisingly, the amplitude of this mode grows with x upstream of reattachment and then shrinks back slowly as the reattached boundary layer develops, although the flow is still dominated by the shed structures at the last probe. The bandwidth of the main peak also gets more spread out close to reattachment. Note that there are no fluctuations detected at lower frequencies, indicating that the flapping mode is not relevant in this simulation, because of the two-dimensionality of the domain.

Phase-averaged vorticity was recorded with a period corresponding to the shedding motion. Figure 6.4 shows contours of the vorticity fields for four phases $\phi = 0$, $\pi/2$, π and $3\pi/2$. Again, the dominance of the large-scale structure produced by the shear-layer roll-up is evident. It can be seen that high-momentum fluid from the freestream is entrained by the vortex and pushed into the recirculation bubble, thereby feeding the initial shear layer.

The key flow quantity in this work is the base pressure force. To explore the relation between the base pressure force and the dominant motion of the wake, we examine the phase-averaged base pressure distribution, using the period corresponding to the shedding motion (with the same phase reference as in figure 6.4). Figure 6.5 presents the phase averages for

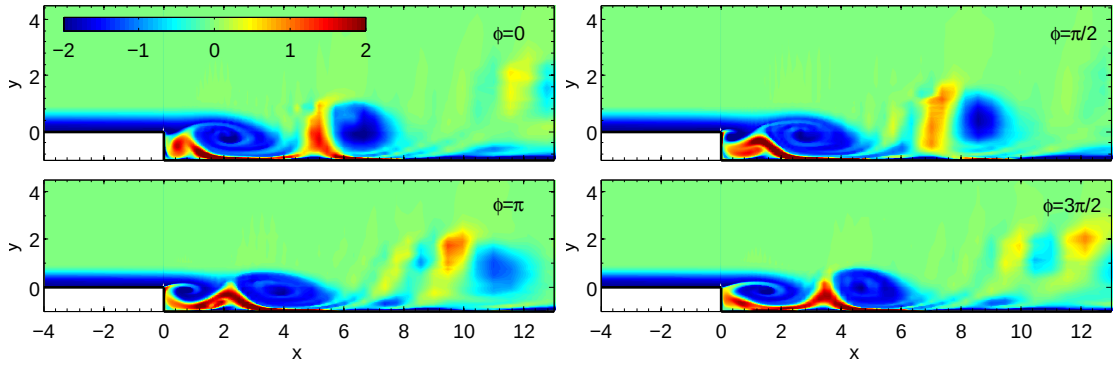


Figure 6.4: Phase-averaged contours of vorticity ω_z.

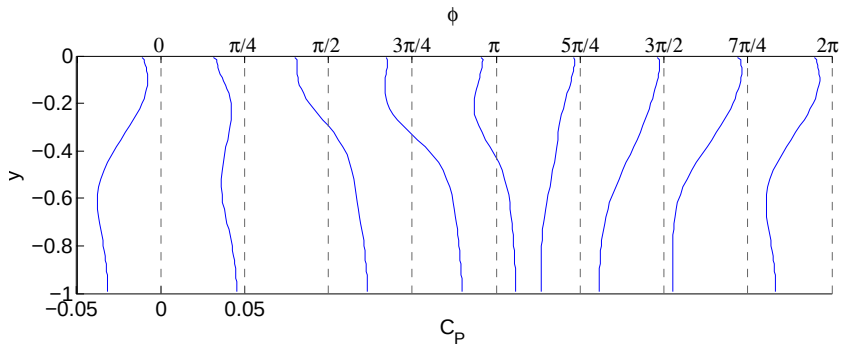


Figure 6.5: Phase-averaged distribution of pressure coefficient $C_P(y)$ on the step base. The vertical dashed lines denote zero pressure for each phase.

9 equally spaced phases between 0 and 2π radians. The bottom abscissa represents $C_P(y)$ and, for clarity, the origin for each curve is shifted by 0.05 with respect to the previous curve. The phase is shown on the top abscissa. For $\phi = 0$, the C_P distribution is low on the whole step, with a maximum at $y = -0.1$, slightly below the separating shear layer. According to figure 6.4, this corresponds to the large-scale (low-pressure) vortical structure towards the latest stage of its growth, sitting close to the base and producing a low pressure in the near-separation region. After reaching a size $l = O(h)$, the vortical structure pulls away from the base, giving way to a progressive increase in base pressure during $0 \leq \phi \leq 3\pi/4$, which we call the convection stage. Two regions can be distinguished on the base during this stage. The lower zone $-1 \leq y \leq -0.35$ sees a rise in pressure due to the distancing of the vortex, whilst the pressure on the upper zone decreases because of the growth of the next vortex. The effect on the lower zone is dominant.

The base C_P reaches an overall maximum around $\phi = 3\pi/4$, when the large structure

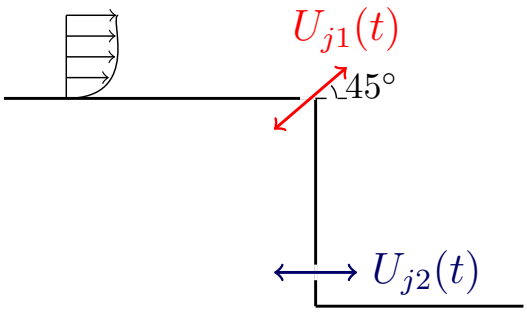


Figure 6.6: Diagram of actuator locations for backward-facing step flow. Not to scale.

abruptly separates causing the recirculation region to contract. This sudden contraction entrains high pressure fluid from the freestream inside the bubble. After the convection stage the next vortex grows by entraining surrounding fluid during $3\pi/4 < \phi < 2\pi$. During the growth stage the base pressure declines. However, note that the pressure in the upper zone increases mildly, due to high pressure fluid being pushed towards the separating shear layer by the main vortex.

6.4 Open-loop forcing

6.4.1 Background

After characterizing the baseline flow, the effect of open-loop harmonic actuation with the synthetic jet is investigated. The two actuation locations described in §5.2, and shown diagrammatically in figure 6.6, are studied and compared. The effect of replacing the jet actuation by a momentum source will be briefly examined, before designing and testing feedback controllers for the main jet configuration with both actuator locations.

6.4.2 Harmonic synthetic jet forcing

The two synthetic jet actuators were forced separately with harmonic signals. The base pressure amplitude spectra for a selection of different forcing frequencies at a fixed amplitude $A_j = 0.2$ are shown in Figure 6.7. This forcing amplitude corresponds to a momentum coefficient $c_\mu = sU_{j,rms}^2/(hU_0^2) = 6 \cdot 10^{-4}$. The flow was left to develop for 15 flow-through times after the start of the forcing to ensure the effects of transients are discarded. A first observation, common to both actuator locations, is that the flow response is strongly dependent upon the jet frequency.

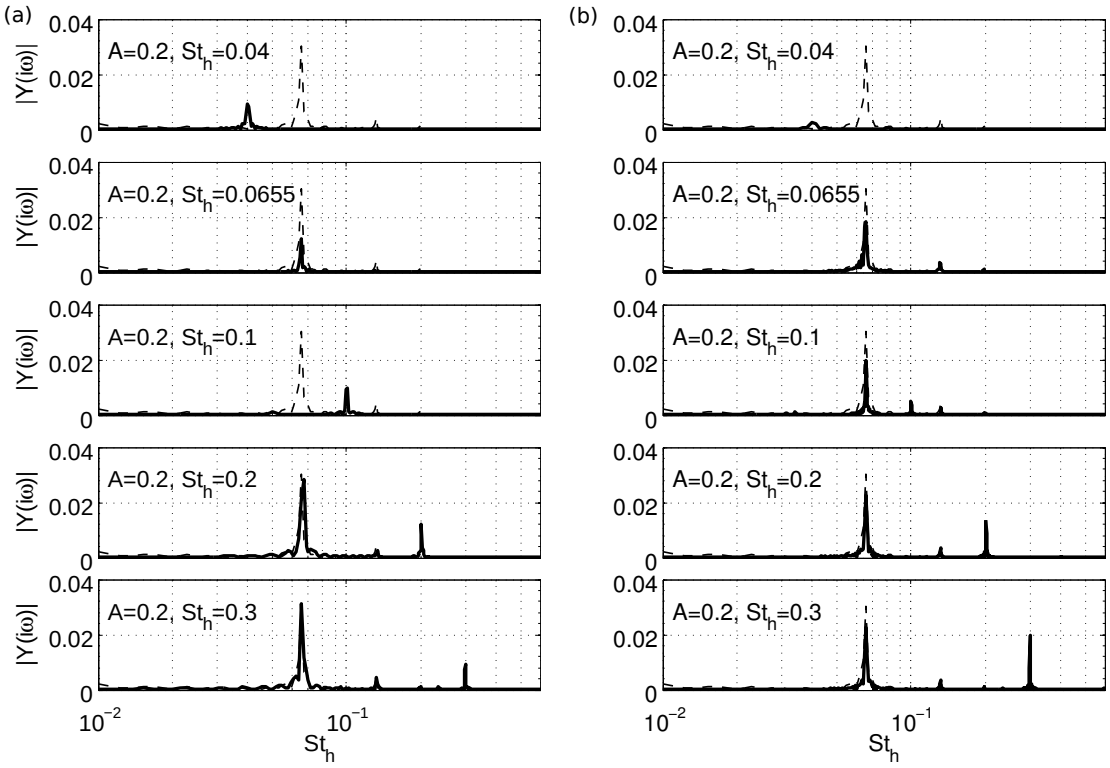


Figure 6.7: Amplitude spectra for open-loop harmonic forcing. (a) Actuator configuration 1 and (b) configuration 2. The unforced spectrum is represented by a dashed line.

At frequencies near the shedding instability, the shear layer locks in to the forcing, after transients. In contrast, frequencies away from the *lock-in* region do not suppress the dominant instability, for the range of amplitudes tested. Instead, a *beating* phenomenon is observed, where both natural and forcing frequency coexist in the flow. As evidenced by figure 6.7 the lock-in range is larger for actuator 1, which acts directly onto the shear layer whereas actuator 2 is buried within the recirculation bubble. Interestingly, the response to actuator 2 appears to increase rapidly with frequency.

The effects of harmonic forcing on the time-averaged base pressure are illustrated in figure 6.8, plotting contours of base pressure change $\Delta\overline{C_P}/|\overline{C_{P0}}| = (\overline{C_P} - \overline{C_{P0}})/|\overline{C_{P0}}|$ against forcing amplitude and frequency ($\overline{C_{P0}}$ denotes the unforced mean base pressure). The first and second actuator locations correspond to plot 6.8a and 6.8b respectively. With both actuators, an increase in base pressure can be obtained at low frequencies, close to the dominant mode.

For actuator 1, a significant increase in C_P is observed when forcing at $St_h = 0.065$, even

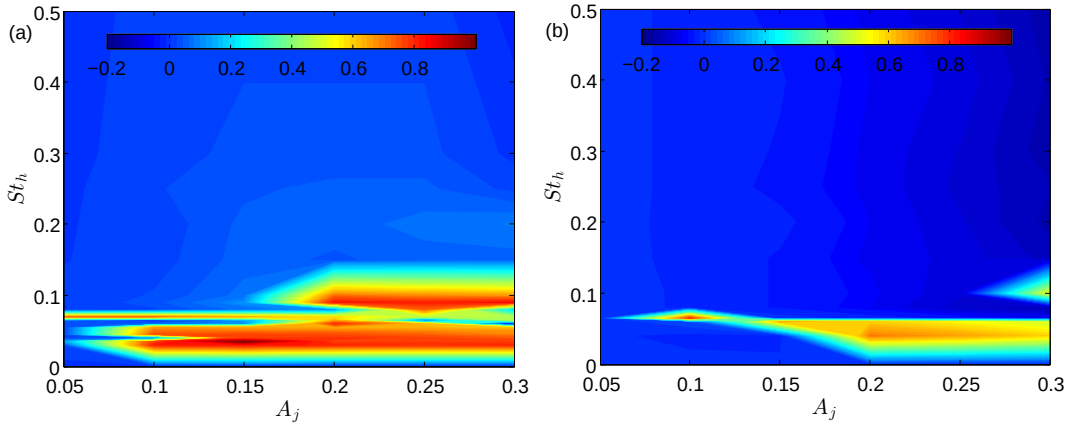


Figure 6.8: Contours of fractional change in time-averaged base pressure, $\Delta\overline{C_P}/|\overline{C_{P0}}|$ against amplitude and forcing frequency for (a) actuators 1 and (b) 2.

with very low amplitudes. This effect seems to saturate at large amplitudes, for $A_j > 0.25$. For $A_j > 0.1$, forcing at the first sub-harmonic leads to a similar ΔC_P. At high amplitudes, roughly when forcing at the dominant mode saturates, the first super-harmonic becomes an efficient means of control.

In all three cases, the increase in base pressure is caused by the suppression of the natural shedding instability, which delays the shear layer roll-up and the reattachment further downstream. There is no indication of a detrimental effect on the base pressure using harmonic forcing with actuator 1 for the 2D flow.

The effect of actuator 2 is qualitatively similar, although the maximum pressure increase is lower. The lock-in obtained with forcing at the dominant mode saturates earlier, for $St_h \approx 0.15$. The super-harmonic forcing has no marked effect until $A_j = 0.3$. Finally, note that high-frequency forcing with $A_j > 0.2$ leads to a reduction in the base pressure.

6.4.3 System identification

The system identification procedure described in §5.3 is carried out for the 2D backward-facing step, with harmonic forcing. For each input frequency, a gain and phase shift can be measured using spectral decomposition, as explained in §5.3.

The time series of the sensor measurement used for the identification are first analyzed and the first 10 domain convection times are discarded to eliminate the effect of transients. The remaining part of the data is divided into equally sized sets. The identification procedure

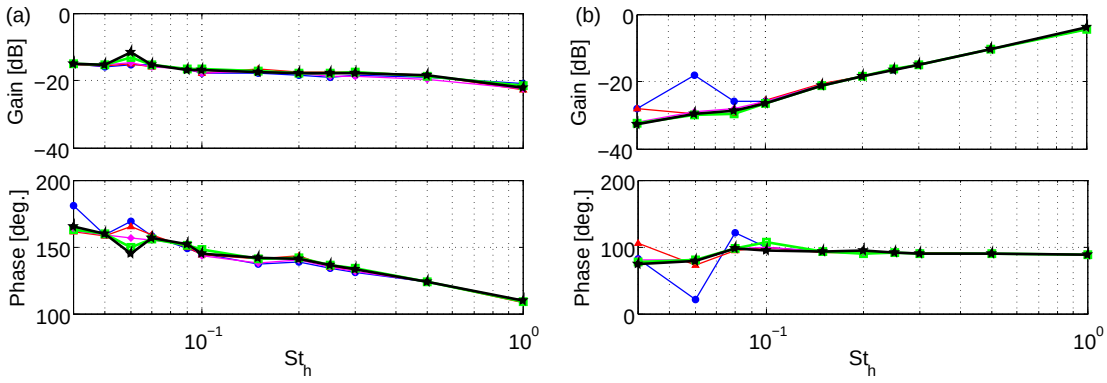


Figure 6.9: Bode plots of frequency response for (a) actuator 1 and (b) actuator 2, for different forcing amplitudes. (●) $A_j = 0.1$; (▲) $A_j = 0.15$; (♦) $A_j = 0.2$; (■) $A_j = 0.25$ and (★) $A_j = 0.3$.

is carried out on each set independently and the results are compared to ensure that a good convergence is obtained. Five different forcing amplitudes are tested to check the linearity assumption. The gain and phase shifts corresponding to both actuator locations are shown in Bode plots in figure 6.9. The different markers correspond to the different control amplitudes A_j. For a perfectly linear system, gain and phase shift do not vary with A_j.

For actuator 1, some weak non-linear effects are observed around the dominant instability $St_h = 0.065$. An increase in amplitude A_j leads to an increasing gain, causing a small peak to appear at the instability, and a reduction in phase (a larger phase lag). Away from this frequency, the dynamic linearity assumption holds very well. Within the range of amplitudes considered, the change in gain and phase shift remain small. The largest difference in gain measured is 3dB and the largest phase discrepancy is 24°.

For actuator 2, some large variations in gain and phase occur near $St_h = 0.065$, but non-linearities disappear for higher frequencies. The largest differences in gain and phase are 10dB and 60°. Nevertheless, the discrepancies seem to fade for amplitudes $A_j > 0.1$. We deem that a linear model may represent the flow response sufficiently well for successful control. Safety margins will be required in terms of stability (gain and phase margins) and performance (sensitivity) to account for the non-linearities.

The gain and phase information obtained above are averaged over the five forcing amplitudes. The resulting open-loop responses corresponding to both actuator locations, $G_{actu1}(i\omega)$ and $G_{actu2}(i\omega)$, are summarized in figure 6.10. The raw gain and phase averages are denoted

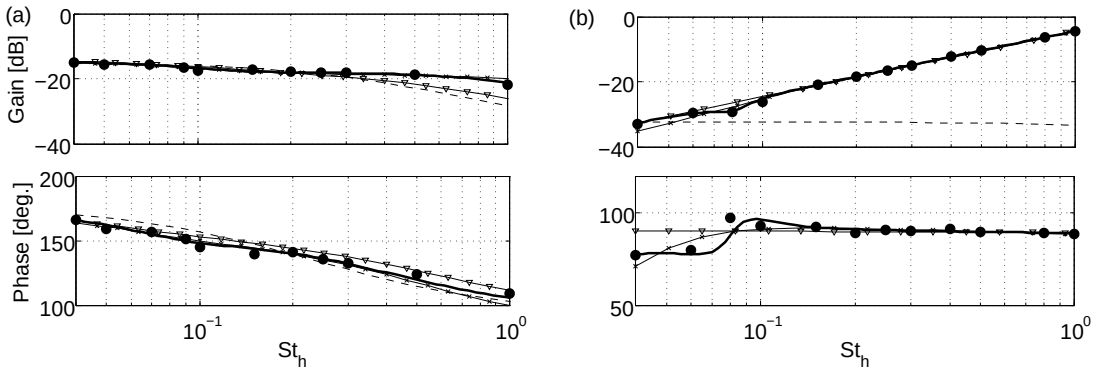


Figure 6.10: Frequency response for (a) actuator 1 and (b) actuator 2. (•) Harmonic forcing; ····· 1^{st} order fit; —▽— 2^{nd} order fit; —×— 3^{rd} order fit; ——— 4^{th} order fit.

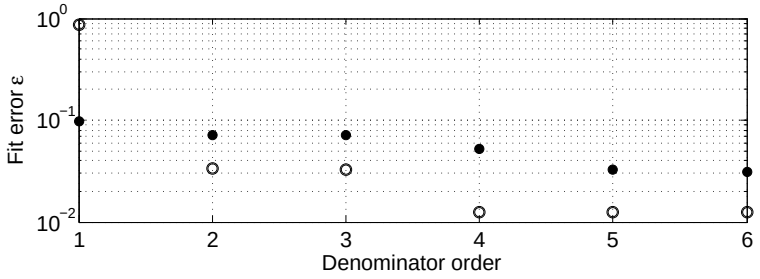


Figure 6.11: Measure of the quality of the fits against denominator order of the fitted transfer function. (•) Actuator 1 and (◦) actuator 2.

by circles. The lines show low-order models obtained by fitting four transfer functions (of denominator order one, two, three and four) to the data via least-squares approximations. We use the *fitfrd* MATLAB command, which is part of the system identification toolbox [92]. There are several ways to measure the quality of the fits. Here, we compute the Euclidean norm of the difference between the raw data G_{raw} and a given fit G_{fit}, given by

$$\epsilon = \left[\sum_{k=1}^{K} |G_{raw}(i\omega_k) - G_{fit}(i\omega_k)|^2 \right]^{1/2}$$

Figure 6.11 plots the evolution of ϵ against the order of the fitted transfer function. For the first actuator location, the second-order fit provides a good match, while the fourth-order fit is chosen for the second location. The fit equations are as follows:

$$G_{actu1}(s) = \frac{-0.154s - 0.0235}{s^2 + 1.776s + 0.168} \tag{6.1}$$

$$G_{actu2}(s) = \frac{-745.5s^3 - 148.4s^2 - 195.3s - 7.25}{s^4 - 27.89s^3 - 7758s^2 - 1705s - 2029} \tag{6.2}$$

For actuator 1, the transfer function is minimum phase (i.e. it has neither poles nor zeros with a positive real part) and has relatively flat dynamics, acting as a low-pass filter with a constant gain drop rate of 20 dB decade^{-1} at high frequencies. As already noted from figure 6.7, the response to actuator 2 has a gain increasing with frequency. Note that the transfer function G_{actu2} is strictly proper, which implies that the gain falls off at larger frequencies. In this case, the behaviour at frequencies $St_h > 1$ is not relevant to the dynamics of the true system, since the range of scales existing in the flow are confined to lower frequencies. Importantly, a phase increase is observed across the shedding instability, corresponding to an unstable pole which will need to be stabilized by the controller.

6.4.4 Momentum source

Before going on to discuss the control synthesis, we propose here a brief interlude to examine the effect of a pure momentum volume source on the 2D flow. The interaction between the synthetic jet and the cross-flow leads to a net positive injection of momentum and vorticity into the flow. The action of the jet can be viewed as an extra source term in the equations of motion. Here we focus solely on a term added to the momentum equation. The two questions we would like to answer are:

- Can we can recover the shape of the frequency response obtained with the jet by using only a momentum source for control?
- How does the direction of the forcing term impact the flow response?

Starting from equation (3.16), a volume source can be added to the momentum balance as follows:

$$\int_\Omega \frac{\partial \overline{u_i}}{\partial t} d\Omega = -\int_\Omega \frac{\partial \overline{u_i}\,\overline{u_j}}{\partial x_j} d\Omega - \int_\Omega \frac{\partial \overline{p}}{\partial x_i} d\Omega + 2\int_\Omega \frac{\partial (\nu_{tot}\overline{S_{ij}})}{\partial x_j} d\Omega + \int_\Omega f_b d\Omega, \tag{6.3}$$

where f_b is a momentum source per unit volume. This extra term is implemented into the LES. The synthetic jet is turned off and replaced by a solid boundary. In its place, the momentum forcing is activated, only in the location of the first synthetic jet actuator, near the step edge. This new actuation corresponds to a force acting on the flow through the wall.

System identification is carried out with an unsteady momentum forcing term with zero mean. Figure 6.12 shows a Bode plot of the frequency response obtained for three forcing terms:

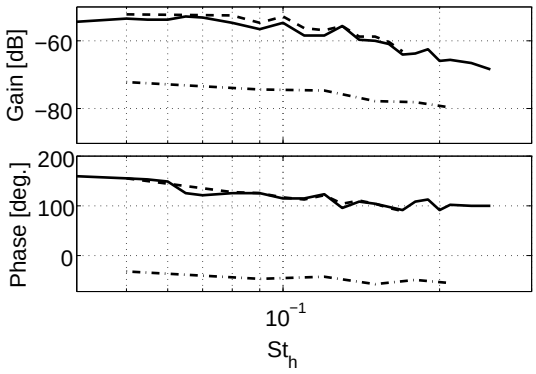


Figure 6.12: Frequency response for forcing in x, y and diagonal directions. ——— $\mathbf{F_{xy}}$; ---------- $\mathbf{F_x}$; ····· $\mathbf{F_y}$.

$\mathbf{F_x}$, $\mathbf{F_y}$ and $\mathbf{F_{xy}}$. These have the same amplitude, but are oriented in different directions (0°, 90° and 45° respectively, with respect to the streamwise direction).

The gain and phase plots are qualitatively similar to that for the jet in figure 6.10a. The value of the gains are different due to the scaling of the input variables (it is difficult to compare gains directly because, in the case of the jet, the momentum depends on the local cross flow velocity). On the other hand, the phase lags for $\mathbf{F_{xy}}$ and $\mathbf{F_x}$ are quantitatively close to the values obtained with the jet. As for direction, the vertical forcing F_y has a low gain and a large phase lag, whereas the other two terms have very close responses. This suggests that it is the streamwise component of the injected momentum that impacts the flow most. Further, this implies that the most common forcing configuration for open-loop control of backward-facing steps –using 45° forcing similar to the first configuration U_{j1} considered in the present work– is superior to vertical forcing but still may not be the most efficient choice. This finding should be verified experimentally, or with highly resolved simulations including the full jet cavity, and may help to inform future actuator design.

6.5 Feedback control

In light of the measured open-loop responses from figure 6.10, simple controllers are designed, targeting a reduction in the fluctuation levels. The disturbance attenuation technique described in §5.3 is invoked, based on the magnitude of the sensitivity function. The loop-shaping technique is used to obtain the desired distribution of $S(i\omega)$. It consists of designing the behaviour of the closed loop system by shaping the open-loop return ratio $L(i\omega) = G(i\omega)K(i\omega)$.

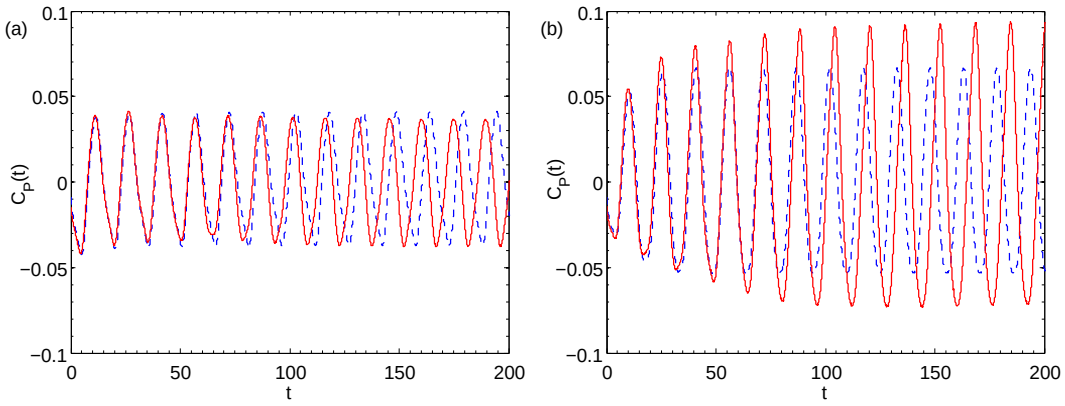


Figure 6.13: Time-series of sensor signals in response to simple controllers aiming at (a) a reduction and (b) an increase in fluctuations amplitude. Both controllers operate via the first actuator location. Linear control theory ---------; LES results ———.

It is also ensured that the controller satisfies closed-loop stability, using a Nyquist diagram [106]. Similarly to loop-shaping, the Nyquist stability criterion allows one to deduce closed-loop properties from the behaviour of the open-loop transfer function $L(i\omega)$. The basic idea is that the system starts to behave like a positive feedback when the phase lag of $L(i\omega)$ reaches $-180°$. If the gain is greater than unity when this happens, then the closed-loop system is unstable. On an Argand diagram of $L(i\omega)$ (a Nyquist diagram), this translates into the condition that the number of encirclements of the -1 point in the anticlockwise direction should equal the number of unstable poles of $L(i\omega)$.

Figure 6.13 compares predictions from linear control theory to LES results for two simple controllers designed to mildly reduce and increase the fluctuations respectively. The controllers are activated at time t=0. An excellent match is observed at initial times between LES and linear theory. However, non-linearities which are not taken into account by the model cause a small shift in frequency. This results in the LES lagging the theoretical response when the fluctuations are reduced and leading it when the fluctuations are increased. In addition, the LES does a better job than predicted at reducing or increasing the fluctuations. This correlates with our earlier observation that the frequency response gain increases slightly with forcing amplitude. These effects can be mitigated by a robust controller and a conservative design for the stability of the closed-loop system.

A second order polynomial controller $K(s) = 1/(s^2 + 2\xi\omega_n s + \omega_n^2)$ is selected for both

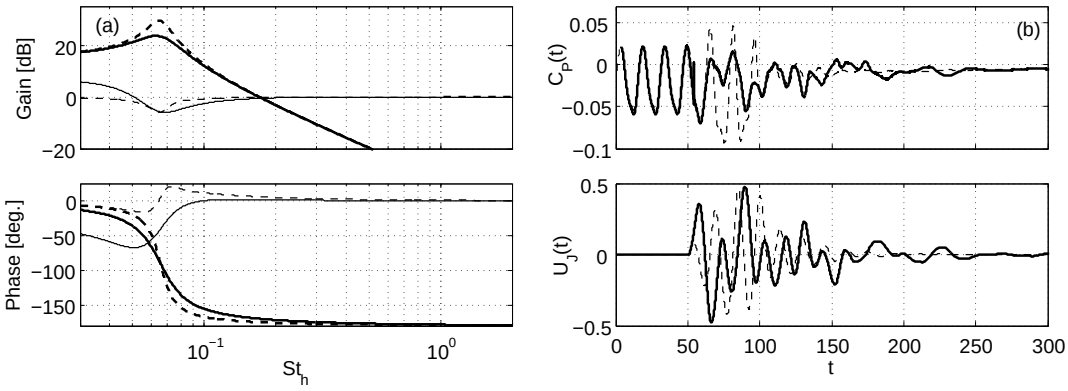


Figure 6.14: (a) Characteristics of closed-loop systems for both actuator locations. The gain and phase of the controllers K are shown as thick lines whilst thin lines represent sensitivity function S=1/(1+GK). (b) Time variations of input $U_j(t)$ and output $C_P(t)$ (including the mean component) for the controlled system. Solid and dashed lines refer to actuators 1 and 2 respectively. The controllers are turned on at t=50.

actuator locations and is implemented in the LES code. The controller must be discretized before its implementation; i.e. it must be expressed in terms of the complex z-tranform variable z. The mapping of the s-plane to the z-plane is given by

$$s = \frac{1}{\Delta t} \ln z. \tag{6.4}$$

Tustin's method, used in the present work, consists of approximating (6.4) by the following expression:

$$s \approx \frac{2}{\Delta t} \frac{z-1}{z+1},$$

which leads to a conversion to the discrete transfer function K_d with time step Δt given by

$$K_d(z) \approx K\left(\frac{2}{\Delta t}\frac{z-1}{z+1}\right). \tag{6.5}$$

More details on the correspondence between continuous and discrete transfer functions or dynamic equations can be found in Jacobs [68].

The resonant frequency is set to the dominant instability $\omega_n = 2\pi \times 0.065$ and the damping coefficients $\xi = 0.2$ (actuator 1) and $\xi = 0.1$ (actuator 2) are chosen to ensure that the actuation signal does not deviate far off from the *linear* range of forcing amplitudes.

Some of the characteristics of K are shown in figure 6.14a, where the sensitivity gain can be observed to be below unity around the shear layer instability frequency. Both actuator

locations produce a similar response by stabilizing the near-wake and pushing the unsteady reattachment region further downstream. The stabilizing effect of the controller was expected since disturbance attenuation and stabilization are closely linked in control theory. After transients the base pressure oscillations are completely suppressed (figure 6.14b). This leads to a 70% increase in the time-averaged base pressure. Thus, in these 2D BFS simulations, feedback control targeted at reducing fluctuations in the base pressure has indeed resulted in a form-drag reduction. In closed-loop, the work done by the actuator adapts to the evolution of the flow (here, for example, requiring only minimal input once the flow has been stabilized) which is a distinct advantage over the open-loop.

6.6 Summary

In this chapter, we considered the 2D backward-facing step flow at $Re_\theta = 280$, as a preliminary test case. This was with the objectives of validating the numerical simulations and testing the system identification procedure and the control strategy.

Linear feedback controllers were designed, which used the sensitivity transfer function to attenuate fluctuations in the base pressure force. These controllers successfully damped the fluctuations, even though the flow response exhibited weak non-linearities close to the natural instability frequency. The near-wake flow was stabilized and the shedding pushed away from the base. A concomitant increase of 70% in the base pressure force was obtained, providing initial validation of our control strategy which exploits the link between base pressure force fluctuations and mean.

Chapter 7

Turbulent backward-facing step

7.1 Background

We now consider the more physically representative 3D backward-facing step flow (see figure 5.1a), with a turbulent inflow boundary layer at $Re_h = 2{\cdot}10^4$, corresponding to $Re_\theta = 1500$. A similar procedure as for the 2D flow is followed. Given that the dynamics of the 3D turbulent flow are richer, the flow physics are discussed in more detail. We start by detailing the procedure to generate the turbulent inflow boundary condition in §7.2 and the validation of the domain size and the grid in §7.3. Then, in a similar manner to the path followed in the previous chapter, we examine the baseline flow in §7.4, harmonic forcing and system identification in §7.5 and closed-loop control in §7.6.

7.2 Inflow generation

The treatment of inlet boundary conditions for LES often bears a strong influence upon the fluid behaviour within the domain, and thus requires special attention. The complexity of imposing a turbulent inflow stems from the need to specify a stochastically-varying component which resembles turbulence.

Broadly, there are three main sets of methods. The first one is the trivial solution; i.e. imposing a laminar solution upstream and using a very long domain to leave enough space for the flow to transition. Artificial perturbations or roughness elements may be added to accelerate transition. Nevertheless, this method generally proves to be a too costly venture. The second set encompasses the so-called synthesis methods, whereby a model is designed for

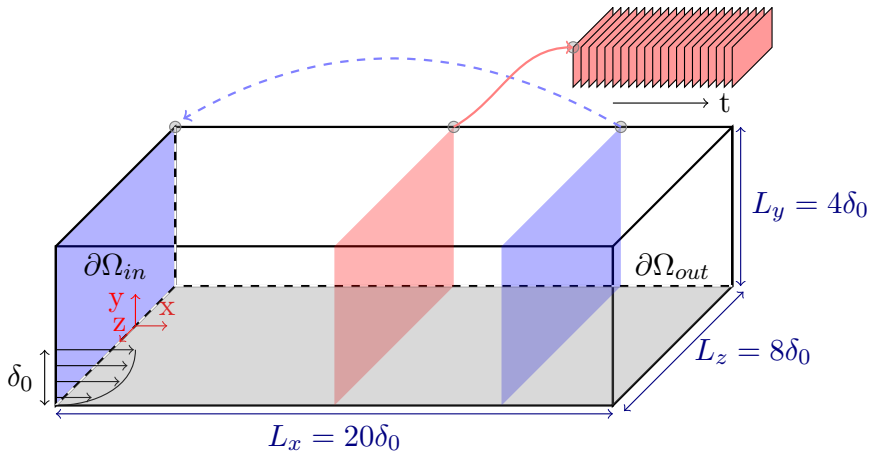


Figure 7.1: Schematic of precursor boundary layer simulation with recycling. The velocity field in the recycling plane (blue) is rescaled and imposed at the inlet, while the velocity in the database plane (red) is saved to a database that will be fed to the main simulation.

the inlet fluctuations based on certain constraints (e.g. Fourier techniques) or reconstructed from a limited number of realizations from experimental or DNS data (e.g. POD methods). Synthesis methods allow a flexible specification of parameters of the inflow turbulence, such as length scales or energy levels. But they remain inherently inaccurate and therefore still require a relatively long inlet section to allow true turbulence to develop [131]. Finally, precursor methods rely on a separate simulation to generate a database which is fed to the main computation. Fully developed turbulence can hence be obtained directly at the inlet. In addition, the database need only be generated once and can then be reused for many simulations.

In the present work, the turbulent boundary layer imposed at the inflow was generated with a precursor method, following the recycling technique of Lund et al. [94]. The precursor simulation computes a zero-pressure-gradient boundary layer developing along a flat plate, as illustrated in figure 7.1. The core idea of this method, assuming self-similarity, is to extract the velocity field from a yz-plane plane downstream (the recycling plane), rescale it and then reintroduce it as a boundary condition at the inlet. The rescaling operation is necessary to account for the growth of the boundary layer between the inlet and recycling planes.

The initial condition in the flow domain is imposed by decomposing the velocity field into a mean and fluctuating part. The mean profile is constructed based on the velocity-defect law of Coles [24]:

$$\frac{\langle U \rangle}{u_\tau} = f_w\left(\frac{y}{\delta_\nu}\right) + \frac{\Pi}{\kappa} w\left(\frac{y}{\delta}\right) \tag{7.1}$$

where u_τ is the skin friction velocity, f_w is the law of the wall, δ_ν is the wall unit, κ is the von Kármán constant, $w = 2\sin^2(\pi y/(2\delta))$ is the empirical wake function and Π is the wake strength parameter whose value is flow dependent. Random perturbations are superimposed to this profile to prevent relaminarization. The precursor simulation is then marched forward in time. At each time step, the velocity fluctuations (with respect to a moving average) in the recycling plane are rescaled and imposed as the inlet boundary condition. The rescaling operation requires the parameters u_τ and δ both at the inlet and recycling planes. These can be determined from the velocity profile at the recycling plane, but they must be specified at the inlet. The boundary layer thickness is chosen as a reference length scale and fixed at the inlet: $\delta_{inlet} = \delta_0$. For the skin friction velocity, Lund et al. [94] suggest

$$\frac{u_{\tau,inlet}}{u_{\tau,recy}} = \gamma = \left(\frac{\theta_{recy}}{\theta_{inlet}}\right)^{\frac{1}{8}}. \tag{7.2}$$

The velocity fluctuations at the inlet are related to those at the recycling plane by the following relations:

$$\left(u_i^{'}\right)_{inlet}^{inner} = \gamma \left(u_i^{'}\right)_{recy} (y^+_{inlet}, z, t), \tag{7.3a}$$

$$\left(u_i^{'}\right)_{inlet}^{outer} = \gamma \left(u_i^{'}\right)_{recy} (\eta_{inlet}, z, t). \tag{7.3b}$$

The superscripts *inner* and *outer* in (7.3) refer to the inner and outer regions of the boundary layer. In the inner region, the scaling is based on wall units y^+ whilst the outer coordinate $\eta = y/\delta$ is used in the outer region. The two scalings are blended together with a weighted average

$$(u_i)_{inlet} = \left(u_i^{'}\right)_{inlet}^{inner} [1 - W(\eta_{inlet})] + \left(u_i^{'}\right)_{inlet}^{outer} W(\eta_{inlet}). \tag{7.4}$$

The hyperbolic weighting function is defined as

$$W(\eta) = \frac{1}{2}\left\{1 + \tanh\left[\frac{\alpha(\eta - b)}{(1-2b)\eta + b}\right] / \tanh(\alpha)\right\} \tag{7.5}$$

with $\alpha = 4$ and $b = 0.2$.

Lund et al. [94] also suggest recycling the mean velocity components. Here, it was observed that excellent results can be obtained by recycling only the fluctuations and superimposing them upon the initial mean profile (7.1), provided a mass flow correction is introduced at each time step to ensure that continuity is satisfied over Ω.

Once the statistics of the precursor computation have converged, the instantaneous velocity field from a downstream plane is extracted and saved into a database over a time period T (see

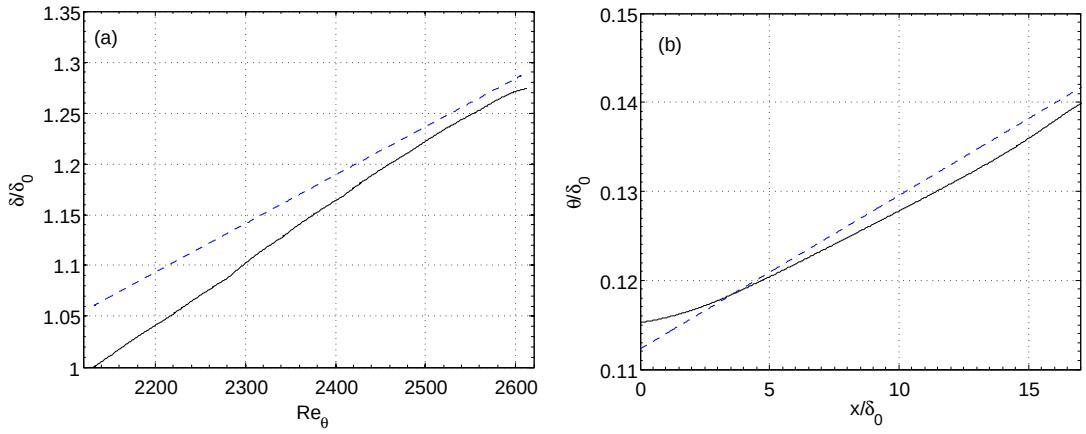


Figure 7.2: Time-averaged characteristics of inflow boundary layer from precursor simulation (solid) compared to momentum integral estimates (dashed). (a) Boundary layer thickness and (b) momentum thickness.

figure 7.1). This database is then used as the inflow of the main simulation. When the last plane of inflow data is reached, the database cycles back to its first plane, so that the main simulation can run for longer than T. Since the inflow data series is not periodic in time, this looping over the database introduces spurious oscillations into the main simulation. In the present work, the velocity database is filtered with a Tukey window to address this issue. As a result, the velocity fluctuations at the start and end of the data series are made to match. The disturbances are completely suppressed with a window altering less than 0.25% of the signal.

Figure 7.2 shows characteristics of the precursor boundary layer, compared with estimates based on the momentum integral analysis (see, e.g., White [145]). A good agreement is obtained, which confirms the success of the precursor simulation. The accuracy of the inflow treatment will be examined further in section 7.3, when looking at the flow in the inlet section of the main simulation.

7.3 Computational domain and mesh

Consider the flow in the backward-facing step domain Ω_1 that was illustrated in figure 5.1a. A 2D slice of the mesh that was used for the simulations, covering the domain Ω_1, is shown in figure 7.3. Note that only one in every four nodes is shown in each direction. In this section, we discuss the choice of the domain dimensions and the design of the computational mesh.

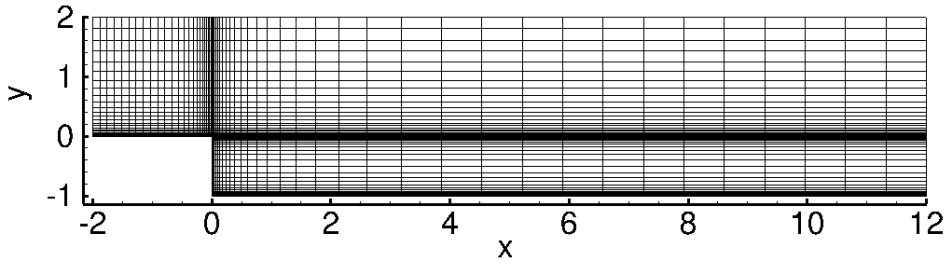


Figure 7.3: Two-dimensional slice of the nominal grid for $Re_h = 2 \cdot 10^4$, with only one in every four nodes shown in each direction.

Grid	Description	Δz^+	x_r	$(x_r - x_{r0})/x_{r0}$ (%)
Nominal	Reference	18	6.1	0
Long	$L_x = 17$	18	6.2	2
High	$L_y = 4$	18	6.35	4
Fine	Finer mesh	12	6.35	4

Table 7.1: Summary of grids tested showing the time-averaged reattachment length x_r obtained.

Both the boundary layer upstream of separation and the recirculation bubble are turbulent. In consequence, the mesh must be carefully set-up to capture the wide range of scales of motion that co-exist in the flow. These structures must either be resolved or accurately modelled by the subgrid-scale term. For this purpose, the computational cells must be small enough to capture the small structures, whilst the flow domain must be large enough to represent the largest structures.

The flow domain Ω_1 with step height h is fully determined by the four non-dimensional parameters L_i, L_x, L_y, L_z (see figure 5.1a). Table 7.1 lists four grids that are designed and tested to examine the influence of L_x and L_y, and the fineness of the mesh. All grids are structured and orthogonal.

A nominal grid is used as a reference, with dimensions $(L_i, L_x, L_y, L_z) = (2, 14, 3, 4)$. The nominal mesh is composed of approximately $6 \cdot 10^6$ computational nodes. Local refinement (or seeding) is applied near walls, in the regions near actuators and in the recirculation bubble. The wall-normal resolution of cells adjacent to walls is set to $\Delta y^+ = \Delta y \, u_\tau / \nu \approx 1$, with the wall-unit scaling based on the skin friction velocity u_τ at the inlet. The spanwise spacing is

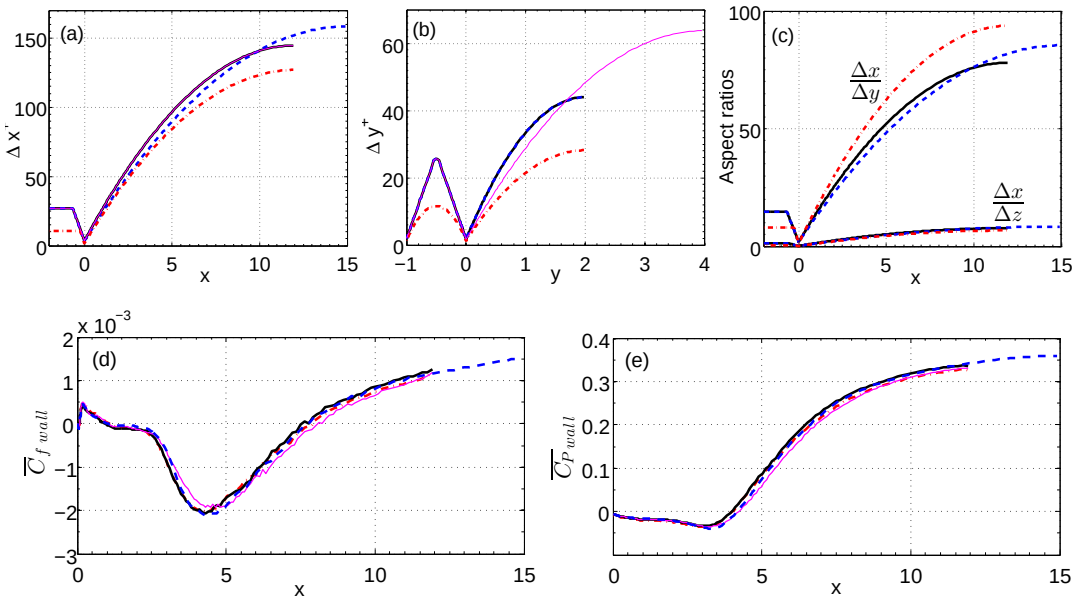


Figure 7.4: (a,b,c) Computational cell characteristics, (d) skin friction distribution and (e) pressure distribution along lower wall, for the four grids listed in table 7.1. Nominal grid ——; *Long* - - -; *High* ——; *Fine* -·-·-.

constant throughout the domain, $\Delta z^+ = 18$, whereas the streamwise spacing varies along the streamwise direction.

Three other grids are designed with parameters varying with respect to the nominal grid. The *Long* grid has $L_x = 17$, the *High* grid has $L_y = 4$, and the *Fine* grid is finer in all three directions, with a total of $28 \cdot 10^6$ cells. Table 7.1 also gives the time-averaged reattachment length x_r obtained with the four grids. The reattachment length is a key feature for numerical resolution of reattaching shear flows. All grids agree on x_r to within 4% of the nominal value x_{r0}.

The upper part of figure 7.4 plots the distribution of cell sizes in wall units along the x and y directions, as well as the cell aspect ratios, for the four grids. The maximum aspect ratio of cells is kept below 100. In addition, it is ensured that the expansion ratio between successive cells does not exceed 1.05. Note that hyperbolic tangent refining was used downstream of the step to ensure a smooth variation in cell dimensions. The distributions of skin friction and pressure coefficients along the lower wall, downstream of the step, are given in the lower part of figure 7.4 for the four grids. All the solutions are in very good agreement with the nominal grid, suggesting that the L_x and L_y dimensions are appropriate, and that the nominal grid is

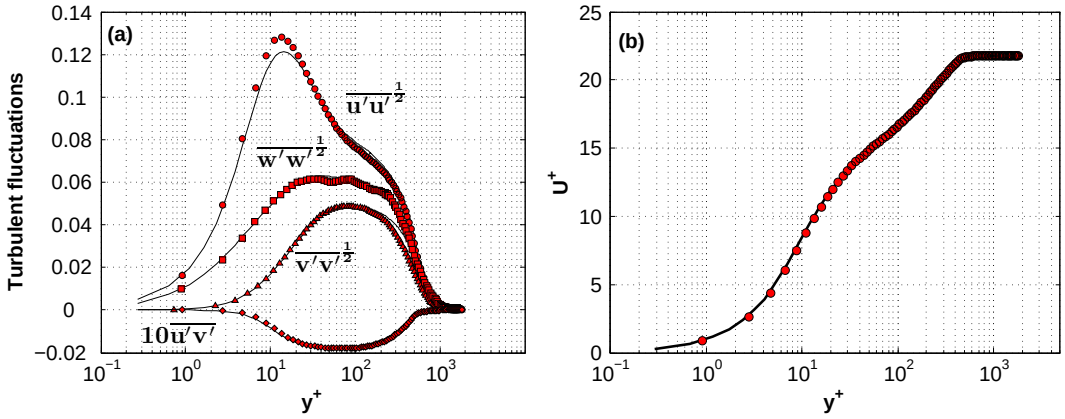


Figure 7.5: Flow characteristics at separation (x=0) compared with DNS data from Jimenez et al. [69] (solid lines) showing (a) the root-mean-square turbulent fluctuations and Reynolds stress and (b) the mean streamwise velocity profile.

sufficiently fine.

We now turn our attention to the other two dimensions defining Ω_1, L_i and L_z. Let us first consider the inlet section. Although the boundary layer flow imposed on $\partial\Omega_{in}$ is already fully developed, an inlet section remains necessary to prevent spurious oscillations [94]. To verify whether the nominal inlet length $L_i = 2$ is sufficient, we examine the flow at separation. Figure 7.5 shows the turbulent second moments and mean streamwise velocity profile at separation. The LES solution is compared with DNS data from Jimenez et al. (2010) for a turbulent boundary layer at $Re_\theta = 1551$, with zero streamwise pressure gradient. An excellent agreement is obtained, confirming that the nominal inlet length $L_i = 2$ is sufficient and that the incoming turbulent boundary layer is represented accurately.

In spanwise-homogeneous, statistically two-dimensional separated flows, structures with large scales in the spanwise direction may exist [44] and some error is induced if they are not fully contained by the computational domain. Thus we next investigate whether the spanwise extent $L_z = 4$ is sufficient. Two-point correlations can be used to evaluate the extent over which flow quantities conserve a significant correlation. The mean spanwise extent of flow structures can hence be evaluated. The correlation coefficient is given by

$$R_{\phi\psi}(\Delta z) = \frac{\overline{\phi(z)\,\psi(z+\Delta z)}}{(\overline{\phi(z)\,\phi(z)}\;\overline{\psi(z+\Delta z)\,\psi(z+\Delta z)})^{1/2}}, \tag{7.6}$$

where ϕ and ψ are two fluctuating quantities. Figure 7.6a displays the correlation coefficients R_{uu} and R_{pp} along three spanwise lines inside the shear layer, where the largest spanwise

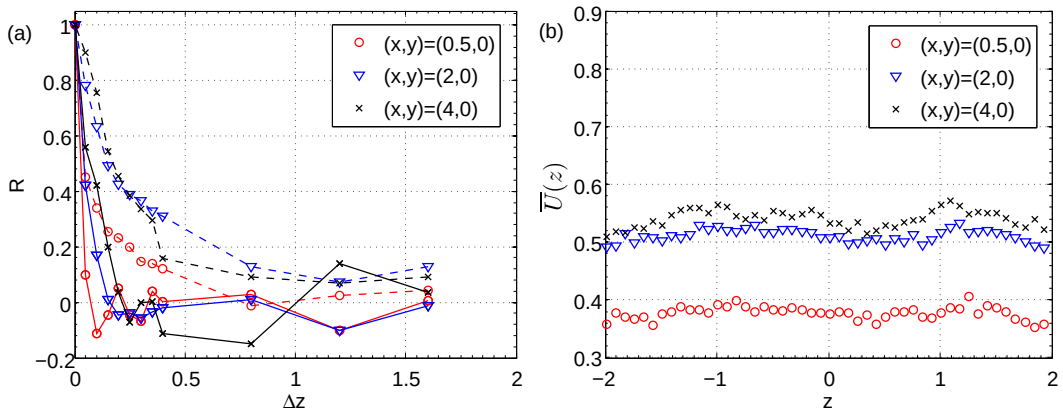


Figure 7.6: (a) Correlation coefficients R_{uu} (solid lines) and R_{pp} (dashed lines) for varying spanwise distance Δz and (b) spanwise evolution of time-averaged streamwise velocity in the shear layer.

structures are expected to be found. For both the streamwise velocity and the pressure, the correlation levels decrease rapidly and remain close to zero for $\Delta z > 0.5$. Note that the correlation does not vanish fully within a half-domain width (2h) which suggests that a larger spanwise extent may improve the accuracy of the results. Nevertheless, the spanwise extent $L_z = 4$ is deemed acceptable.

The spanwise distribution of time-averaged streamwise velocity $\overline{U}(z)$ is presented in figure 7.6b at three locations inside the separated shear layer. Despite some small variations in z due to a lack of perfect convergence of the statistics in time –this is caused mainly by the very low frequency motions that can arise in reattaching shear layers– the time-averaged flow can be considered to be independent of the spanwise direction z. Henceforth averaging in span will be used to improve the convergence of the time statistics, hence the notation $\overline{(\cdot)}$ will denote an average in time and in z, unless otherwise stated. To conclude, this investigation satisfies us that the nominal grid can be used to represent the turbulent backward-facing step flow accurately.

7.4 Baseline flow

We now proceed to investigate the main features of the uncontrolled flow. We first look at large-scale features of the time-averaged flow, including characteristics of the recirculation bubble and the mixing layer. Then we proceed to examine the dynamics via spectral analysis.

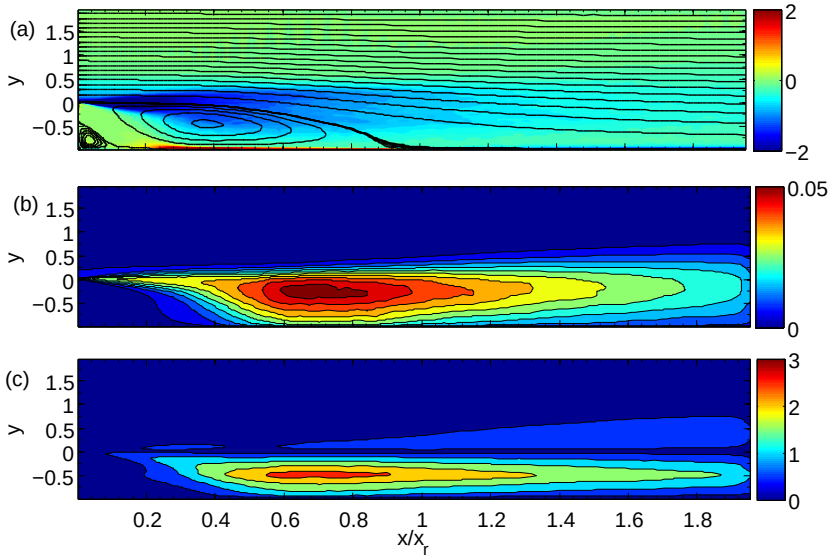


Figure 7.7: Time-averaged contours of flow and LES model properties. (a) Line contours of time-averaged streamfunction on colour contours of vorticity $\overline{\omega}_z$; (b) contours of turbulent kinetic energy $k = 0.5(\overline{u^2} + \overline{v^2} + \overline{w^2})$ and of (c) the eddy viscosity ratio $\overline{\nu_t}/\nu$.

7.4.1 Main time-averaged features

Three contour fields covering the domain downstream of separation are illustrated in figure 7.7. Recall that the step corner is at (0,0,z). Figure 7.7a shows line contours of time-averaged streamfunction on time-averaged vorticity $\overline{\omega_z}$ colour contours. The main features of the flow appear similar to what was observed in the 2D laminar flow. The main and secondary recirculation bubbles are evidenced by the streamfunction contours. Note that the secondary bubble is significantly smaller in the turbulent case. The vorticity highlights the spreading of the shear layer via a growing region of negative vorticity. Interestingly, a thin and elongated region of intense positive vorticity embraces the lower wall in the region $0.2 \leq x/x_r \leq 1$.

The field of turbulent kinetic energy $k = 0.5(\overline{u^2} + \overline{v^2} + \overline{w^2})$ is represented in figure 7.7b. The maximum k is located in the shear layer in the region $0.6 \leq x/x_r \leq 0.8$. The presence of the wall and a large stabilizing curvature of the shear layer near reattachment result in a sharp decrease of the turbulent kinetic energy.

Finally, figure 7.7c plots the averaged eddy viscosity ratio $\overline{\nu_t}/\nu$. This ratio provides a measure of the reliance on the subgrid-scale model to solve the LES equations. High values of $\overline{\nu_t}$ imply that the model plays an important part in the solution. Hence it is necessary to ensure that $\overline{\nu_t}/\nu$ is small. Here, the ratio does not exceed 2.5, which is deemed acceptable. As

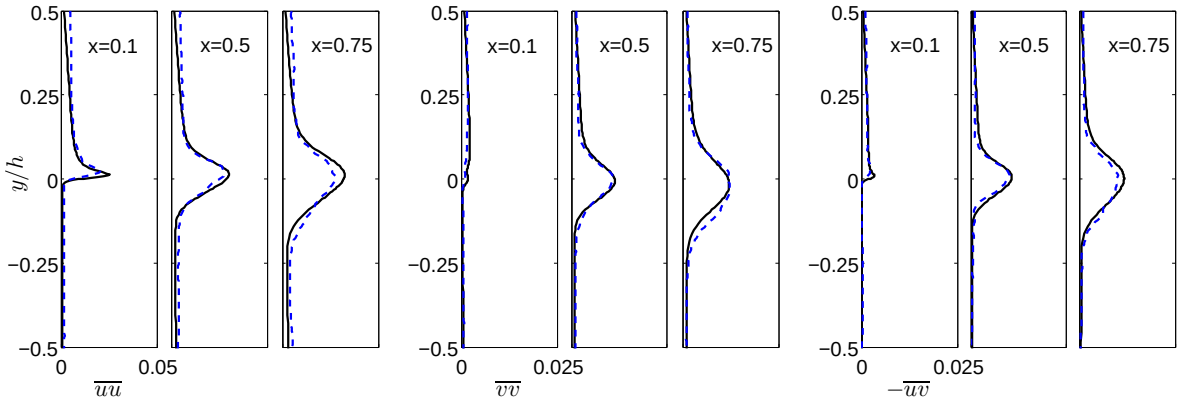


Figure 7.8: Second turbulent moments (streamwise, transverse and Reynolds stresses) in the near-base flow, comparing LES data (solid lines) with PIV data from Brosco [12].

expected, the subgrid-scale model is most active in regions of high turbulent kinetic energy.

Figure 7.8 compares second moments of velocity fluctuations with experimental data on a backward-facing step obtained by Brosco [12] with particle image velocimetry (PIV). The conditions of the experiment of Brosco are not exactly identical to the present boundary conditions, but are sufficiently close for a meaningful comparison. The experimental Reynolds number is $Re_\theta = 1381$ and the expansion ratio is 1.02. A good agreement between the LES and the PIV is evident, indicating that the recirculation bubble and initial stages of the shear layer are well represented by the LES.

The separated shear layer can be analyzed like a traditional mixing layer. For instance, the streamwise evolution can be examined by computing the evolution of the momentum and vorticity thicknesses (see figure 7.9). Because of the strong backflow below the mixing layer, the definitions for these thicknesses are not evident. Here the backflow is taken into account in the definition of the two thicknesses, following Dandois et al. [29].

The momentum thickness is defined as

$$\theta(x) = \int_{y_{min}}^{\infty} \frac{\overline{U}(x,y) - \overline{U}_{min}(x)}{U_0 - \overline{U}_{min}(x)} \left(1 - \frac{\overline{U}(x,y) - \overline{U}_{min}(x)}{U_0 - \overline{U}_{min}(x)}\right), \tag{7.7}$$

where $\overline{U}(x,y)$ is the streamwise velocity averaged in time and along the spanwise direction, and $\overline{U}_{min} = \min_y(\overline{U}(x,y))$. In their experimental investigation on free mixing layers, Browand & Troutt [14] found that the growth rate of the momentum thickness is well fitted by the linear

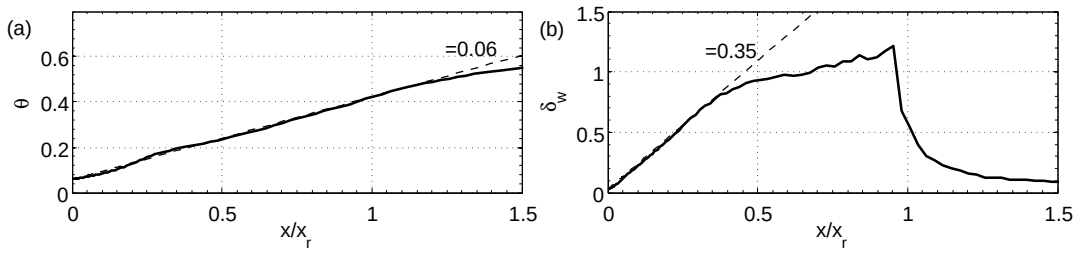


Figure 7.9: (a) Momentum thickness and (b) vorticity thickness evolution along the mixing layer.

relation

$$\frac{d\theta}{dx} = 0.034\lambda, \tag{7.8}$$

where $\lambda = (U_0 - \overline{U}_{min})/(U_0 + \overline{U}_{min})$ is the velocity ratio. In our case λ varies between 1 and 1.6, so that the expected growth rate is $0.034 \leq d\theta/dx \leq 0.054$. As evidenced by figure 7.9a, a good fit is obtained with $d\theta/dx = 0.06$ which is higher than the prediction of (7.8). This is due to the large negative velocities below the mixing layer and extra entrainment from the low pressure recirculation region that encourages the growth of the mixing layer.

The vorticity thickness is given by

$$\delta_\omega(x) = \frac{U_\infty - \overline{U}_{min}(x)}{\max_y \left(\frac{\partial \overline{U}(x,y)}{\partial y}\right)}. \tag{7.9}$$

The initial growth rate of δ_ω is shown in figure 7.9b to be close to 0.35 up to $x/x_r = 0.4$. After this point, the presence of the wall starts to be felt which causes the growth to slow down. Browand & Troutt [14] also obtained an empirical relation for the growth of the vorticity thickness in free mixing layers:

$$\frac{d\delta_\omega}{dx} = 0.17\lambda. \tag{7.10}$$

This corresponds to values of the growth rate between 0.17 and 0.27. Again, $d\delta_\omega/dx$ observed in this case is higher because the shear layer separating from the backward-facing step is not truly a free mixing layer.

7.4.2 Spectral analysis

The recirculation bubble is the witness of large-scale modes of motion —the shear layer, shedding and flapping modes— and small-scale turbulent fluctuations, all interacting with each

other in complex ways. These interactions give rise to rich dynamics throughout the bubble. We examine these dynamics via spectral analysis, using Fourier decomposition of pressure time series. The Fast Fourier Transform (FFT) algorithm (performing a discrete Fourier transform) in MATLAB is used for this purpose. Time series are recorded at several probe locations from the LES simulations. All probes record a signal over a period T=1200 time units, containing roughly 1.5 million samples. The time step between consecutive samples is variable, due to the dynamic time-stepping in the LES. Constant time-step signals are constructed by linear interpolation of the raw signals and the sampling time is set to $T_s = 5 \cdot 10^{-3}$. We verified that the interpolation does not affect the spectra by comparing the results obtained with cubic interpolation and with varying values of T_s. The signals are broken down into blocks of 16384 samples, with an overlap of 50%, giving a frequency resolution of $\Delta St_h = 1.2 \cdot 10^{-2}$. The discrete Fourier transforms of the 28 blocks are computed and averaged to reduce the impact of noise. The blocks are pre-multiplied with Hanning functions to avoid spectral leakage.

Figure 7.10 shows pressure spectra at various locations downstream of separation, inside the recirculation bubble. The value labels on the y-axis are omitted because they are not relevant to our discussion; it suffices to note that both axes are logarithmic and are the same for all the plots of figure 7.10. At the first position, x=1, a peak is observed at $St_h \approx 0.32$, or $St_\theta \approx 0.024$. This peak is detected throughout the height of the bubble at this station (for all values of y). It corresponds to the convective Kelvin-Helmholtz instability which originates in the shear layer, soon after separation. The first sub-harmonic at $St_h \approx 0.16$ is also visible, although weaker.

There is a hump in the spectra, spread over a large band of frequencies. This signals the broadband character of the reattaching shear layer and the bubble, due to the interaction between the three dominant modes. Driver et al. [35] performed a spectral analysis of the bubble behind a backward-facing step and divided the spectrum into three parts: the flapping, the vortical structures and the turbulent fluctuations. The flapping motion appears at low frequencies, below the main hump, and is difficult to detect since it has low energy. The vortical structures existing in the shear layer and the bubble cause the main hump, beyond which the fluctuating energy is associated with small-scale turbulent eddies. Near separation, most of the fluctuating energy is concentrated in the shear layer, close to $y = 0$. As the shear layer grows, the fluctuating power spreads towards the lower wall.

The spectrum of the sensor signal that will be used for control is shown in figure 7.10h. This

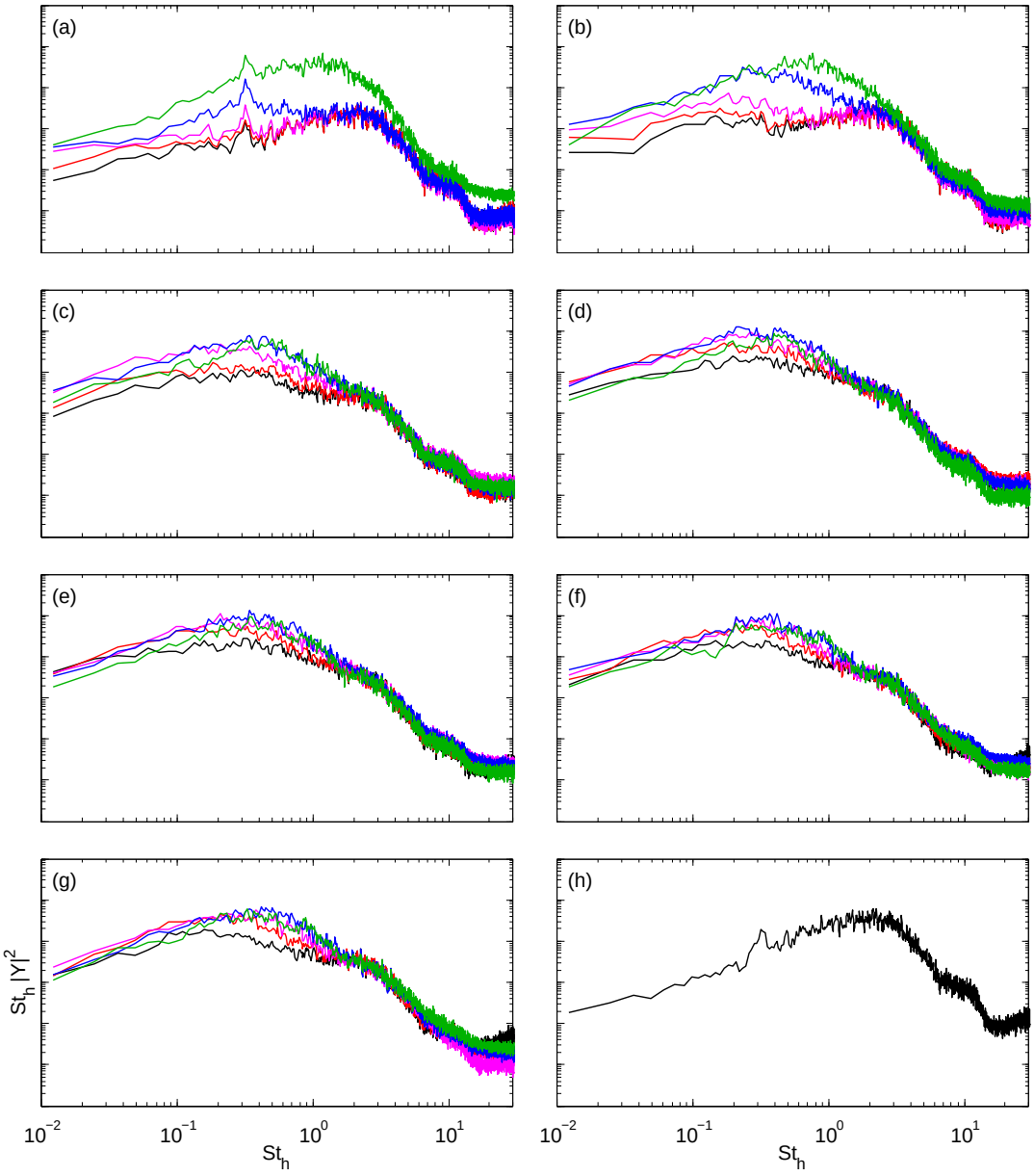


Figure 7.10: Pressure spectra downstream of separation, along z=0. (a) x=1, (b) x=2, (c) x=3, (d) x=4, (e) x=5, (f) x=6, (g) x=7 and (h) sensor signal (base pressure fluctuations). y=0; y=-0.25; y=-0.5; y=-0.75; y=-1 (lower wall).

is the spectra of the pressure spatially-averaged over the base. The main features described above, such as the shear-layer instability and the large hump are observable from the base. Thus, the dynamics that must be influenced in order to affect the wake are observable with the current sensing arrangement. Note the non-physical behaviour at the high-frequency end of the spectra. This is due to high-frequency residual noise in the pressure field associated with the numerical scheme. This weak noise is not present in the velocity field. Although this disturbance could be reduced by lowering the residual tolerance of the multigrid pressure solver, it does not affect the accuracy of the results because it only manifests itself beyond the dissipation range.

7.5 Open-loop forcing

After investigating the baseline flow, the purpose of this section is two-fold. Firstly, the effects of the open-loop harmonic forcing (with both actuator locations) on the flow are described. Secondly, the results of the system identification procedure carried out in a similar manner to chapter 6 are discussed. The same two actuator configurations considered in the 2D case (see chapter 6) are used here.

7.5.1 Physical insight

Harmonic perturbations introduced in the flow lead to harmonic fluctuations observable by the sensor measurement, but they also lead to changes in the time-averaged dynamics via non-linear effects. Figure 7.11 illustrates the effect of the slot jet forcing frequency on two time-averaged quantities: the reattachment length x_r and the (spatially-averaged) base pressure $\overline{C_P}$. The most evident feature is the radically different response of the wake to the two actuator locations. Actuator 1, located near the separation edge in a region of high receptivity, has a strong impact on both x_r and $\overline{C_P}$. On the contrary, actuator 2, perturbing the flow near the base foot, has virtually no impact on the reattachment length. It leads to a reduction in $\overline{C_P}$ with a narrow valley at $St_h \approx 0.25$ and a roughly constant pressure decrease (which strengthens with the amplitude of the perturbation) away from this frequency.

For actuator 1, figure 7.11a shows that forcing decreases x_r by up to 35% at low forcing frequencies and increases it slightly for frequencies in the range $0.8 \leq St_h \leq 2$. A comparison with experimental data at $Re_\theta = 890$ from Chun & Sung [21] is included. Although the flow

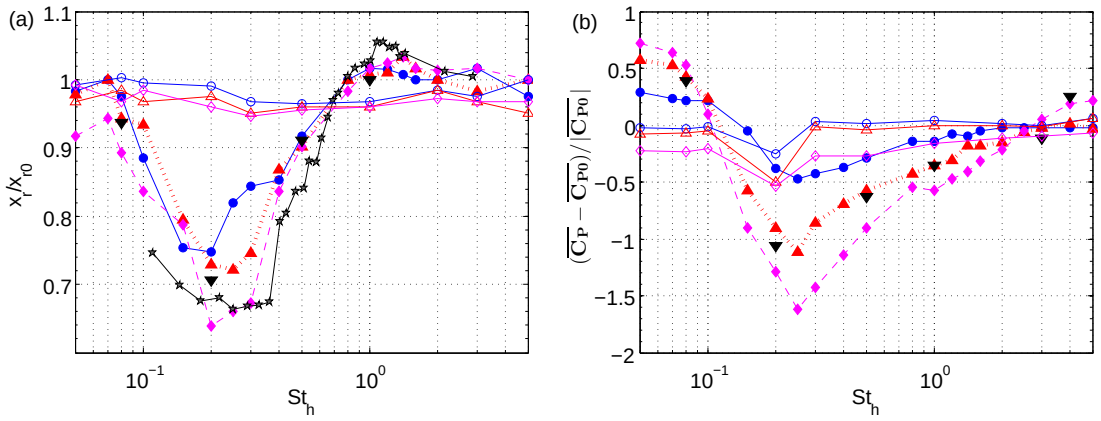


Figure 7.11: Effect of open-loop forcing on time-averaged (a) reattachment length x_r and (b) base-pressure $\overline{C_P}$. The zero subscript denotes the baseline case. Experimental data from Chun & Sung [21] ($Re_\theta = 890$, forcing level $A_0 = 0.07$) is included for comparison (★). Three forcing amplitudes are considered: $A_j = 0.1$ (●), $A_j = 0.2$ (▲) and $A_j = 0.3$ (♦). Results obtained at a few frequencies with actuator 1 ($A_j = 0.2$) on the *Fine* grid are denoted by ▼. Actuator 1 is represented by filled symbols and actuator 2 by open symbols.

conditions and actuation level differ (the latter can not be directly compared due to different slot widths and definitions of the forcing amplitude), the curve for forcing level $A_j = 0.3$ agrees reasonably well with the experimental data. Yoshioka et al. [147] report a maximum reduction in reattachment length of 30% for a forcing amplitude $A_j = 0.3$ which provides further support for the present results. The reduction of the reattachment length is linked to increased turbulent stresses near separation which lead to a higher growth rate of the shear layer. The shear near the interface of the layer and the recirculating flow is also higher hence producing higher entrainment and earlier reattachment.

We now turn our attention to the effect of actuator 1 on the time-averaged base pressure $\overline{C_P}$. Figure 7.11b shows that frequencies below $St_h \approx 0.1$ lead to an increase in $\overline{C_P}$ whereas a pressure decrease is observed for $St_h > 0.1$. The change in $\overline{C_P}$ is nearly a linear function of forcing amplitude within the frequency range $0.1 < St_h < 2$ for the three amplitudes tested, although the relation becomes non-linear if higher forcing amplitudes are used.

For both the reattachment length and the base pressure coefficient, results obtained with the *Fine* grid at a few selected forcing frequencies match well with the solutions on the nominal grid, thereby indicating that the latter grid is adequate to compute the perturbed flows. However, a

significant discrepancy is observed in the time-averaged base pressure obtained for $St_h = 4$, as evidenced by figure 7.11b. The nominal grid predicts that $\overline{C_P}$ is not affected by the harmonic perturbations with $A_j = 0.2$ for $St_h > 3$ whilst the *Fine* grid shows a pressure increase of almost 30% for $St_h = 4$. This happens because the nominal grid struggles to resolve the very small scale structures produced by high-frequency perturbations (an order of magnitude above the dominant unstable modes of the flow). Some recent studies have pointed out that actuation via these small-scale perturbations provides a promising open-loop control mechanism (see, e.g., Vukasinovic et al. [141]) and in particular a means to reduce form-drag on an axisymmetric bullet-shaped body [110].

For all three forcing amplitudes, global minima are obtained for both x_r and $\overline{C_P}$ around the same frequency $St_h \approx 0.25$. A number of studies on reattaching shear layers have proposed that the frequency for maximum reduction of x_r is associated with the shedding mode [29]. In other words, the frequency for maximum reduction of x_r and $\overline{C_P}$ is dictated by the rate of vortex shedding from the reattachment region. As shown in figure 7.11a, Chun & Sung [21] obtained a global minimum at $St_h \approx 0.27$, and they associated this extremum with the shedding mode. Also, they observed the existence of a local minimum at $St_h = 0.4$ for lower forcing amplitudes, which they identify as the shear layer instability. A pronounced dip is visible in figure 7.11a at $St_h = 0.4$ for the lowest amplitude $A_j = 0.1$. This supports the hypothesis that the forcing frequency $St_h \approx 0.25$ corresponding to the trough in the x_r and $\overline{C_P}$ *bucket* is in fact linked to the shedding mode.

Figure 7.12 illustrates base pressure spectra for the flows perturbed with two open-loop harmonic signals $U_j = 0.2\sin(2\pi 0.08t)$ and $U_j = 0.2\sin(2\pi 0.2t)$. We will henceforth term those two signals the low-frequency (LF) and the medium-frequency (MF) forcing. Both actuators are considered and compared to the baseline case. Comparison of the two actuators leads to an observation already mentioned: open-loop forcing with actuator 1 has a stronger impact on the flow. Large peaks associated with the forcing are visible for actuator 2 for both the LF and MF perturbations. These peaks, however, are smaller than those produced by actuator 1 and other wavelengths are not sensibly disturbed compared to the baseline flow. Actuator 1 amplifies the level of pressure fluctuations on the base over a broad range of scales around the forcing. In addition, it can be observed that the MF forcing with actuator 1 tends to suppress the shear layer instability.

Figure 7.13 shows some features of the flow perturbed with the LF and MF signals. Again it

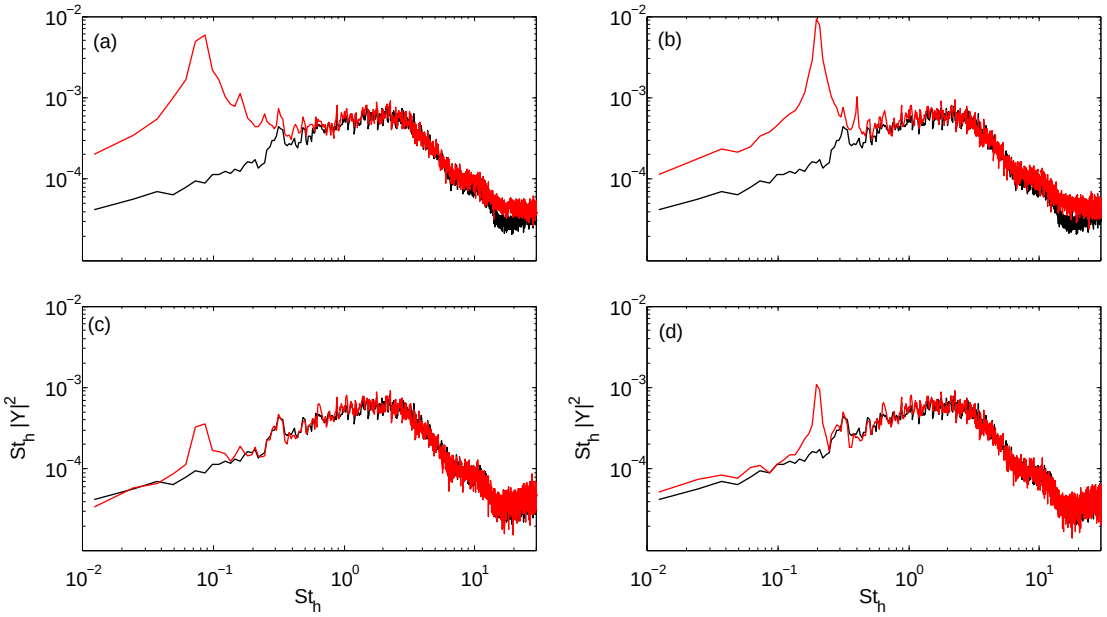


Figure 7.12: Spectra of sensor signal (base pressure fluctuations) for harmonic forcing with (a,b) first control location and (c,d) second control location. Harmonic forcing with amplitude $A_j = 0.2$ and frequencies (a,c) $St_h = 0.08$ and (b,d) $St_h = 0.2$. ——— Baseline; ——— Control.

is obvious that the second actuator has a lesser impact on statistical flow features compared to the first one. However, careful observation of profiles of $\overline{U}$ and $\overline{V}$ in figure 7.13 reveals that the mean flow velocity profiles in the near-separation region are altered by actuator 2. Considering actuator 1, it was previously observed that the LF forcing increases the mean base pressure $\overline{C_P}$, whilst the MF forcing reduces it. As evidenced by figures 7.13a and 7.13c, the mean velocity profiles are only weakly affected by the LF forcing. On the other hand, the MF forcing reduces the reattachment length more significantly and hence affects the velocity field. The turbulent kinetic energy profiles shown in figure 7.13e reveal an interesting perspective: the LF forcing dramatically changes the profile of turbulent fluctuations downstream of reattachment, where the influence of the MF forcing is comparatively small. The turbulent kinetic energy is pulled towards the lower wall by the LF forcing. As is well known, the forcing at $St_h = 0.2$ increases the peak turbulent fluctuations in the separated region, with a maximum reached around $x/h = 2$.

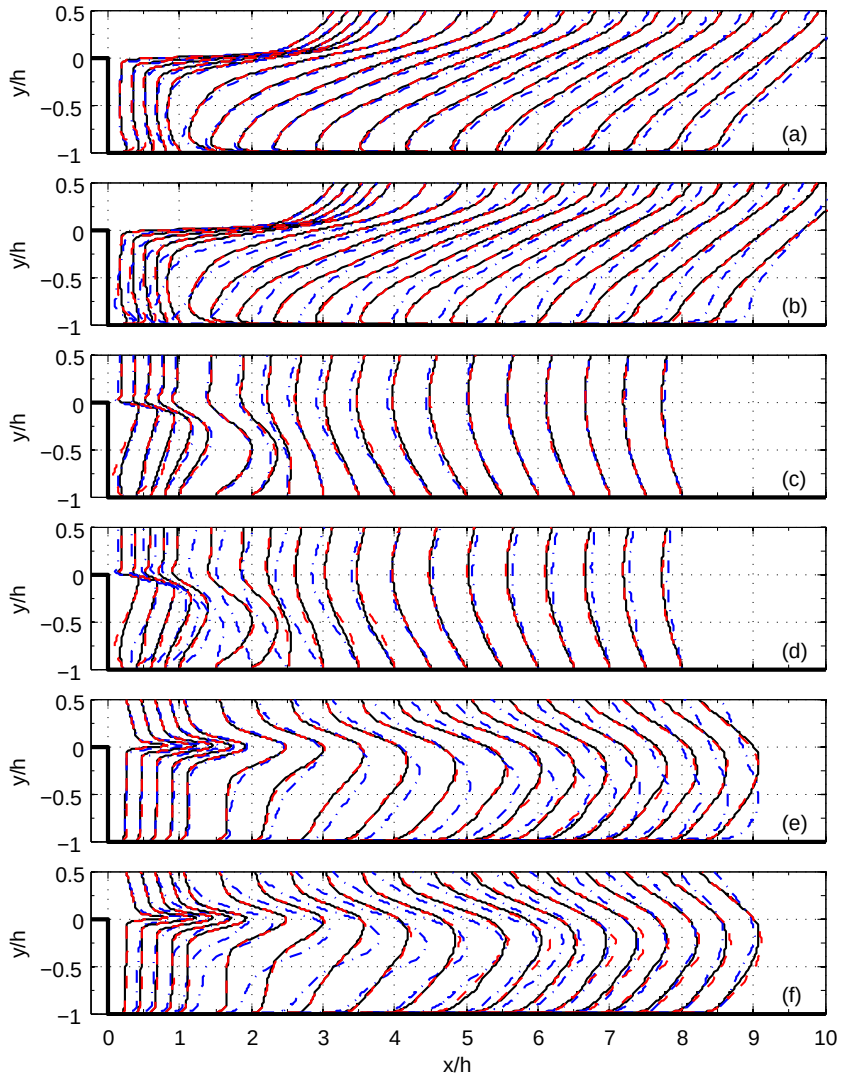


Figure 7.13: Flow characteristics downstream of separation for forcing with (a,c,e) $St_h = 0.08$ and (b,d,f) $St_h = 0.2$. (a,b) Time-averaged streamwise velocity $\overline{U}$, (c,d) transverse velocity $\overline{V}$ and (e,f) turbulent kinetic energy k. ——— Baseline flow; -·-·- actuator 1; ····· actuator 2.

7.5.2 System identification

As for the 2D flow, the information obtained from the harmonic open-loop forcing also serves to identify the flow response $G(i\omega)$; i.e. the response of the base pressure fluctuations to the actuation. The validity of the dynamic linearity assumption is checked by examining different forcing amplitudes. Figure 7.14 shows Bode plots of the frequency responses G_1, G_2 and G_3 obtained with harmonic forcing at three different amplitudes $A_j = 0.1$, 0.2 and 0.3, with each actuator independently. For both actuators, the slight mismatch between the three curves reveals that weak non-linearities are present in both gain and phase. However, the deviations between the three curves do not exceed 2dB and 7.8° for actuator 1 and 4.3dB and 12.5° for actuator 2. Hence, approximating the flow response as a dynamically linear process is a reasonable approximation here, as long as the magnitude of the actuator signal remains within the range considered.

For each actuator, a frequency response model G is constructed as the average of G_1, G_2 and G_3, illustrated by the square dots in the lower part of figure 7.14. The solid line represents a model fitted to the data via the MATLAB command fitfrd, performing least-squares minimization in the frequency domain. The models fitted for actuators 1 and 2 are given by (7.11) and (7.12) respectively.

$$G_{actu1}(s) = \frac{-1440s - 9312}{s^2 + 11740s + 28560} \tag{7.11}$$

$$G_{actu2}(s) = \frac{62.88s^2 + 1404s + 98.85}{s^2 + 1148s + 26427} \tag{7.12}$$

Both fitted transfer functions G_{actu1} and G_{actu2} are stable and minimum phase. The dashed lines in the lower part of figure 7.14 represent models obtained by performing the Eigensystem Realization Algorithm (ERA) on input-output data from the LES. Rather than applying harmonic inputs of different frequencies, a single input containing the entire band of interest is chosen for identification via the ERA. The input selected for the ERA is a sum-of-sines signal of the form:

$$U_j(t) = A_j \sum_{k=1}^{K} \sin(\omega_k t + 2\pi\phi_k). \tag{7.13}$$

The lower and upper limits of the passband are $\omega_{min} = 0.3$ and $\omega_{max} = 31$, $K = 24$ is the number of sinusoids spread evenly within the passband, and $\omega_k = \omega_{min} + (k-1)(\omega_{max} - \omega_{min})/(K-1), k = 1, ..., K$. To ensure a sensible time variation of the signal amplitude, the

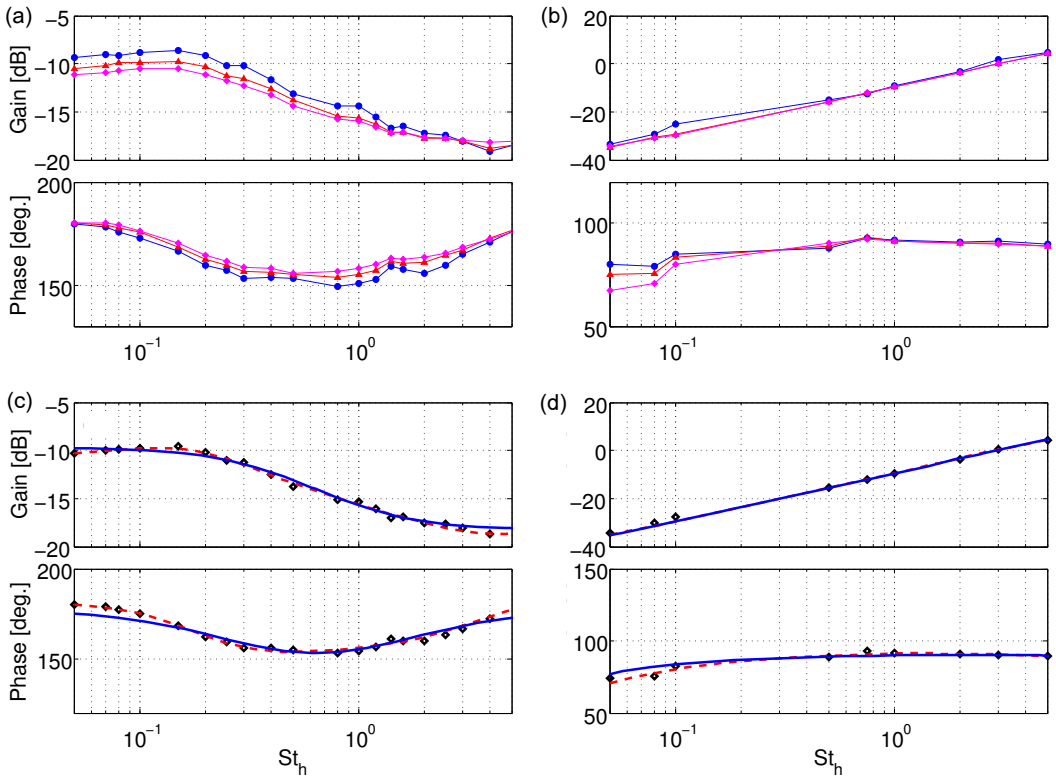


Figure 7.14: Bode plots of frequency responses for (a,c) actuator 1 and (b,d) actuator 2. (a,b) Frequency responses for different forcing amplitudes: (●) $A_j = 0.1$, (▲) $A_j = 0.2$ and (♦) $A_j = 0.3$. (c,d) Frequency responses averaged over three amplitudes (◇); ——— least-squares fits; ------- low-order models obtained with the ERA.

phase of the k^{th} sinusoid at $t = 0$ is $2\pi\phi_k$, where ϕ_k is a random number taken from a uniform distribution on the interval [0,1].

The ERA is a system identification and model reduction technique proposed by Juang & Pappa [71] which generates reduced order models theoretically identical to those obtained from balanced Proper Orthogonal Decomposition (POD) [95]. The balancing refers to the observability and controllability gramians of the reduced model being equal and diagonal (balanced), which ensures that the dynamics of the system are properly accounted for (by selecting the modes which are both observable and controllable when reducing the system). An important feature of the ERA is that it does not require the solution of an adjoint system and hence is suitable for use with both computational and experimental data. For more details on the notions of observability and controllability and on the ERA, the reader is referred to Illingworth [66]. Figure 7.14 demonstrates a remarkable agreement in the transfer functions obtained by spectral analysis with harmonic forcing and those obtained with the ERA using a more sophisticated input signal. We conclude that both methods are suitable. The ERA is less computationally expensive but care must be taken to design an input signal with smooth time variations so as to avoid numerical instabilities.

Although the dynamics of G here are different than in the 2D laminar case, some similarities are evident from comparison of figures 6.10 and 7.14. In particular, actuator 2 exhibits a gain increasing monotonically with frequency, within the frequency band examined, and a constant phase lag at high frequencies. On the other hand, the transfer function from the first actuator to the base pressure is highly sensitive to the shear layer development and hence has different dynamics in the laminar and turbulent flows. Indeed, the low-frequency gain is higher and there is no high-frequency roll-off in 3D.

It is important to keep in mind some of the limitations of the low-order models built herein; in particular that they apply only specifically to the actuation-sensing couple selected. As observed above, if the actuator is displaced to a different location, its impact on the wake is altered and different dynamics arise.

7.6 Closed-loop control

7.6.1 Control synthesis

After obtaining a low-order model for $G(s)$, a controller $K(s)$ can be designed using the fluctuations attenuation approach described in chapter 6. As explained in §5.3, the controller aims to reduce the fluctuations in the sensor signal, by constraining the sensitivity function to have a gain below unity within a specific frequency range.

Achieving this over a large frequency band is not always possible. Bode's integral formula (7.14) relates the integral of the sensitivity gain over all frequencies to the unstable open-loop poles p_k. This means that if the sensitivity gain is reduced in a particular frequency range, it will increase in another:

$$\int_0^\infty \ln|S(i\omega)|\,d\omega = \pi \sum Re(p_k) - \frac{\pi}{2} \lim_{s\to\infty} sL(s). \tag{7.14}$$

Whilst this was of little concern in the 2D case, where the baseline flow is dominated by a single frequency, the 3D turbulent flow requires the shaping of $|S(i\omega)|$ over a large range of scales. Therefore, the H_∞ loop-shaping method [97] is chosen here. The loop-shaping technique, used for the 2D laminar flow, is a well-known approach in control theory, whereby one specifies closed-loop objectives in terms of requirements on the open-loop transfer function $L = GK$ (or its singular values in the case of multi-input multi-output systems). This approach however suffers from the need to ensure stability of the closed-loop system. Another approach to controller design is H_∞ synthesis in which the closed-loop objectives are expressed in terms of weighted closed-loop transfer functions. H_∞ synthesis guarantees stability and robustness although the selection of the closed-loop weights is not straightforward and may be disconnected from the properties of the controlled process.

H_∞ loop-shaping combines the advantages of these two methods. The open-loop properties of L are specified first by adding a pre- and post-compensator to the open-loop process G (for SISO systems these collapse to a single compensator) and the H_∞ method is then used to robustly stabilize this shaped plant. Hence, this method returns a robust controller $K(s)$ to satisfy a desired open-loop transfer function $L(s) = G(s)K(s)$ whilst the closed-loop system is guaranteed to be stable. The compensator was selected by inspection, to give a desired open-loop shape $L_d(s)$, given the plant transfer function $G(s)$, whilst $L_d(s)$ was obtained by loop-shaping in order to yield a required sensitivity gain distribution. The loopsyn function in

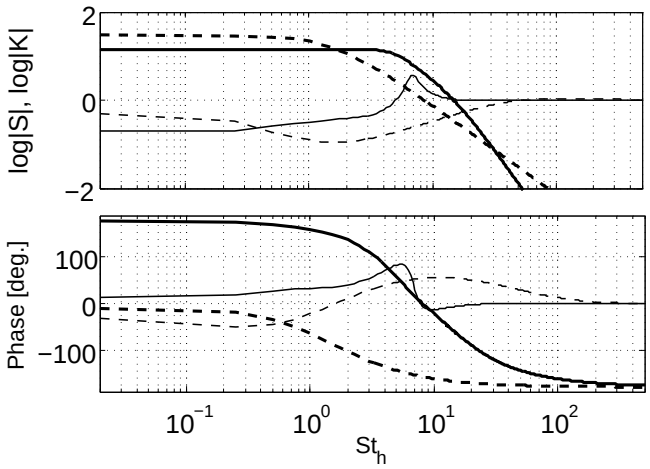


Figure 7.15: Characteristics of closed-loop systems for both actuator locations. Solid and dashed lines refer to the first and second actuators respectively. The gain and phase of the controllers K are shown as thick lines whilst thin lines represent the sensitivity functions.

MATLAB was used to perform the H_∞ loop-shaping synthesis.

The characteristics of the resulting controllers for both actuator locations are given in (7.15) and (7.16).

$$K_1(s) = \frac{-1.26 \times 10^8}{s^4 + 196s^3 + 16660s^2 + 504000s + 9 \times 10^6} \tag{7.15}$$

$$K_2(s) = \frac{3000}{s^2 + 20s + 100} \tag{7.16}$$

For actuator 1, the gain and phase margins of the control system are 1.6 and 26° respectively, and the maximum sensitivity gain is quite high, $M_s = max_\omega |S(i\omega)| = 2.99$, although it occurs in a range of frequencies where flow disturbances are small. The control system with actuator 2 has an infinite gain margin and a phase margin of 89°, with $M_s = 0.9$. Figure 7.15 shows the frequency responses of the controllers and the corresponding sensitivity functions $S(i\omega)$ obtained from the loop-shaping control synthesis. The main features to note are that the first actuator location has lower stability margins, as well as a small positive hump in the sensitivity gain centered around $St_h = 7$ which implies that noise is amplified near this frequency.

Figure 7.16 illustrates the results obtained from implementing the feedback controller K_1 into the LES. The left-hand plots of the figure represent time-domain data whereas the right-hand plots show the corresponding spectra. Both views appear simultaneously in order to convey a clear sight of the control effect on the input and output signals. The pressure fluctuations are reduced in amplitude and the actuation levels required are relatively low. The

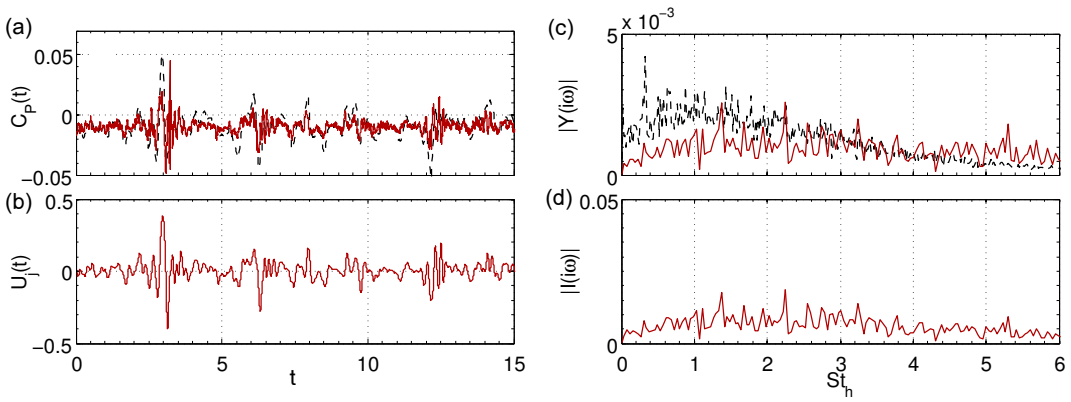


Figure 7.16: Input and output for controller K_1, with the first actuator location. Time-series of (a) the sensor (base pressure) signal and (b) the actuation signal. Amplitude spectrum of (c) the sensor signal and (d) the actuation signal. Baseline, ---- ; control, ——— .

amplitude spectrum of the sensor signal highlights an attenuation of the fluctuations over a large bandwidth, although high frequencies are amplified. The mean base pressure is also increased by 20% compared to the baseline flow.

The control results for the controller K_2, operating via the second actuator location, are shown in figure 7.17. In this case, the attenuation of the pressure fluctuations and the high-frequency rejection are more effective than with K_1. However, very low frequencies are amplified. The actuation signal U_j output by the controller K_2 operates at low frequencies, in contrast to the previous controller. A mean base pressure increase of 10% is recorded with K_2, which is less than with K_1. This suggests that the link between the base pressure fluctuations and the time-averaged value is complex and further investigation into this relationship would need to be performed in order to exploit it for optimization.

7.6.2 Flow mechanisms

Let us investigate the controlled flow fields with a view to obtaining some insight into what the control achieves. Note that a more detailed investigation into the flow mechanisms will be performed in chapter 8. Figure 7.18 shows some characteristics of the controlled flows downstream of separation compared to the baseline flow. The controllers K_1 and K_2 only mildly affect the time-averaged velocity fields $\overline{U}$ and $\overline{V}$, although the peak $\overline{V}$ in the region $1 \leq x \leq 2$ is significantly reduced. As mentioned before, this peak is the time-averaged trace of the passage of large-scale vortices. The turbulent kinetic energy is significantly reduced over

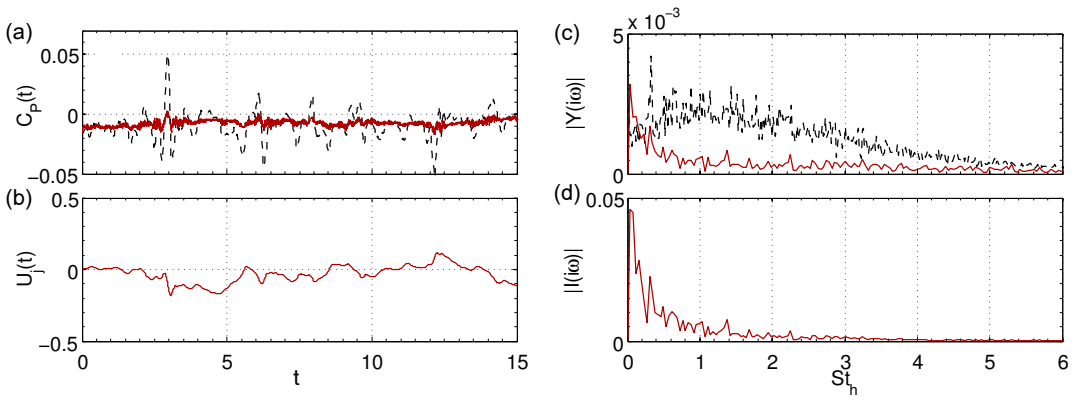


Figure 7.17: Input and output for controller K_2, with the second actuator location. See caption of figure 7.16.

a large region of the domain. Actuator 2 leads to a more important reduction of the turbulent kinetic energy in the separated shear layer. Note that, overall, both controllers impose very similar effects on the mean flow despite their control action being effected from very different locations.

Line contours of the time-averaged streamfunction for the baseline and controlled flows are plotted in figure 7.19. As discussed above, the time-averaged streamwise velocity field is globally only weakly modified by the feedback controllers for both actuator locations. The reattachment lengths of the controlled flows are mildly increased compared to the baseline flow. For actuator 1, $x_r = 6.8$ while for actuator 2, $x_r = 6.9$, compared to $x_r = 6.2$ in the baseline case. This represents an increase of roughly 10% in x_r for the controlled flows.

It appears therefore that the recirculation length is not a useful indicator for the base pressure force. In the laminar case it was shown that the base pressure force can be increased via control leading to a stabilized near-wake and delayed reattachment. For the turbulent flow, open-loop forcing frequencies below $St_h = 0.1$ lead to a decrease in x_r and an increase in $\overline{C_P}$ on the base whereas the present feedback control strategy leads to a mild increase in x_r and an increase in $\overline{C_P}$.

Figure 7.19 also shows a magnified view of the secondary recirculation eddy sitting near the base foot. Both controllers reduce the size of this structure. This secondary recirculation bubble is the time-averaged view of bursts of high momentum fluid, brought in from the reattachment region, impinging onto the base. It has been associated with the flapping mode [129], forming a feedback mechanism between the reattachment zone and the near-separation region.

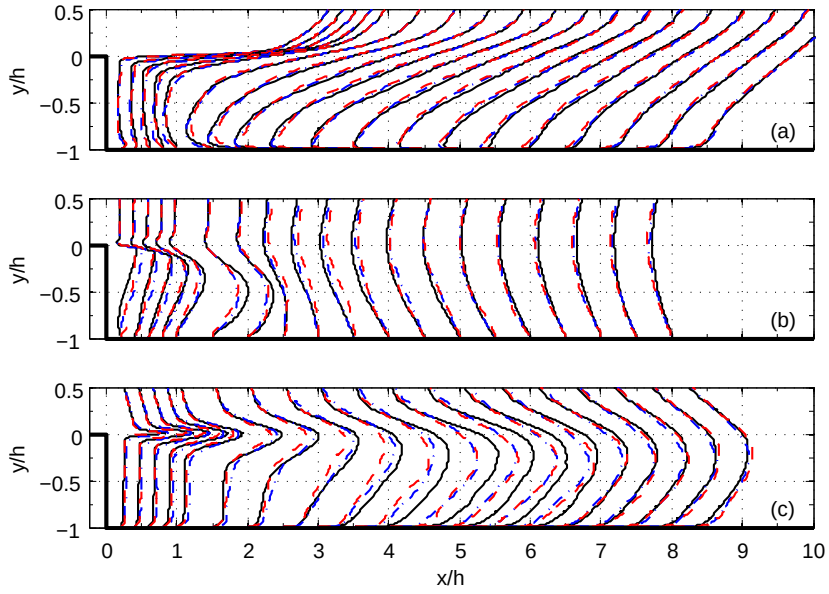


Figure 7.18: Time-averaged flow characteristics downstream of separation for closed-loop forcing. (a) Streamwise velocity $\overline{U}$, (b) transverse velocity $\overline{V}$ and (c) kinetic energy k. ——— Baseline flow; -·-·- controller K_1; ------ controller K_2.

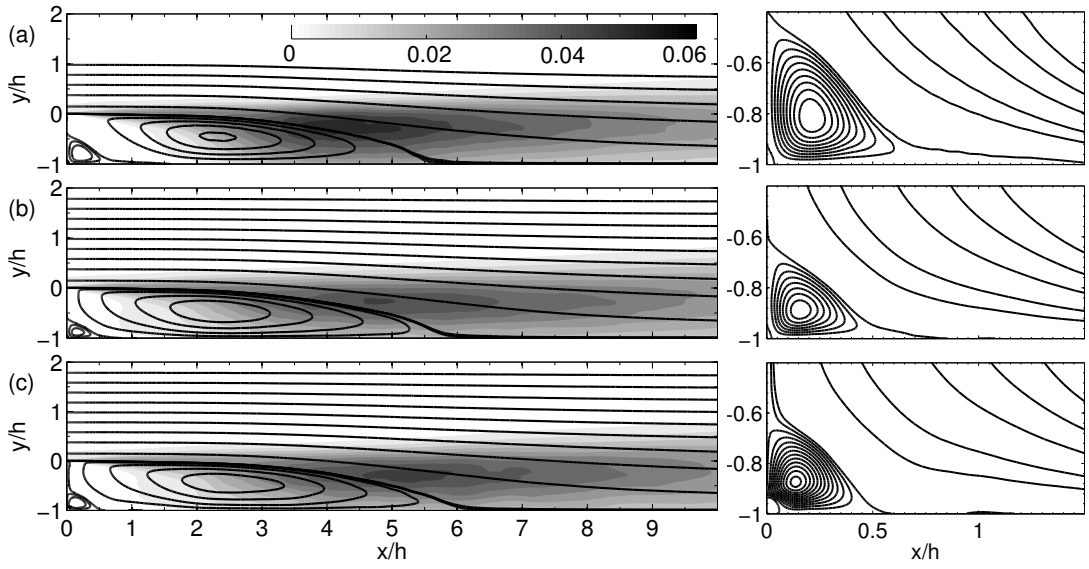


Figure 7.19: Line contours of the time-averaged streamfunction on colour contours of turbulent kinetic energy k. The baseline flow is shown in (a) and the controllers K_1 and K_2 are shown in (b) and (c) respectively. The right part of the figure shows a zoom on the base foot region.

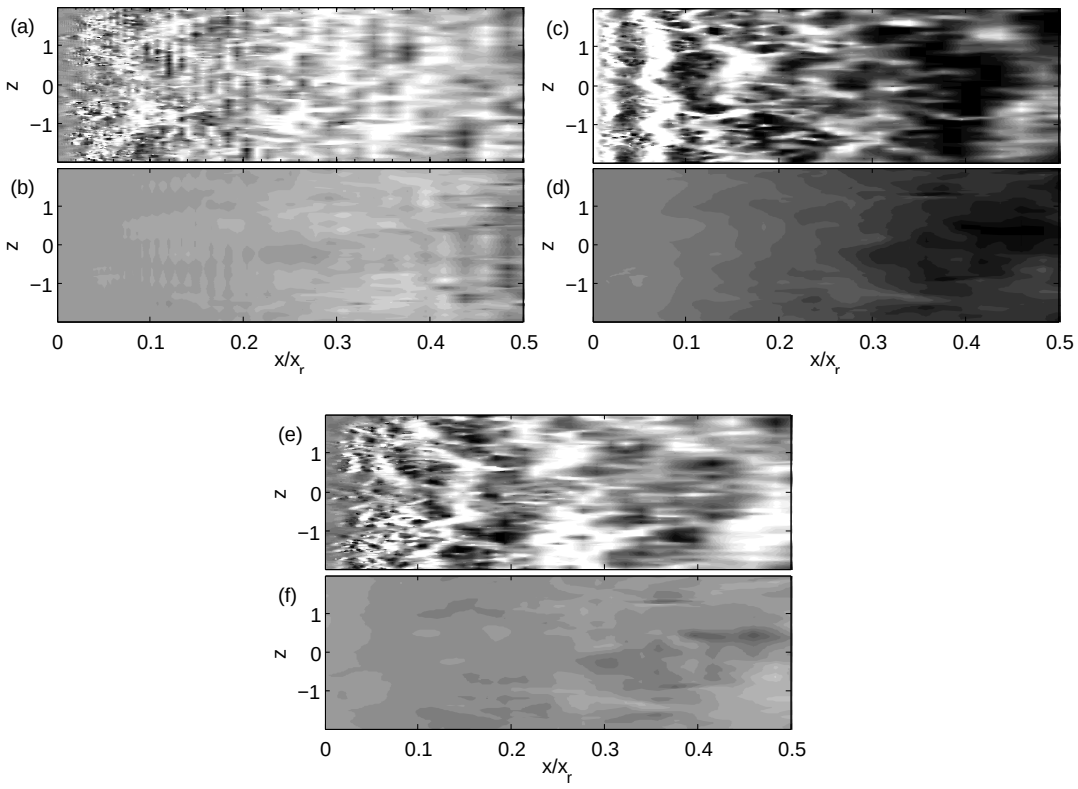


Figure 7.20: Instantaneous contours of pressure coefficient, C_P for the (a,b) uncontrolled, (c,d) controller K_1 and (e,f) controller K_2 cases. Two horizontal planes are considered: (a,c,e) the separation plane y=0 and (b,d,f) the lower wall y=-1. The contours go from white ($C_P = -0.05$) to black ($C_P = 0.05$).

The reduction in pressure fluctuations attenuates this mechanism which is one of the causes for the increase in base pressure observed with the closed-loop control. The attenuation of the shear layer and shedding modes leads to reduced dissipation and smaller losses in stagnation pressure.

Instantaneous pressure contours in the planes y=0 and y=-1 (the separation plane and the lower wall) are presented in figure 7.20 with and without control. Alternating spanwise structures of high and low pressure can be identified for the baseline and both controlled flows, but K_1 produces tighter and more 2D structures in the initial stage of the shear layer, before successive structures appear to merge. K_2 on the contrary leads to higher three-dimensionality and localized high pressure spots are apparent.

7.7 Summary

Using LES, we have accurately numerically simulated the 3D backward-facing step flow with turbulent separation. This flowfield was analyzed in the absence and presence of forcing, via slot jet actuators, with two actuation locations considered. It was observed that open-loop forcing can have a significant impact on the mean base pressure force.

Following the approach tested in the previous chapter, we characterized the response of the base pressure force to open-loop harmonic forcing and used system identification tools to derive a low-order linear model for this response. Finally, feedback controllers were designed using a frequency-domain sensitivity approach. We synthesized robust controllers with the desired sensitivity gain distribution, in order to reduce the base pressure fluctuations.

With both actuator locations, the controllers yield satisfactory results: a base pressure rise of 20% is obtained with K_1, while limiting the actuation amplitude to remain roughly within the range of linearity studied. We confirm that the first actuator location is better suited for our purposes. However, controller K_2 is surprisingly able to damp the base pressure fluctuations significantly. Finally, we observe that the link between the pressure fluctuations and the mean is not straightforward, and further work will be required before it can be used for optimization.

Chapter 8

Reynolds number effects and flow mechanisms

8.1 Background

Let us consider once again the backward-facing step flow in the same domain Ω_{3D} as considered in the previous chapter (see figure 5.1a). A higher Reynolds number $Re_h = 4 \cdot 10^4$, corresponding to $Re_\theta = 3000$, is imposed to evaluate the effect of the Reynolds number on the flow and on the control strategy.

The computational cost involved with well-resolved simulations of this flow at this Reynolds number is high. Consequently, the code was ported to the UK high-performance computing facility HECToR. The simulations presented in this chapter were run on up to 768 cores. A new turbulent inflow database is generated for this higher Reynolds number.

We aim to assess whether this control strategy could still be applied at the much higher Reynolds numbers encountered in real-life bluff body applications such as road vehicles. At the same time, we attempt to complete our understanding of the mechanisms governing the baseline and controlled flows by studying them further.

We follow a similar route as that of chapter 7. In §8.2, we rapidly describe the grid and evaluate its resolution. We look into the baseline flow in §8.3 and the effects of open-loop forcing in §8.4. A new controller is designed and implemented in §8.5, where we end with a discussion on control efficiency.

Grid	Δz^+	x_r	$(x_r - x_{r0})/x_{r0}$ (%)
Nominal	18	8.5	0 %
Fine_x	18	8.63	1.5 %
Fine_z	12	8.4	-1.2 %

Table 8.1: Summary of grids tested showing the time-averaged reattachment length x_r obtained.

8.2 Grid resolution

In order to allow for a direct comparison with the lower Reynolds number case studied in chapter 7, the same domain dimensions are prescribed for Ω. A grid resolution study is again carried out as described previously. In addition to the nominal grid, two grids with refined streamwise and spanwise cell spacing are tested.

Regarding the transverse distribution of nodes, it was found from previous tests that a spacing close to $\Delta y^+ = 1$ is essential near the inlet wall and in the injection region in order to resolve the boundary layer and the higher end of actuation frequencies considered. Much larger spacings can be used if combined with semi-empirical wall models, also termed wall laws, but these are likely to incur strong penalties in terms of accuracy [133]. In addition, the cell expansion ratio in the y-direction must not be too large so as to seed enough nodes inside the boundary layer and avoid large gradients in the grid. Given that L_y is relatively short ($L_y = 3$), these two requirements essentially dictate the necessary grid-spacing in the transverse direction.

The reattachment lengths obtained with the three grids are listed in table 8.1. The two finer grids predict a mean reattachment length x_r within 2% of the nominal value, suggesting that the nominal grid has a sufficient resolution in the streamwise and spanwise directions. Compared with the flow at $Re_h = 2 \cdot 10^4$, x_r is almost 40% higher, showing that the previous flow was not fully developed, since Armaly et al. [5] showed the reattachment length to be essentially independent of the Reynolds number for fully developed turbulent flows.

The distributions of cell dimensions are plotted in figure 8.1 along the x and y directions for the three grids above. As for the lower Reynolds number case, the maximum aspect ratio of cells is kept below 100 and the expansion ratios do not exceed 1.05.

The distributions of skin friction and pressure coefficients along the lower wall, downstream

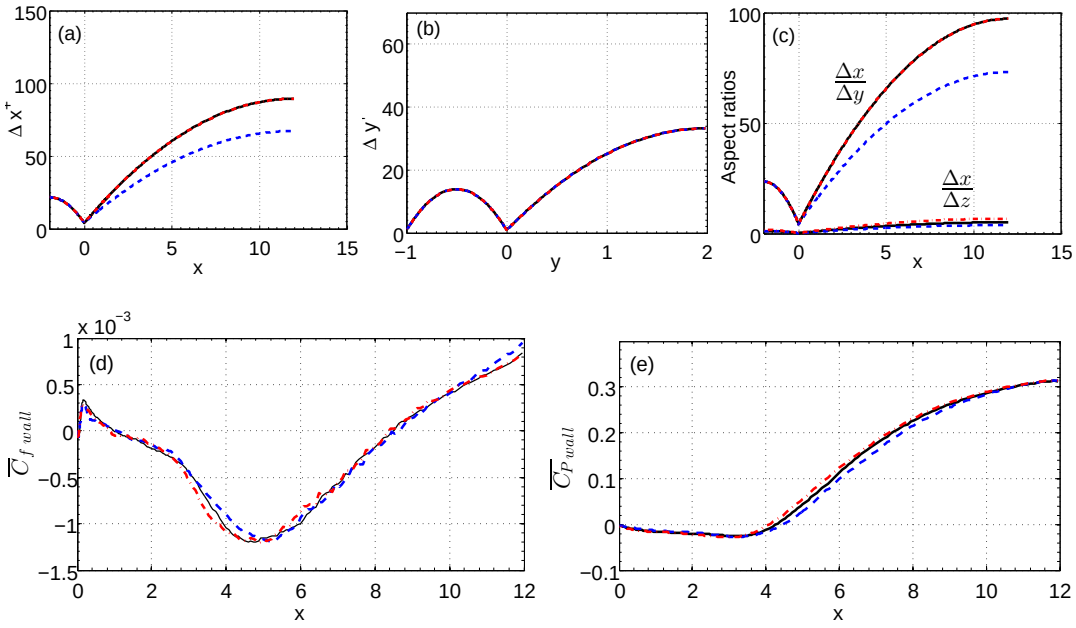


Figure 8.1: (a,b,c) Computational cell characteristics, (d) skin friction distribution and (e) pressure distribution along lower wall, for the three grids listed in table 8.1. Nominal grid ——; *Fine_x* - - -; *Fine_z* -·-·-.

of the step, are given in the lower part of figure 8.1. All three solutions are in very good agreement with the nominal grid, which validates the use of the latter grid. $\overline{C}_f$ and $\overline{C_P}$ along the lower wall are qualitatively similar to the lower Reynolds number case. We note that the minimum skin friction occurring around $x = 5$ is about $\overline{C}_{f\,wall} = -0.0012$ which is the value obtained experimentally by Eaton & Johnston [38]. For the lower Reynolds number case studied in the previous chapter, a lower minimum was found, $\overline{C}_{f\,wall} = -0.002$. Le et al. [86] performed a DNS of a turbulent backward-facing step flow and have also remarked that the skin friction coefficient on the lower wall is significantly higher at low Reynolds numbers.

8.3 Baseline flow

Let us consider the main aspects of the baseline flow. We endeavour to compare this case with the lower Reynolds number, as well as further our discussion of the flow mechanisms at play in the backward-facing step flow.

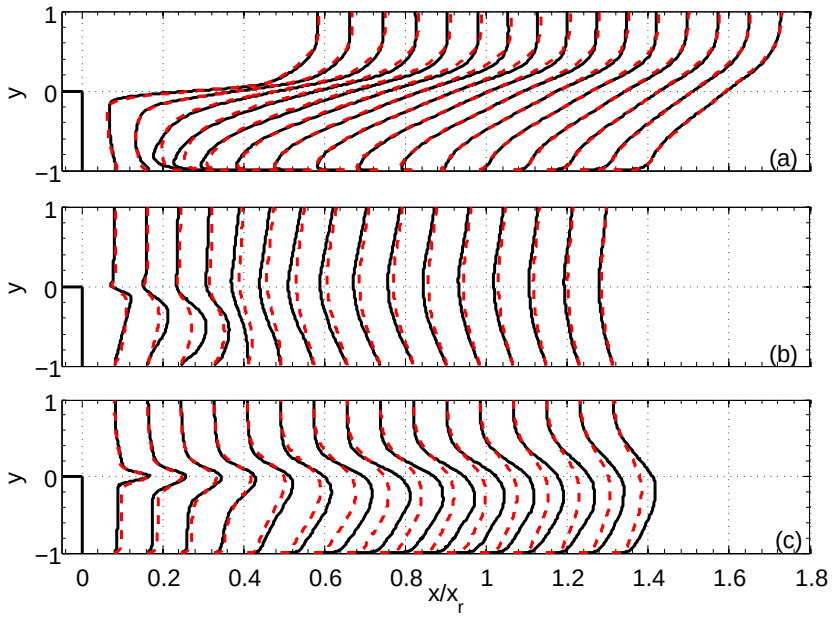


Figure 8.2: Time-averaged profiles of (a) $\overline{U}$, (b) $\overline{V}$ and (c) k, downstream of separation. —— $Re_h = 2 \cdot 10^4$; - - - - $Re_h = 4 \cdot 10^4$.

8.3.1 Time-averaged flow

We start with mean flow statistics. Figure 8.2 shows time-averaged flow profiles comparing the uncontrolled flows at the two Reynolds numbers $Re_h = 2 \cdot 10^4$ and $4 \cdot 10^4$. The solid and dashed lines denote the lower Reynolds and higher Reynolds cases respectively. The streamwise velocity profiles plotted in figure 8.2a collapse perfectly except in a small region $0.2 \leq x/x_r \leq 0.4$ within the recirculation bubble. This is the region of strongest backflow and one can observe that the amplitude of the backflow is reduced by the increase in Reynolds number.

The positive peaks in transverse velocity $\overline{V}$, marking the passage of large-scale vortical structures convected downstream by the shear layer, are also seen to be lower in figure 8.2b at $Re_h = 4 \cdot 10^4$. Consequently, the entrainment of outer fluid from above the shear layer, indicated by the negative peaks of $\overline{V}$, is also reduced.

Finally, the most striking difference between the two flows appears in the profiles of turbulent kinetic energy. The peaks are significantly lower for the higher Reynolds number case. These results concur with the reduced magnitude of the skin friction coefficient along the lower wall for this higher Reynolds case and confirm that the turbulent separated flow is not fully developed at $Re_h = 2 \cdot 10^4$.

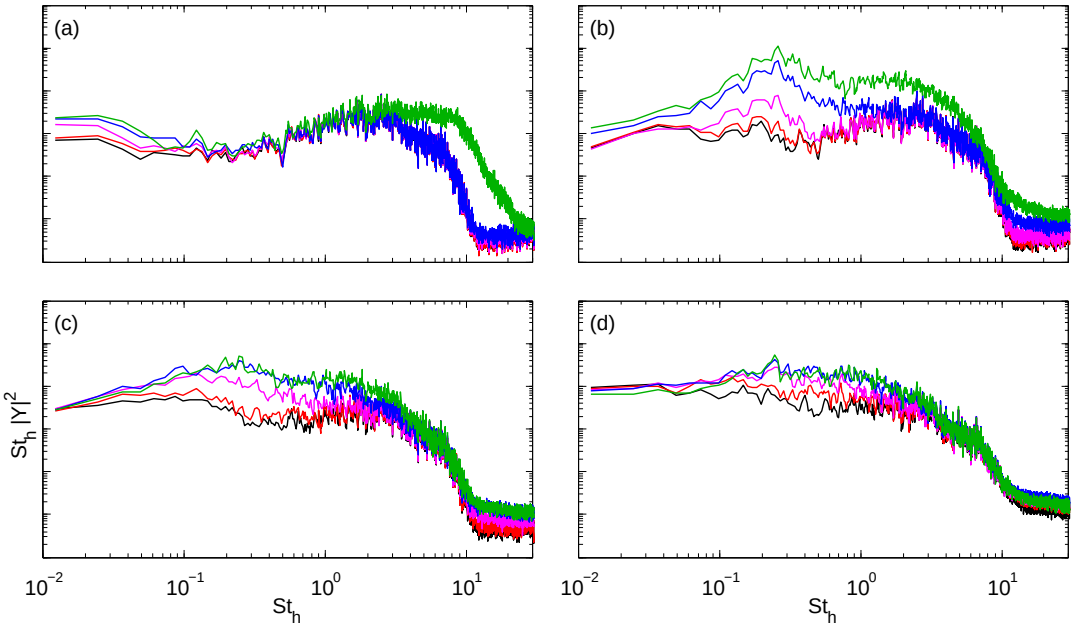


Figure 8.3: Pressure spectra downstream of separation, along z=0. (a) x=0, (b) x=2, (c) x=4, (d) x=6. y=0; y=-0.25; y=-0.5; y=-0.75; y=-1 (lower wall).

8.3.2 Spectral analysis and correlation

The aim of this section is to gain further insight into the dynamics of the uncontrolled flow and study the consequences of the increase in Reynolds number on its behaviour. For this purpose, we once again perform spectral analysis of pressure signals inside the recirculation bubble and then examine autocorrelations of the fluctuating pressure field.

Figure 8.3 shows pressure spectra at four streamwise locations downstream of separation. The spectra at $x = 0$ (on the base) are plotted in figure 8.3a. As for $Re_h = 2 \cdot 10^4$, most of the fluctuating energy is concentrated near the upper edge of the step, at $y = 0$. Stronger fluctuations at high frequencies for $y = 0$ result from residual small eddies present in the upstream boundary layer. The most interesting perspective observed here is the presence of a hump at very low frequencies. This hump reveals the flapping motion of the shear layer which was not observable in the previous case. A peak is also observed for all values of y near $St_h = 0.1$, corresponding to the shedding mode. Note that the shear layer instability is not strongly felt at the base yet.

On the other hand, at $x = 2$ the shear layer mode becomes strongly dominant, although it is more broadband in this case than observed in chapter 7. In accordance with previous

remarks, the spectra slowly shift to lower frequencies with increasing streamwise distance from separation and the power density of fluctuations spreads throughout the entire height of the bubble.

Another related way to visualize spatio-temporal coherence in a turbulent flow is via cross-correlations. Here we compute the autocorrelation function for pressure, given by:

$$R_{pp}(\mathbf{x}, \Delta t) = \frac{1}{(n - \Delta t)(\sigma_p)^2} \sum_{k=1}^{n-\Delta t} p(\mathbf{x}, t_k)\, p(\mathbf{x}, t_k + \Delta t). \tag{8.1}$$

In (8.1), the discrete form of the autocorrelation function is shown for a time series with n equally spaced samples at times $(t_1, t_2, ..., t_n)$, assuming the flow is a stationary process. The time delay is denoted by Δt and σ_p is the root-mean-square value of the pressure fluctuations $p(\mathbf{x}, t)$. Since the signals contain a finite number of samples n, the field of view is limited and the number of data points decreases linearly as the magnitude of the time delay Δt increases. The averaging takes this into account by dividing by the number of samples $n - \Delta t$. With definition (8.1), the range of the correlation coefficient is $[-1; 1]$, with 1 indicating perfect correlation, -1 perfect negative correlation and 0 signalling no correlation.

Figure 8.4 shows maps of the autocorrelation function $R_{pp}(\Delta t)$ for points below separation ($y \leq 0$) at four streamwise stations (x=0, x=2, x=4 and x=6). In all cases, R_{pp} is obviously 1 for $\Delta t = 0$ and decreases with increasing time delay. The plots are symmetrical about the y-axis, so only positive time delays are shown so as to make the plots clearer.

The first plot illustrates the autocorrelation on the base (x=0). There is a parabolic region of very high correlation for small time delays, centered around $y \approx -0.2$ and extending from the step edge down to $y \approx -0.7$. The fact that this zone is centered around $y = -0.2$ rather than peaking at $y = 0$ (where the shear layer starts to develop) is surprising. It suggests that this high correlation is caused by the shedding, rather than being associated with the shear layer instability. This correlates with our previous observation from figure 8.3a, namely that the shear layer instability is not strongly felt on the base, whereas the shedding mode is observable.

The motion of the reattachment due to the shedding pushes high momentum fluid into the recirculation bubble that impinges on the base near $y = -0.2$. Furthermore, note that this high correlation is spread over a wide band of time delays. We postulate that this reflects an interaction between the shedding mode and the flapping, which modulates the frequency of the former. Given that the effects of the flapping are concentrated in the flow near separation,

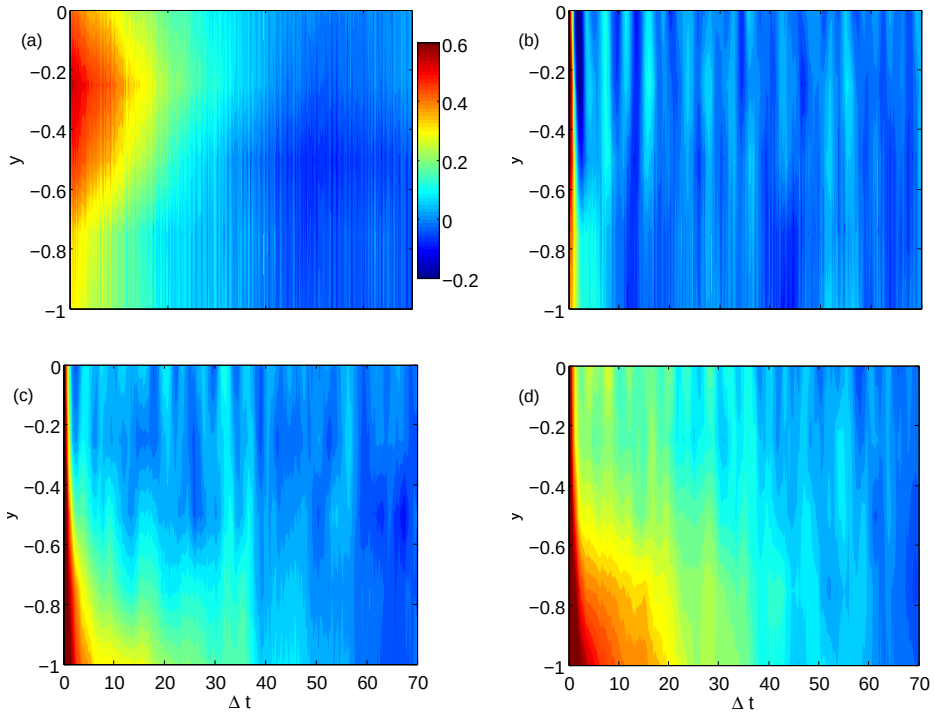


Figure 8.4: Contours of autocorrelation function $R_{pp}(\mathbf{x}, \Delta t)$ downstream of separation. (a) x=0, (b) x=2, (c) x=4 and (d) x=6.

this is where this modulation is most observable.

At x=2 (figure 8.4b), the region of high correlation has disappeared. The magnitude of R_{pp} drops down to small values very fast, showing the absence of large-scale low frequency structures. On the other hand, thin finger-like structures of small, alternatively positive and negative correlation drop down from the upper edge of the plot. These are spaced apart by about $\Delta t \approx 4$, or a frequency of $St_h \approx 0.25$. Thus, they are linked to the shear layer instability, which is seen to affect the bubble from its upper edge down to $y = -0.6$.

Finally, in figures 8.4c and 8.4d, the shear layer expands towards the lower wall and large-scale structures associated with the highly unsteady reattachment region develop.

8.3.3 Instantaneous pressure field

The time-averaged pressure field downstream of the step does not reveal much about the dynamics of the flow and is dominated by the large streamwise pressure gradient imposed by the expansion. On the other hand, the instantaneous pressure field can be investigated to gain some insight into the development of the shear layer and the behaviour of coherent structures in the bubble.

Figure 8.5 shows instantaneous isosurfaces of pressure downstream of separation viewed in a horizontal plane and a vertical plane. Negative pressure $C_P = -0.02$ and positive pressure $C_P = 0.02$ contours are marked. Spanwise structures can be detected from figure 8.5a, corresponding to vortical structures formed by the roll-up of the shear layer. Vortex mergings are also observed as branches connecting these structures. Low-pressure structures dominate the separated shear layer. The streamwise growth of those low-pressure structures within the shear layer can be visualized by figure 8.5b.

Random bursting events in velocity or pressure signals recorded inside recirculation bubbles have been reported by several authors (see, e.g., Cherry et al. [18], Castro & Haque [15] and Spazzini et al. [129]). It is interesting to investigate whether such bursts are observable from the base, via the sensor measurement that will be used for control. Figure 8.6a shows a short sample of a (spatially-averaged) base pressure time series. A burst is clearly visible in the signal at t=726.

Two instantaneous contours of pressure over the base are examined to gain some insight into the causes of this bursting event. The contours are saved at two times corresponding to a local minimum and local maximum C_P during the burst, as indicated by the blue dots in

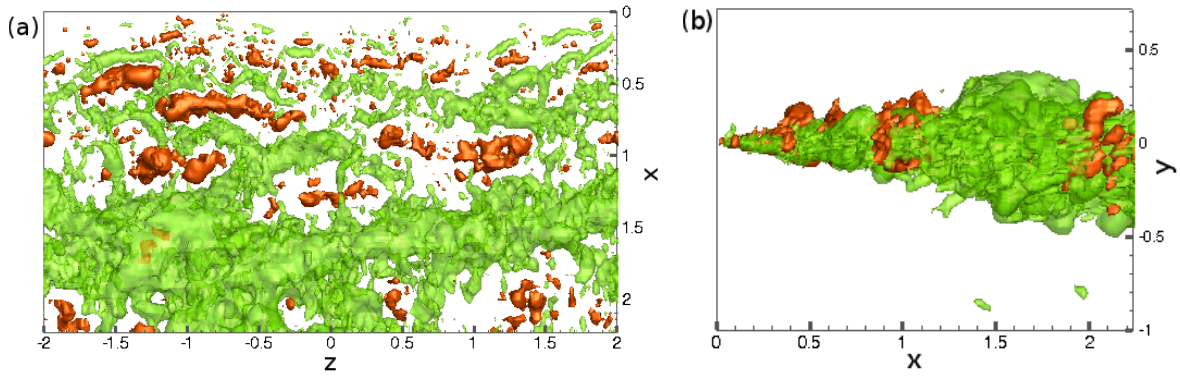


Figure 8.5: Instantaneous isosurfaces of pressure coefficient C_P for the baseline flow, (a) top view and (b) side view. Green surfaces correspond to negative pressure $C_P = -0.02$ while red surfaces corresponds to positive pressure $C_P = 0.02$.

figure 8.6.

The contours corresponding to $C_{P,min}$ and $C_{P,max}$ are shown in figures 8.6b and 8.6c respectively. For both plots, the contours range from $C_P = -0.1$ (white) to $C_P = 0.1$ (black). A striking result is that the flow structures delineated by the contours are very similar for the valley and peak of the burst; i.e. there are no significant changes in the local flow structures near the base. However, the pressure increases over the whole base due to the burst. This shows that such pseudo-periodic events are associated with global changes in the bubble. In particular, it appears that it is a cycle of expansion and contraction of the bubble, connected to the low-frequency flapping of the shear layer, that causes the bursts. A slow expansion is followed by a sudden contraction that raises the pressure in the recirculating region and interacts with the shear layer near separation.

8.4 Open-loop forcing

Open-loop harmonic forcing with the slot jet actuator located near separation (previously referred to as the first actuator location) is examined here. The results are contrasted with that of the lower Reynolds $Re_h = 2{\cdot}10^4$ flow by forcing at the same amplitudes and frequencies.

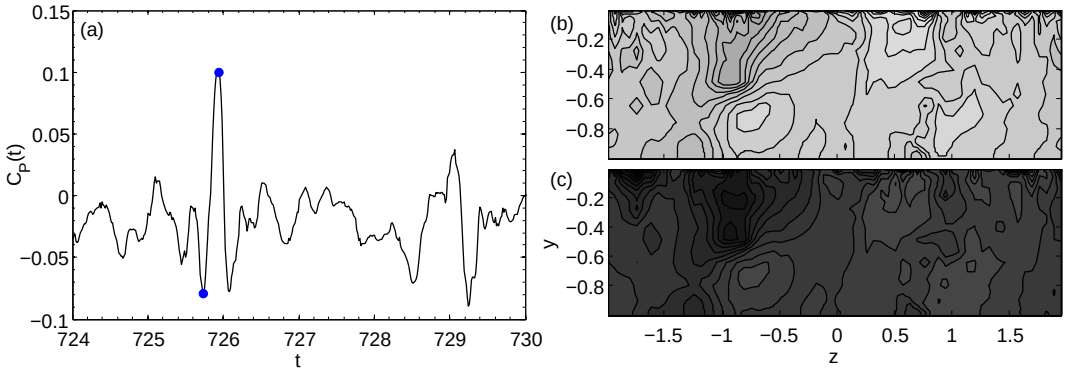


Figure 8.6: (a) Short sample realization of the base pressure time series showing a bursting event and (b,c) instantaneous isocontours of base pressure corresponding respectively to the local minimum and maximum pressure indicated by blue points in (a).

8.4.1 Physical insight

We introduce harmonic perturbations via the actuator, which are expected to lead to changes in the harmonic part of the sensor signal, as well as in its mean due to non-linear effects. Figure 8.7 illustrates the effect of harmonic forcing on the time-averaged reattachment length x_r and base pressure $\overline{C_P}$. The full symbols denote the flow case considered in chapter 7 while the open symbols refer to the current flow. To improve the clarity of the plots, trend lines are added and only two forcing amplitudes are shown. Although there is no qualitative change in the trends with the increase in Reynolds number, the case at $Re_h = 4 \cdot 10^4$ is significantly more responsive to harmonic actuation.

The maximum reduction in the extent of the recirculation bubble exceeds 40%, as opposed to roughly 30% for the lower Reynolds. Similarly, a more significant increase in the bubble size is achieved at high frequencies. As for $\overline{C_P}$ on the base, the pressure bucket is also extended. For harmonic forcing with amplitude $A_j = 0.2$ and frequency $St_h \approx 0.25$, the pressure on the base drops by about 150% of its unforced value. Reducing the base pressure (and consequently increasing form-drag) is child's play compared to the task of reducing the drag.

Nonetheless, increases in the base pressure force at the low and high frequency ends of the range are still observed, although the increase at low frequencies seems to be lesser at higher Re. It is postulated that a higher pressure force increase will be obtained for the high Reynolds if forcing frequencies below $St_h = 0.06$ are considered. However, such low-frequencies require very long simulations in order to obtain converged averages and they may exceed the typical

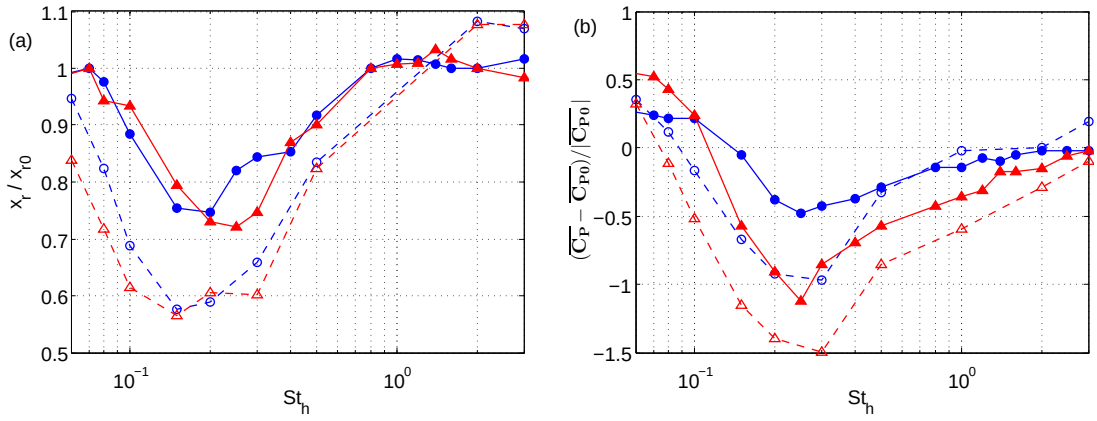


Figure 8.7: Effect of open-loop forcing on time-averaged (a) reattachment length x_r and (b) base-pressure $\overline{C_P}$. The zero subscript denotes the baseline case. Two forcing amplitudes are shown: $A_j = 0.1$ (●) and $A_j = 0.2$ (▲). The lower and higher Reynolds number flows are denoted by the filled and open symbols respectively.

range of standard actuators used in experiments.

8.4.2 System identification

Figure 8.8 presents the frequency response $G(i\omega)$ obtained from system identification with harmonic forcing. The assumption of dynamic linearity is verified again by considering three forcing amplitudes. As evidenced by figure 8.8a, weak non-linearities are present in both gain and phase, but appear small enough (maximum discrepancies between different amplitudes of 2.8dB and 7.6°) to be compensated by the robustness of the controller. The data is averaged over the three amplitudes and fitted with a second order model via least-squares minimization.

The model is given by:

$$G(s) = \frac{71.42s + 539.3}{s^2 - 494.7s - 1520}. \tag{8.2}$$

A comparison with the fit obtained for the lower Reynolds number case is shown in figure 8.8b. The increase in Reynolds number has not significantly affected the input-output relationship of the flow system since the two frequency responses are very close. Interestingly, a small increase in gain, roughly uniform over the frequency band examined, is observed for the higher Reynolds number. This suggests that the increase in Reynolds brings a benefit in terms of control authority.

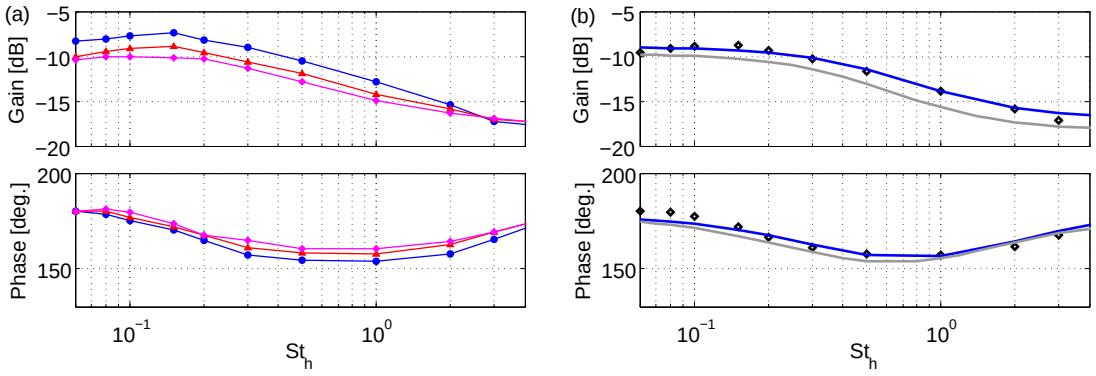


Figure 8.8: Bode plots of frequency responses $G(i\omega)$. (a) Frequency responses for different forcing amplitudes: (●) $A_j = 0.1$, (▲) $A_j = 0.2$ and (♦) $A_j = 0.3$. (b) Frequency response averaged over three amplitudes (◇); ——— second order model fit; ——— $G(i\omega)$ for lower Reynolds number.

8.5 Closed-loop control

8.5.1 Control synthesis

A controller is designed via H_∞ loop-shaping, following the same procedure as in chapter 7. The target of the control synthesis is a small sensitivity magnitude (corresponding to a negative gain in dB) over the range of frequencies covering the dominant instability modes of the flow, including low frequencies and the large hump discussed in §8.3.2.

Frequency domain characteristics of the control system are plotted in figure 8.9a. The controller K is qualitatively similar to the previous design, although a fast roll-off of the gain slope at high frequencies is necessary to prevent the amplification of spurious numerical disturbances at very high frequencies in the LES.

The continuous-time transfer function of the resulting controller is

$$K = \frac{-3.115 \cdot 10^{13}}{s^6 + 1131s^5 + 5 \cdot 10^5 s^4 + 10^8 s^3 + 1.2 \cdot 10^{10} s^2 + 5.8 \cdot 10^{11} s + 5 \cdot 10^{12}}. \tag{8.3}$$

The coefficients are dramatically reduced when the controller is expressed in discrete form with a small time-step, which is the form used for the control. The resulting control system has high stability margins; the gain margin is 7.8 and the phase margin is 113°.

The controller K is implemented in the LES and frequency-domain results for the input and output signals are given in plots 8.9b and c. As expected, the amplitude of the fluctuations

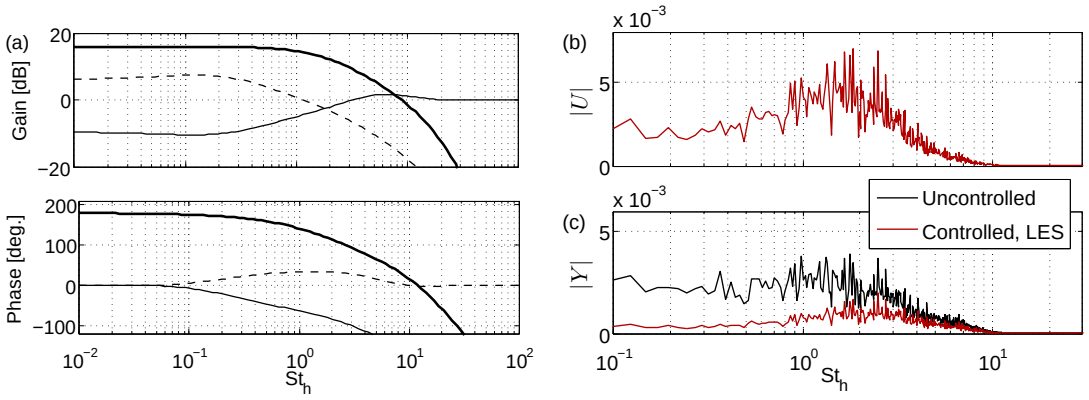


Figure 8.9: (a) Frequency-domain characteristics of the closed-loop system. In the Bode diagram, the controller K is denoted by the thick solid line, the open-loop transfer function $L = GK$ by the dashed line and the sensitivity S by the thin solid line. (b) Input and (c) output signals in the frequency-domain for the controlled flow.

is reduced over a large frequency band. Despite the small positive bump in the sensitivity gain around $St_h = 8$, fluctuations around this frequency are not made larger by the controller.

Rather than being good news, this reflects the limitations of the linear flow response model. The model deviates from the true flow response so that the sensitivity gain appears mildly positive although it is not. Nevertheless, it seems that the limitations of the model can be successfully mitigated by a conservative design. The actuator signal is *active* in the same frequency range as the sensor measurement. Finally, the controller raises the mean base pressure by 22%, which exceeds the performance observed at the lower Reynolds.

A short sample of the same input and output signals in the time domain is presented in figure 8.10. The LES results are compared with theoretical predictions from linear control theory. These predictions assume that the noise is given by the unforced sensor measurement. It is remarkable that an excellent agreement is obtained between the linear time-invariant model and the non-linear (non time-invariant) simulation of the turbulent separated flow.

8.5.2 Flow mechanisms

We turn our attention to the effects of the control on the flow, in an attempt to bring a brief complement to the discussion in §7.6. First, we compare maps of autocorrelation between the baseline and controlled flows and then examine the impact of control on vortical regions in the wake.

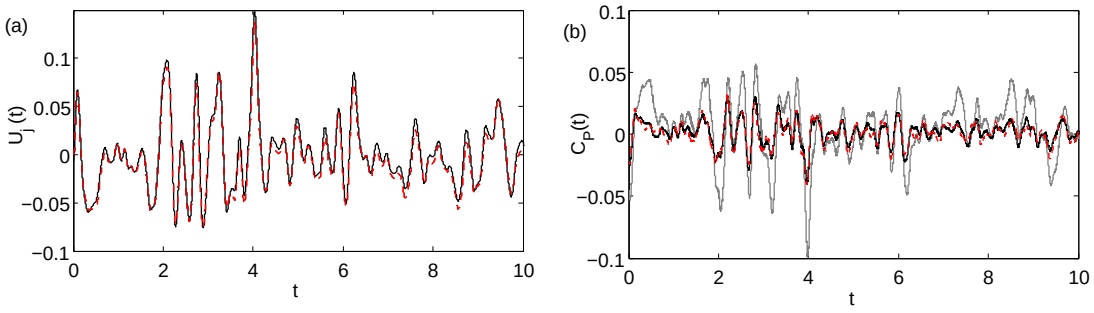


Figure 8.10: Time series of (a) actuator and (b) sensor signals comparing the signals measured in the LES (——) with linear control theory (- - - -). The unforced base pressure (——) is shown as a reference in (b).

Figure 8.11 shows contours of the autocorrelation function $R_{pp}(\mathbf{x}, \Delta t)$ for the controlled flow. The plots use the same colour scheme as figure 8.4, to allow for direct comparison with the baseline flow. There are three main points to note.

Firstly, the two regions of high correlations that were observed in figure 8.4 near separation and in the reattachment region are not visible here, showing that the controller damps out large-scale coherent structures. This was expected, since the goal of the controller is to reduce the amplitude of fluctuations on the base.

Secondly, note the appearance of large regions of alternate positive and negative (weak) correlation near the base, at x=0 and x=2. These are more defined at x=2 (figure 8.11b), where the negative regions are centered around $\Delta t \approx 25$ and $\Delta t \approx 60$. Correlations for such large time-delays mark the presence of a low-frequency motion induced by the controller, close to the lower wall. This phenomenon has not been explained yet, and will require further work. The spectra in figure 8.9b do not reveal any hints of the controller enhancing low frequency perturbations. However, note that this phenomenon is only very weakly observable on the base in figure 8.11a and the sensors only capture the base pressure. In addition, longer time series might be required to improve the accuracy of the Fourier spectra at very low frequencies.

Finally, one can observe that the controller enhances the finger-like structures mentioned in section 8.3.2. Again, this was not detected by the sensors because this phenomenon seems to only affect the flow downstream of the base.

As explained by Haller [52], there are several criteria in use to define or visualize vortices. Among them, the Q-criterion introduced by Hunt et al. [65] defines a vortex as a spatial

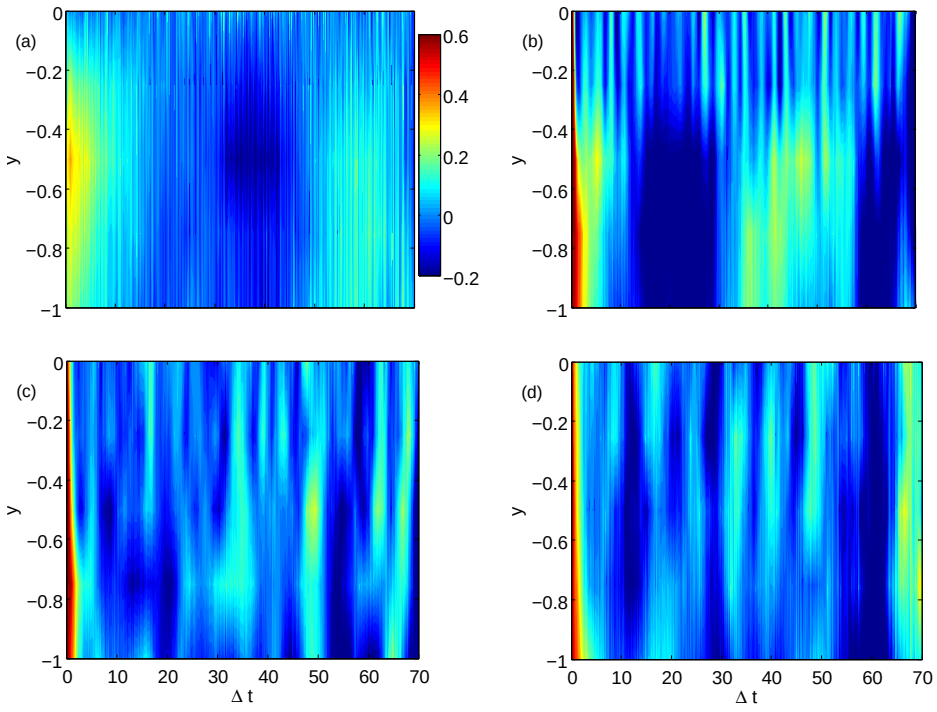


Figure 8.11: Autocorrelation function $R_{pp}(\mathbf{x}, \Delta t)$ of pressure signals downstream of separation for the controlled flow. (a) x=0, (b) x=2, (c) x=4 and (d) x=6.

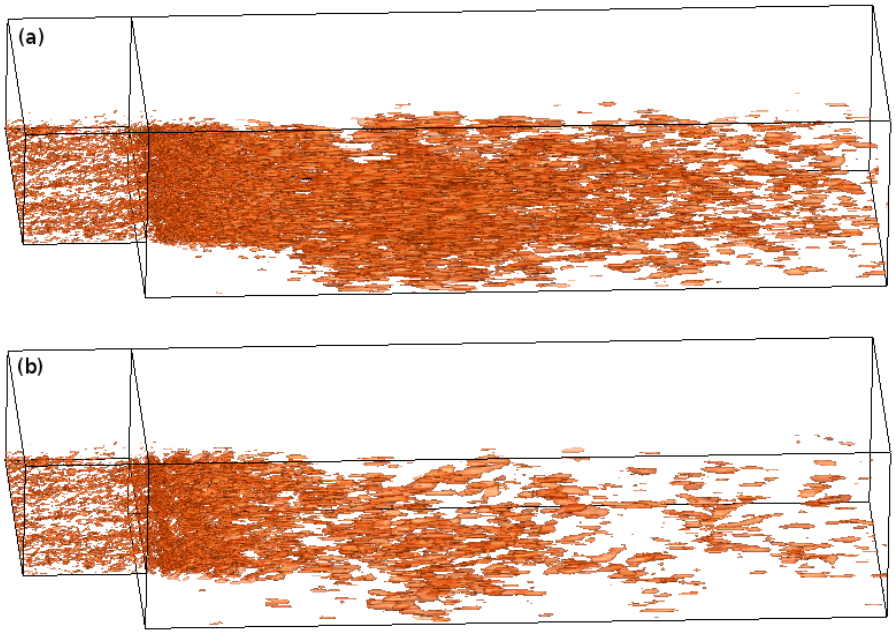


Figure 8.12: Instantaneous isocontours of Q=5 for (a) the baseline and (b) controlled flows, obtained with grid *Fine_z*.

region where the L_2-norm of the vorticity tensor $\Omega_{ij} = 0.5(\frac{\partial u_i}{\partial x_j} - \frac{\partial u_j}{\partial x_i})$ (not to be confused with the computational volume) dominates that of the rate-of-strain tensor $S_{ij} = 0.5(\frac{\partial u_i}{\partial x_j} + \frac{\partial u_j}{\partial x_i})$. Vortices are found in flow regions of positive Q:

$$Q = \frac{1}{2}\left(|\Omega|^2 - |S|^2\right) > 0 \tag{8.4}$$

Figure 8.12 plots instantaneous contours of Q=5 for the baseline and controlled flows. The Q-criterion can educe small-scale structures, which are not necessarily well resolved in LES. Therefore, the grid *Fine_Z* was used in order to reduce the reliance on the subgrid-scale model to compute such structures.

The controller damps out vortical activity in the initial stages of the shear layer, which slows down its growth rate. As explained above, this results in lower mixing and entrainment and consequently in a longer reattachment length. Interestingly, the most visible impact is the reduction of the presence of vortical structures in the reattachment region and downstream.

8.5.3 Efficiency considerations

A measure of the actuation cost is needed to compare the performance of the feedback control to the highest efficiency obtained with the open-loop forcing. We quantify the actuation cost

	Open-loop			Closed-loop		
	$\Delta\overline{C_P}$	c_μ	$\mathcal{J}$	$\Delta\overline{C_P}$	c_μ	$\mathcal{J}$
Actu. 1, $Re_h = 2 \cdot 10^4$	0.24	$1.5 \cdot 10^{-4}$	1600	0.2	$1.2 \cdot 10^{-4}$	1667
Actu. 2, $Re_h = 2 \cdot 10^4$	—	—	—	0.1	$1.44 \cdot 10^{-4}$	694
Actu. 1, $Re_h = 4 \cdot 10^4$	0.4	$1.5 \cdot 10^{-4}$	2666	0.22	$3.4 \cdot 10^{-5}$	6470

Table 8.2: Base pressure increase $\Delta\overline{C_P}$, momentum coefficients c_μ and merit functions $\mathcal{J}$ for open-loop and closed-loop control. For the open-loop, the numbers shown correspond to the harmonic input with the highest merit function obtained.

with the momentum coefficient, $c_\mu = sU_{j,rms}^2/(hU_0^2)$, where s is the actuator width. We define the efficiency of an open-loop or closed-loop control scheme with the simple merit function $\mathcal{J}$, defined as

$$\mathcal{J} = \Delta\overline{C_P}/c_\mu = (\overline{C_P} - \overline{C_{P0}})/(c_\mu\overline{C_{P0}}), \tag{8.5}$$

where $\overline{C_{P0}}$ is the time-averaged base pressure for the baseline case.

Table 8.2 recapitulates the base pressure increases obtained with all the 3D backward-facing step cases discussed above. It also gives the corresponding momentum coefficients and merit functions obtained with the best open-loop control (the one with the highest merit function) and with feedback control, for the two actuator locations and Reynolds numbers considered.

Considering actuator 1 at $Re = 2 \cdot 10^4$, the highest merit function with open-loop forcing is achieved with an amplitude $A_j = 0.1$ and forcing frequency $St_h = 0.05$. The corresponding momentum coefficient and mean pressure increase are $c_\mu = 1.5 \times 10^{-4}$ and 24% respectively, which yields $\mathcal{J} = 0.24/(1.5 \times 10^{-4}) = 1600$.

The controller K_1 *costs* $c_\mu = 1.2 \times 10^{-4}$ for a 20% increase in $\overline{C_P}$. Hence, its merit function is $\mathcal{J} = \Delta\overline{C_P}/c_\mu = 0.2/1.2 \times 10^{-4} \approx 1667$. Therefore, the feedback controller K_1 is more efficient than the corresponding open-loop forcing. Regarding the secondary actuator, no sensible pressure increase was measured in open-loop whilst the controller K_2 has a merit function $\mathcal{J} = 694$, which leads us to conclude that the first actuation location is a more appropriate choice to increase the base pressure and hence reduce form-drag.

The most interesting feature to note is that, at the higher Reynolds, where it seems that the turbulence in the separated flow is fully developed (by comparison of time-averaged features such as skin friction and reattachment length with values obtained experimentally at much

higher Reynolds), the efficiency of the control is dramatically larger. In these conditions, the benefits of using a closed-loop controller over harmonic forcing also become more apparent. Furthermore, the closed-loop results above were obtained with little consideration for actuation cost (the main focus was to bound actuation amplitude to remain within the linearity range examined). Investigations with optimal control tools are expected to reduce the momentum coefficient required in the closed-loop case. Perhaps more importantly, enhancing the current black-box models of the flow behaviour by inclusion of knowledge about the dynamics may provide significant gains in performance. This looks like a promising route to follow in the future.

8.6 Summary

The flow domain Ω_{3D} considered previously was again examined at a higher Reynolds number of $Re_h = 4 \cdot 10^4$. We examined the effects of this parameter on the baseline and controlled flows. It was observed that the lower Reynolds number of $Re_h = 2 \cdot 10^4$ (corresponding to $Re_\theta = 1500$) is not sufficient to obtain a fully developed downstream flow, despite the realistic turbulent boundary layer imposed at the inlet. However, we remark that the main features of the flow remain qualitatively very similar at $Re_h = 4 \cdot 10^4$. Interestingly, the increase in Reynolds seems to bring along a better control authority, leading to opportunities for more efficient control.

In addition, we attempted to further our understanding of the fluid mechanics for both the baseline and controlled cases. In particular, we performed a spectral and correlation analysis to educe the coherence that, to a large extent, dictates the dynamics of the recirculation bubble.

Finally, we remarked that the control strategy based on the fluctuations and using the sensitivity approach accomplishes a sensible rise in time-averaged base pressure for the flow at $Re_h = 4 \cdot 10^4$.

Chapter 9

D-shaped bluff body

9.1 Background

This chapter forms a preliminary investigation of the control of the D-shaped bluff body flow. For this purpose, we numerically simulate the flow in the domain Ω_2 that was sketched in figure 5.1b. The main objective is to test the control strategy presented in chapter 5 on a bluff body that is not wall-mounted. The inflow boundary condition, on both the upper and lower surfaces of the body, is a laminar Blasius boundary layer profile of thickness $\delta = 0.1$, superimposed with random perturbations to encourage transition to turbulence. The Reynolds number is set to $Re_h = 10^4$ to achieve a reasonable computational cost.

Unlike the backward-facing step flow, the flow over the D-shaped body possesses two separation lines at the upper and lower trailing edges, leading to an upper and a lower shear layer which interact. This interaction causes an absolute wake instability that initially develops in the far wake when the flow is started and then gradually extends upstream [57]. The absolute instability generates shedding of large vortices, leading to the von-Kármán vortex street. The shedding mechanism dominating the wake dynamics is essentially two-dimensional [6].

The control of the D-shaped bluff body for form-drag reduction has attracted considerable interest. Park et al. [107] used a passive device consisting of small tabs placed along the trailing edges. These managed to weaken the shedding by enhancing the three-dimensionality of the wake, leading to a drag decrease. A similar drag-reduction mechanism was performed via open-loop actuation by Kim et al. [73], with steady spanwise-sinusoidal jet forcing. Closed-loop control targeting synchronization of the two shear layers to delay the onset of shedding was presented by Henning et al. [57] and Pastoor et al. [108]. Stalnov et al. [130] used a

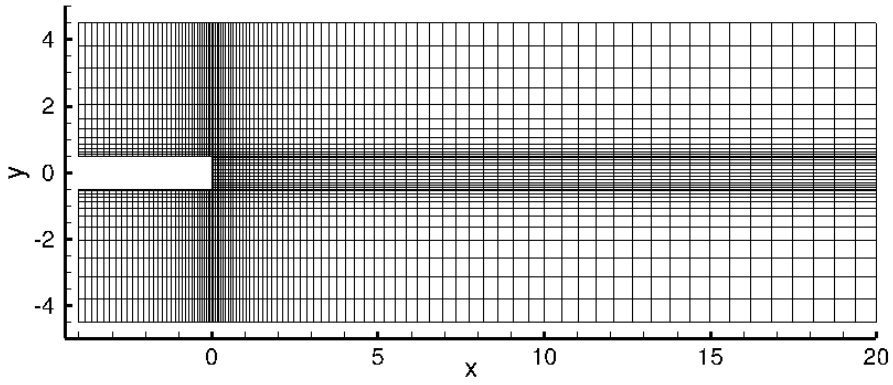


Figure 9.1: Two-dimensional slice of the nominal grid for $Re_h = 10^4$, with only one in every four nodes shown in each direction.

phase-locked loop to alter the frequency and phase of the shedding process, with a view to reducing unsteadiness in the wake.

In the following, we start by designing the computational mesh in §9.2, taking care to obtain adequate resolution. We then investigate the essential dynamics of the baseline flow in more detail in §9.3 and finally present the results of the system identification procedure and the feedback control in §9.4.

9.2 Grid resolution

Before investigating the baseline flow, we discuss the choice of the domain dimensions and the grid resolution. A nominal mesh is designed, comprising roughly 3.1 million nodes, with local refinement near walls and in the upper and lower actuation regions. A two-dimensional slice of the nominal computational grid is plotted in figure 9.1, showing only one in every four nodes in each direction for clarity. Note that the origin of the Cartesian reference frame is located at the centroid of the base, and the transverse node distribution is symmetric about the $y = 0$ axis. The nominal dimensions of the domain Ω_2, defined in figure 5.1, are $(L_i, L_x, L_y, L_z) = (4, 24, 9, 4)$.

Recall from the overview in chapter 5 that the top and bottom boundaries are set with free-slip conditions, whilst a periodic condition is imposed in the spanwise direction. Consequently, the flow is statistically homogeneous in the spanwise direction and the time averaging is coupled with a spanwise averaging to accelerate statistical convergence, as for the backward-facing step flow.

Grid	Δz^+	x_s	$(x_s - x_{s0})/x_{s0}$ (%)	St_d	$(St_d - St_{d0})/St_{d0}$ (%)
Nominal	24.9	0.995	0 %	0.243	0 %
Wide	24.9	0.950	-4.5 %	0.255	4.9 %
Fine_x	24.9	0.911	-8.4 %	0.251	3.3 %
Fine_z	12.4	0.895	-10.6 %	0.249	2.5 %

Table 9.1: Summary of grids tested, showing the stagnation point x_s in the time-averaged flow and the shedding frequency St_d obtained with four different grids.

Three other grids are tested —each designed by varying one main parameter with respect to the nominal grid— to verify that the nominal test case simulates the flow accurately. Table 9.1 lists all four grids. Compared to the nominal case, the *Wide* grid has a larger spanwise extent $L_z = 6$, the *Fine_x* grid is finer in the streamwise direction (downstream of the body) and the *Fine_z* grid has a spanwise spacing $\Delta z^+ = 12.4$, half that of the nominal case.

Table 9.1 also shows the solutions for the time-averaged length of the recirculation region x_s and the dominant frequency of the shedding mode, St_d. The first variable x_s is defined as the point along the axis $y = 0$ where the mean streamwise velocity $\overline{U}$ passes from a negative to a positive value. The dominant frequency of the shedding St_d is extracted from the base pressure sensor signal via spectral analysis. It can be seen that x_s is over-predicted by the nominal grid, whilst the shedding frequency St_d is mildly under-predicted. However, the differences remain small and satisfy us that the nominal grid is adequate to obtain an accurate solution of the D-shaped body flow. Figure 9.2 describes the distributions of computational nodes in the streamwise and transverse directions in wall units, as well as the maximum aspect ratios for all four grids.

9.3 Baseline flow

We now proceed to examine the main features of the baseline flow at $Re_h = 10^4$. Our main target in this section is to educe and discuss the large-scale coherent structures that dominate the wake, and to relate them to the base pressure force on the bluff body.

Figure 9.3 shows instantaneous isosurfaces of vorticity magnitude and pressure coefficient. The large-scale spanwise vortices, or rollers, that are shed downstream of the bluff body are evidenced by the high-vorticity surfaces in figure 9.3a. The vortical structures are arranged

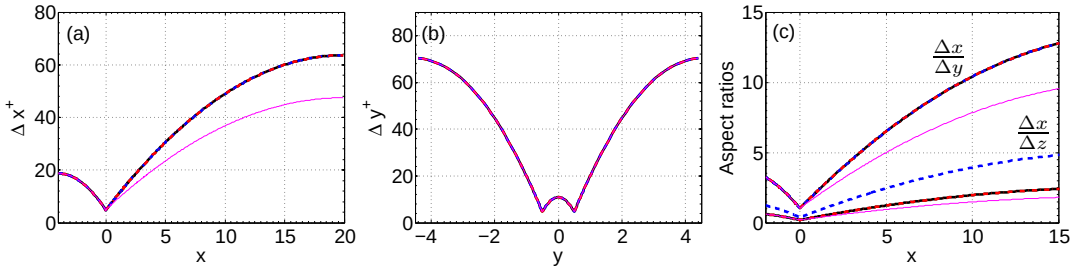


Figure 9.2: Distributions of computational nodes in the (a) streamwise and (b) transverse directions in wall units (based on friction velocity u_τ at the domain inlet). (c) Maximum aspect ratios. Nominal grid ——; *Fine_z* - - -; *Fine_x* ——; *Wide* -·-·-.

in the well-known von Kármán vortex street pattern. These vortices are produced by the alternate roll-up of the upper and lower shear layers. Gerrard [50] suggested that circulation from the separated shear layer feeds the growth of its attached vortex, until the latter is large enough to entrain the opposite shear layer. The oppositely signed vorticity disrupts the feeding of circulation and the large vortex is shed.

Isosurfaces of negative pressure coefficient $C_P = -0.1$, extracted from the same snapshot, are shown in figure 9.3b. It can be observed that the large-scale vortical structures resulting from the roll-up have a low pressure core. This can be predicted by taking the divergence of the momentum equation (3.2b) and then applying continuity. This manipulation leads to the pressure Poisson equation:

$$\frac{\partial^2 p}{\partial x_i^2} = -\frac{\partial u_i}{\partial x_j}\frac{\partial u_j}{\partial x_i} = Q \tag{9.1}$$

As discussed in the previous chapter, vortical regions correspond to a positive Q. From (9.1), one can infer that vortex cores hence correspond to local pressure minima. These vortical structures are essentially two-dimensional in the near wake, before breaking down further downstream.

Spectral analysis is performed to measure the dominant frequencies in the flow. The amplitude Fourier spectrum of the sensor signal (the base pressure fluctuations) is shown in figure 9.4a for the baseline flow. A large and narrow peak is present at $St_h \approx 0.25$, which corresponds to the shedding frequency. The vortex shedding mode clearly dominates the wake and, hence, the base pressure signal. The frequency of $St_d \approx 0.25$ agrees well with the literature; Henning et al. [57] and Pastoor et al. [108] report values of $St_d = 0.28$ and $St_d = 0.23$ respectively. The first harmonic is also observed.

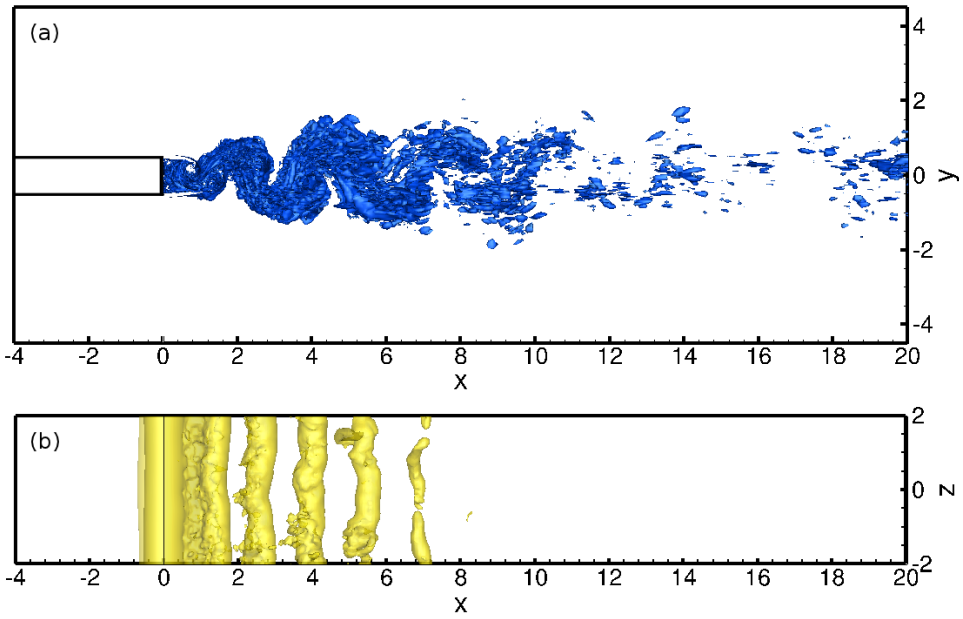


Figure 9.3: Instantaneous isosurfaces of (a) vorticity magnitude $|\omega| = 2.5$ in the xy plane and of (b) pressure coefficient $C_P = -0.1$ in the xz plane.

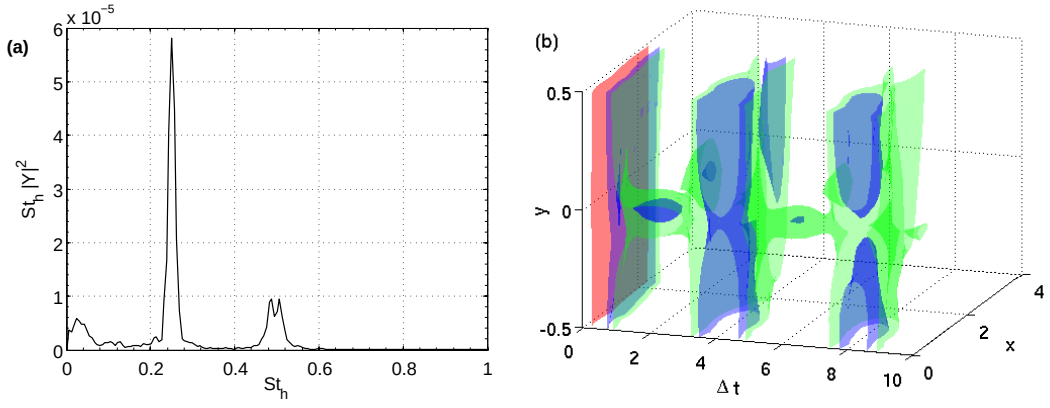


Figure 9.4: Characteristics of the dominant unsteady modes. (a) Base pressure amplitude spectra and (b) three-dimensional isosurfaces of the pressure autocorrelation $R_{pp}(\mathbf{x}, \Delta t)$. In (b), isosurfaces are plotted for three values of R_{pp}: 0.3 (green), 0.5 (blue) and 0.9 (red).

Finally, note the presence of a rather broad low-frequency peak, which is also present in the spectrum of Henning et al. [57], although it is not discussed. This low-frequency motion appears to be linked with a mechanism akin to the flapping mode described previously for the backward-facing step. A natural feedback loop exists between the shedding zone and the shear layers close to separation, leading to a pseudo-periodic expansion-contraction cycle of the recirculation region.

Three-dimensional isosurfaces of the autocorrelation coefficient $R_{pp}(\mathbf{x}, \Delta t)$, defined previously in (8.1), are plotted in figure 9.4b. The spatial region covered extends over $0 \leq x \leq 4$ and $-0.5 \leq y \leq 0.5$, for time delays $0 \leq \Delta t \leq 10$. As expected, the high correlation surface for $R_{pp} = 0.9$, coloured in red, is found for small time delays and does not vary significantly in the streamwise direction. The blue isosurfaces for $R_{pp} = 0.5$ appear periodically for time delays multiples of four, corresponding to the shedding period. The main blue structures narrow down progressively in the streamwise direction and extend up to $x \approx 1$, which corresponds to the length of the recirculation region x_s. The green $R_{pp} = 0.3$ isosurfaces show that some level of correlation remains up to large time delays in the region around the centre of the base.

In order to relate the shedding process with the base pressure, we examine the evolution of the base pressure distribution at different phases of the shedding process. Figure 9.5 shows instantaneous vorticity contours and the base distribution for four phases, $\phi = 0, \pi/2, \pi, 3\pi/2$, of the shedding cycle. The mutual entrainment between the two shear layers is well illustrated by the vorticity contours. The main point to observe is that the large vortices attached to the shear layers strongly influence the base pressure: their proximity to the base leads to a stronger footprint and hence a lower pressure. This suggests that delaying the roll-up of the shear layers is a means to increase the mean base pressure force.

9.4 System identification and feedback control

We then perform the system identification procedure presented in chapter 5 and carried out in chapters 6, 7 and 8. The open-loop frequency responses $G(i\omega)$ obtained are plotted in Bode diagrams in figure 9.6. As for the backward-facing step, the dynamic linearity assumption is examined by forcing with three different amplitudes $A_j = 0.1$, 0.2 and 0.3. Figure 9.6a shows the resulting frequency responses. Small differences in gain and phase are observed between the three curves, mainly near the shedding and flapping modes. These differences do not exceed

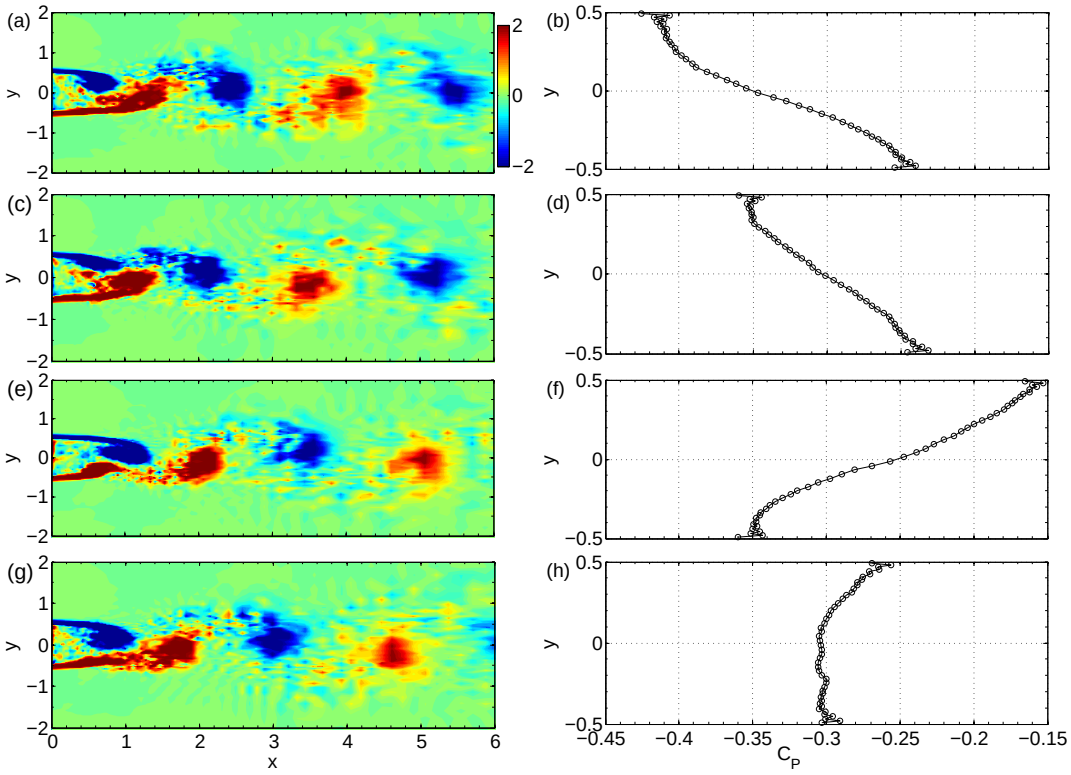


Figure 9.5: (a,c,e,g) Instantaneous vorticity ω_z contours and corresponding (b,d,f,h) base pressure C_P distributions, for four phases of the shedding cycle: (a,b) $\phi = 0$; (c,d) $\phi = \pi/2$; (e,f) $\phi = \pi$; (g,h) $\phi = 3\pi/2$.

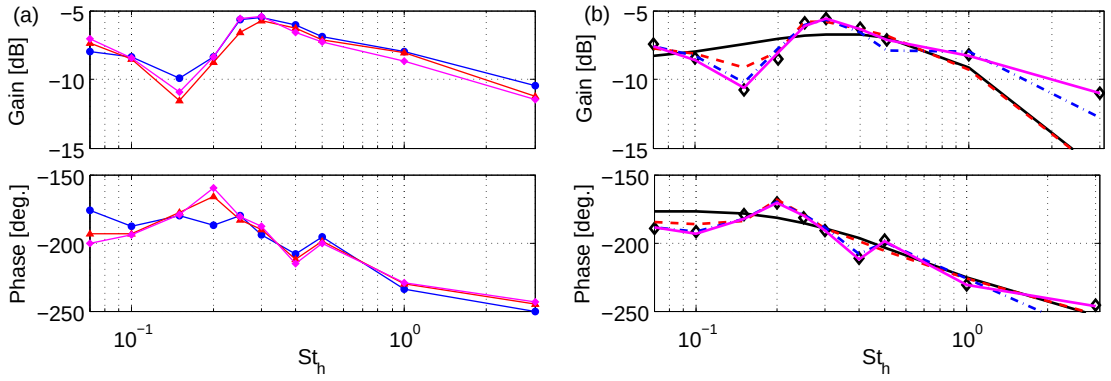


Figure 9.6: Bode plots of frequency responses. (a) Frequency responses for different forcing amplitudes: (●) $A_j = 0.1$, (▲) $A_j = 0.2$ and (♦) $A_j = 0.3$. (b) Frequency responses averaged over three amplitudes (◇). Least-square fits (via fitfrd) with (denominator) order 2 ——; order 4 - - - - ; order 6 ·····; order 8 ——. In each case the order of the numerator is one less than that of the denominator.

1.06dB for the gain and 27° for the phase. This reveals weak non-linearities, but the results from the backward-facing step case has shown us that these can be successfully mitigated by robust controllers.

An average over the three datasets is formed and shown in figure 9.6b. The transfer function gain reaches a local minimum at $St_h = 0.15$ and then peaks around the shedding mode frequency, before decreasing at a constant rate at high frequencies. The lines represent least-squares transfer function fits (of order 2, 4, 6 and 8) obtained via the MATLAB function fitfrd. The transfer function of order 8 provides an excellent fit to the frequency-domain data and is hence selected.

Using the open-loop plant model $G(i\omega)$ obtained from system identification, a robust controller is designed. Given that the baseline sensor spectrum is not very broadband, classical loop-shaping is used to shape the gain of the sensitivity function. The frequency response of the resulting controller K is shown in figure 9.7a, together with the open-loop transfer function $L = GK$ and the sensitivity function S. The controller K, which is only of second order, leads to a negative sensitivity gain (in dB) over a large band of frequencies up to $St_h \approx 0.7$. A small hump of positive $|S|$ for $0.7 \leq St_h \leq 3$ means that some high frequency disturbances will be amplified by the control system, but the natural disturbances within this range are very weak in this case.

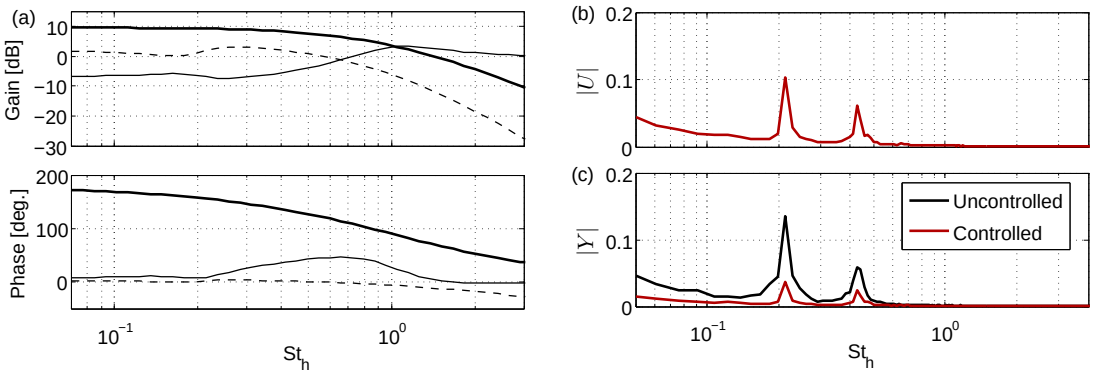


Figure 9.7: Frequency-domain characteristics of the closed loop system. (a) Frequency responses of the controller K (thick solid line), the open-loop function $L = GK$ (dashed line) and the sensitivity function S (thin solid line). Fourier spectra of the input and output control signals are shown in (b) and (c) respectively.

Figures 9.7b and c show amplitude spectra of the input and output control signals respectively. It can be observed that the controller successfully attenuates the fluctuations in the base pressure force. The control produces a concomitant 15% increase in the time-averaged base pressure, and hence manages to sensibly reduce the form-drag. As expected, the controller responds to the flow system and hence operates mainly at the most energetic frequencies of the baseline flow.

Figure 9.8 shows streamfunction contours for the time-averaged velocity field, comparing the baseline and closed-loop controlled flows. The wake is enlarged by the controller, hence delaying the roll-up of the shear layers and the vortex shedding. As a result, the large vortices with low-pressure cores have a lesser impact on the base and the time-averaged base pressure force increases. This result agrees with the effects observed previously in the literature with closed-loop controllers aiming to reduce form-drag on a D-shaped body (Henning et al. [57]; Pastoor et al. [108]) or to reduce unsteadiness in the wake (Stalnov et al. [130]).

9.5 Summary

The D-shaped body flow in domain Ω_2 was investigated at $Re_h = 10^4$ with a perturbed laminar inflow. After reviewing previous control attempts for the D-shaped body and examining the main features of the baseline flow, we test the control strategy that was first applied on the

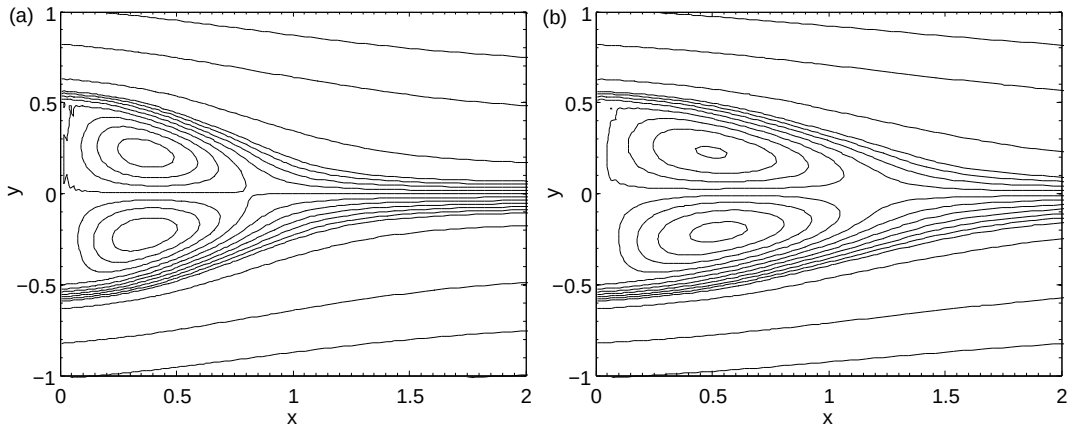


Figure 9.8: Line contours of time-averaged streamfunction Ψ for the (a) baseline and (b) feedback controlled flows.

backward-facing step flow in the previous chapters. It is found that linear system identification and control, combined with the assumption about the link between the base pressure force fluctuations and mean, are sufficient to produce a sensible increase in the time-averaged base pressure force (15% with a second order controller) and hence reduce form-drag.

The present control strategy applied to a bluff body flow relied solely on information sensed from the base; i.e. no information or sophisticated modelling of the velocity or pressure fields in the wake are necessary. In addition, it was shown that very low-order control models (derived from system identification and the control synthesis) can lead to successful control. Therefore a control system relying on the present strategy may be implemented in real-time at a low-cost.

Chapter 10

Conclusions & outlook

This brings us to the conclusion of this work. We summarize the main results and contributions of this thesis. Subsequently, we give some suggestions for future work.

10.1 Summary

This thesis has focused on applying linear system identification and feedback control tools to reduce form-drag on 2D bluff bodies with a blunt trailing-edge. At the heart of this work lies an interrogation about the applicability of such black-box linear methods to the complex, non-linear, non time-invariant and multi-scale problem of turbulent shear layers and wakes. Fortunately, the answer seems to be positive, albeit with a few words of caution.

Firstly, this work has only considered bluff body flows homogeneous in the spanwise direction. These are in part dominated by large-scale coherent spanwise structures that are à priori easier to analyze than broadband turbulence. Secondly, transfer function models are strongly dependent on the configuration of the actuation and the sensing. Non-observable modes can not be captured which leads to a restricted view. Some important flow mechanisms may be hidden from the plant model. Thus, unexpected results may arise in regions of the flow away from the sensor. Finally, the issue of optimization remains an open-ended question. Linear control theory offers a great array of optimization tools. However, it may be that linear black-box models are better suited to robust methods which can mitigate large uncertainty. With these words of caution in mind, it seems that the modelling and control strategy used in this thesis offers rich opportunities for control in a practical, real-world setting.

We have considered two distinct bluff bodies, a wall-mounted volume with a sharp trailing

edge reducing to a backward-facing step and a D-shaped bluff body. The major part of this research effort was focused on the backward-facing step. A 2D laminar flow and a 3D turbulent flow at two Reynolds numbers were studied. For all flows, the investigation was broken down into three main parts: study of the baseline flow, system identification to model the response of the flow to actuation, and control synthesis. The control strategy was based on the premise that reducing the pressure fluctuations on the base causes an increase in the mean pressure. This approach proved successful for all the cases investigated.

The flow mechanisms involved were examined along the way. In the case of the backward-facing step, we concluded that the increase in base pressure obtained is associated with a stabilization of the natural modes of motion dominating the flow. Damping of the Kelvin-Helmholtz instability in the shear layer leads to reduced entrainment and dissipation, hence also pushing the unsteady reattachment and large-scale (low-pressure) structures away from the base. The natural feedback mechanism between the reattachment and the separation regions that causes the low-frequency flapping motion is in turn impeded. Smaller scales of motion are also affected in several ways, which calls for further study.

For the D-shaped body, a similar perspective showed that the controller strives to delay the shedding. This reduces the trace of low pressure structures on the base, as well as decreasing the momentum transferred to the recirculation bubble.

10.2 Outlook

The thesis presented above touches on various fields, including fluid dynamics, hydrodynamic stability, control theory and numerical methods. Such a combination reflects the challenging demands of modern flow control problems. As Bewley [8] elegantly stated, there is a need for a Renaissance approach, to develop the integration between the different disciplines involved for flow control.

There are numerous interesting directions to follow from here. We briefly allude to three ideas that seem promising. These are based on individual improvements to the building blocks of the control strategy. As highlighted above, a harmonious integration of the different blocks must be kept in mind.

The dynamics of the flow can be decomposed into modes. For simple bluff body flows, it seems possible to isolate a small number of natural modes that dominate the flow and its

response to small perturbations. An important issue that arises is that of defining the role of those modes more precisely and assessing methods to incorporate them in the plant model and control design, without loosing the advantages of linear data-based methods. Surely, it seems that models including such information can attain superior performance compared to black-box models. It remains to ensure that the cost penalty is viable for complex flows. In addition, the dominance of these modes might be challenged in more complex geometries with roundings and protrusions causing stronger turbulent fluctuations and many small separated flow regions.

Secondly, it would be interesting to examine whether the control strategy presented can be applied to 3D bluff bodies. The work of Flinois [42] is, in part, geared in this direction. Also, more complex geometries should be considered. These may include elements characteristic of specific applications like road vehicles, where features such as the gap underneath the body, the moving road, the effect of adjacent vehicles and sidewinds are all expected to influence the aerodynamic loads.

Finally, there is scope for more sophisticated control methods. Some examples include multi-input multi-output (MIMO) control and adaptive control that would allow the slow part of the dynamics to be re-evaluated online and used to update the plant model and the controller in real-time. Also, state-space methods combined with optimization tools present an interesting potential. Optimal control tools should be envisaged, since it is in fact the net energy gain, rather than the drag reduction, that is relevant. Such tools would allow the minimization of the actuation effort to be incorporated in the controller design process.

Bibliography

[1] E. W. Adams and J. P. Johnston. Effects of the separating shear layer on the reattachment flow structure. Part 2: Reattachment length and wall shear stress. *Exp. Fluids*, 6:493–499, 1988.

[2] S. R. Ahmed. Computational Fluid Dynamics. In W.-H. Hucho, editor, *Aerodynamics of Road Vehicles*. Society of Automotive Engineers, Inc., 1998.

[3] J. D. Anderson. *Fundamentals of aerodynamics*. McGraw Hill, 2001.

[4] E. Aram, R. Mittal, and L. Cattafesta. Simple representations of zero-net-mass-flux jets in grazing flow for flow-control simulations. *Int. J. Flow Control*, 2(2):109–125, 2010.

[5] B. F. Armaly, F. Durst, J. C. F. Pereira, and B. Schönung. Experimental and theoretical investigation of backward-facing step flow. *J. Fluid Mech.*, 127:473–496, 1983.

[6] P. W. Bearman. Vortex shedding from oscillating bluff bodies. *Ann. Rev. Fluid Mech.*, 16:195–222, 1984.

[7] P. Beaudan and P. Moin. Numerical experiments on the flow past a circular cylinder at sub-critical Reynolds number. Technical report, Department of Mechanical Engineering, Stanford, 1994.

[8] T. R. Bewley. Flow control: new challenges for a new Rennaissance. *Prog. Aerosp. Sci.*, 37:21–58, 2001.

[9] S. Bhattacharjee, B. Scheelke, and T. R. Troutt. Modifications of vortex interactions in a reattaching separated flow. *AIAA J.*, 24(4):623–629, 1986.

[10] P. Bradshaw and F. Y. F. Wong. The reattachment and relaxation of a turbulent shear layer. *J. Fluid Mech.*, 52:113–135, 1972.

[11] M. Breuer. Large eddy simulation of the subcritical flow past a circular cylinder: numerical and modeling aspects. *Int. J. Numer. Meth. Fluids*, 28:1281–1302, 1998.

[12] E. Brosco. Experimental investigation on separation control by high frequency forcing. Master's thesis, La Sapienza, University of Rome, 2011.

[13] F. K. Browand and C. M. Ho. The mixing layer: an example of quasi two-dimensional turbulence. *J. Méc. Théor. Appl.*, pages 99–120, 1983.

[14] F. K. Browand and T. R. Troutt. The turbulent mixing layer: geometry of large vortices. *J. Fluid Mech.*, 158:489–509, 1985.

[15] I. P. Castro and A. Haque. The structure of a turbulent shear layer bounding a separation region. *J. Fluid Mech.*, 179:439–468, 1987.

[16] L. N. Cattafesta and M. Sheplak. Actuators for active flow control. *Annu. Rev. Fluid Mech.*, 43:247–272, 2011.

[17] L. N. Cattafesta, Q. Song, D. R. Williams, C. W. Rowley, and F. S. Alvi. Active control of flow-induced cavity oscillations. *Prog. Aerosp. Sci.*, 44:479–502, 2008.

[18] N. J. Cherry, R. Hillier, and M.E.M.P. Latour. Unsteady measurements in a separated and reattaching flow. *J. Fluid Mech.*, 144:13–46, 1984.

[19] H. Choi, W-P Jeon, and J. Kim. Control of flow over a bluff body. *Annu. Rev. Fluid Mech.*, 40:113–139, 2008.

[20] A. J. Chorin. Numerical solution of the Navier-Stokes equations. *Math. Comput.*, 22(104):745–762, 1968.

[21] K. B. Chun and H. J. Sung. Control of turbulent separated flow over a backward-facing step by local forcing. *Exp. Fluids*, 25:133–142, 1996.

[22] K. B. Chun and H. J. Sung. Visualization of a locally-forced separated flow over a backward-facing step. *Exp. Fluids*, 25:133–142, 1998.

[23] K. Cohen, S. Siegel, and T. McLaughlin. A heuristic approach to effective sensor placement for modeling of a cylinder wake. *Comput. fluids*, 35:103–120, 2006.

[24] D. Coles. The law of the wake in the turbulent boundary layer. *J. Fluid Mech.*, 1:191–226, 1956.

[25] S. S. Collis, R. D. Joslin, A. Seifert, and V. Theofilis. Issues in active flow control: theory, control, simulation, and experiment. *Prog. Aerosp. Sci.*, 40:237–289, 2004.

[26] L. Cortelezzi and J. L. Speyer. Robust reduced-order controller of laminar boundary layer transitions. *Phys. Rev. E*, 58(2):1906–1910, 1998.

[27] M.J.P. Cullen and A. R. Brown. Large eddy simulation of the atmosphere on various scales. *Phil. Trans. R. Soc. A*, 367:2947–2956, 2009.

[28] J. A. Dahan, A. S. Morgans, and S. Lardeau. Feedback control for form-drag reduction on a bluff body with a blunt trailing edge. *J. Fluid Mech.*, 704:360–387, 2012.

[29] J. Dandois, E. Garnier, and P. Sagaut. Numerical simulation of active separation control by a synthetic jet. *J. Fluid Mech.*, 574:25–58, 2007.

[30] V. de Brederode and P. Bradshaw. Three-dimensional flow in nominally two-dimensional separation bubbles. Technical report, Imperial College, Dept. of Aeronautics, 1972.

[31] J. W. Deardorff. A numerical study of three-dimensional turbulent channel flow at large Reynolds numbers. *J. Fluid Mech.*, 41:453–480, 1970.

[32] A. Dejoan and M. A. Leschziner. Large eddy simulation of periodically perturbed separated flow over a backward-facing step. *Int. J. Heat Fluid Fl.*, 25:581–592, 2004.

[33] A. P. Dowling and A. S. Morgans. Feedback control of combustion oscillations. *Annu. Rev. Fluid Mech.*, 37:151–182, 2005.

[34] D. M. Driver and H. L. Seegmiller. Features of a reattaching turbulent shear layer in divergent channel flow. *AIAA J.*, 23(2):163–171, 1985.

[35] D. M. Driver, H. L. Seegmiller, and J. G. Marvin. Time-dependent behavior of a reattaching shear layer. *AIAA J.*, 25(7):914–919, 1987.

[36] S. J. Eastwood, P. G. Tucker, H. Xia, and C. Klostermeier. Developing large eddy simulation for turbomachine applications. *Phil. Trans. R. Soc. A*, 367:2999–3013, 2009.

[37] J. K. Eaton and J. P. Johnston. Turbulent flow reattachment: an experimental study of the flow and structure behind a backward-facing step. Technical Report MD-39, Thermoscience Division, Dept. of Mechanical Eng., Stanford University, 1980.

[38] J. K. Eaton and J. P. Johnston. A review of research on subsonic turbulent flow reattachment. *AIAA J.*, 19(9):1093–1100, 1981.

[39] R. J. Englar. Development of pneumatic aerodynamic devices to improve the performance, economics, and safety of heavy vehicles. *SAE Technical Paper Series*, 2000-01-2208, 2000.

[40] B. F. Farrell and P. J. Ioannou. Turbulence suppression by active control. *Phys. Fluids*, 8:1257–1268, 1996.

[41] G. M. Fishpool and M. A. Leschziner. Stability bounds for explicit fractional-step schemes for the Navier-Stokes equations at high Reynolds number. *Comput. Fluids*, 38:1289–1298, 2009.

[42] T. L. B. Flinois. Feedback Control on Three-Dimensional Blunt Body Wakes For Road-Vehicle Form Drag Reduction. Technical report, Imperial College London, 2012.

[43] R. Friedrich and M. Arnal. Analysing turbulent backward-facing step flow with the lowpass-filtered Navier-Stokes equations. *J. Wind Eng. Ind. Aerod.*, 35:101–128, 1990.

[44] J. Fröhlich, C. P. Mellen, W. Rodi, L. Temmerman, and M. A. Leschziner. Highly resolved large-eddy simulation of separated flow in a channel with streamwise periodic constrictions. *J. Fluid Mech.*, 526:19–66, 2005.

[45] J. Fröhlich and W. Rodi. LES of the flow around a circular cylinder of finite height. *Int. J. Heat Fluid Fl.*, 25:537–548, 2004.

[46] M. Gad-el Hak. *Flow Control - Passive, active and reactive flow management.* Cambridge University Press, The Edinburgh Building, Cambridge CN2 2RU, UK, 2000.

[47] M. Gad-el Hak, A. Pollard, and J.-P. Bonnet. *Flow Control, Fundamentals and Practices.* Springer-Verlag, 1998.

[48] A. Gelb and W. E. Vander Velde. *Multiple-input describing functions and nonlinear system design.* McGraw-Hill, 1968.

[49] M. Germano, U. Piomelli, P. Moin, and W. H. Cabot. A dynamic subgrid-scale eddy viscosity model. *Phys. Fluids A-Fluid*, 3:1760–1765, 1991.

[50] J. H. Gerrard. The mechanics of the formation region of vortices behind bluff bodies. *J. Fluid Mech.*, 25(2):401–413, 1966.

[51] S. Ghosal and P. Moin. The basic equations for the large eddy simulation of turbulent flows in complex geometry. *J. Comput. Phys.*, 118:24–37, 1995.

[52] G. Haller. An objective definition of a vortex. *J. Fluid Mech.*, 525:1–26, 2005.

[53] M. A. Z. Hasan. The flow over a backward-facing step under controlled perturbation: laminar separation. *J. Fluid Mech.*, 238:73–96, 1992.

[54] A. F. Heenan and J. F. Morrison. Passive control of pressure fluctuations generated by separated flow. *AIAA J.*, 36(6):1014–1022, 1998.

[55] H. Hemida, S. Krajnović, and L. Davidson. Large-eddy simulation of the flow around a simplified high speed train under the influence of a cross-wind. In *Proc. 17th AIAA Computational Dynamics Conference, Toronto, Ontario, Canada*, 2005.

[56] L. Henning and R. King. Drag reduction by closed-loop control of a separated flow over a bluff body with a blunt trailing edge. In *Proceedings of the 44th IEEE Conference on Decision and Control, and the European Control Conference 2005*, pages 494–499, 2005.

[57] L. Henning and R. King. Robust multivariable closed-loop control of a turbulent backward-facing step flow. *J. Aircraft*, 44(1):201–208, 2007.

[58] A. Hervé, D. Sipp, P. J. Schmid, and M. Samuelides. A physics-based approach to flow control using system identification. *J. Fluid Mech.*, 702:26–58, 2012.

[59] C. Hirsch. *Numerical computation of internal and external flows.* Butterworth-Heinemann, 2nd edition, 2007.

[60] P. Holmes, J. L. Lumley, and G. Berkooz. *Turbulence, Coherent Structures, Dynamical Systems and Symmetry.* Cambridge University Press, Cambridge, UK, 1996.

[61] H. T. Huang and H. E. Fiedler. A DPIV study of a starting flow downstream of a backward-facing step. *Exp. Fluids*, 23:395–404, 1997.

[62] S.-C. Huang and J. Kim. Control and system identification of a separated flow. *Phys. Fluids*, 20:101509, 2008.

[63] L. M. Hudy, A. Naguib, and W. M. Humphreys. Stochastic estimation of a separated-flow field using wall-pressure-array measurements. *Phys. Fluids*, 19:024103, 2007.

[64] L. M. Hudy, A. M. Naguib, and W. M. Humphreys. Wall-pressure-array measurements beneath a separating/reattaching flow region. *Phys. Fluids*, 15(3):706–716, 2003.

[65] J. C. R. Hunt, A. A. Wray, and P. Moin. Eddies, streams, and convergence zones in turbulent flows. Technical report, Center for Turbulence Research, 1988.

[66] S. J. Illingworth. *Feedback control of oscillations in combustion and cavity flows.* PhD thesis, Magdalene College, University of Cambridge, 2009.

[67] S. J. Illingworth, A. S. Morgans, and C. W. Rowley. Feedback control of flow resonances using balanced reduced-order models. *J. Sound Vib.*, 330:1567–1581, 2011.

[68] O. L. R. Jacobs. *Introduction to control theory.* Oxford University Press, New York, 1993.

[69] J. Jimenez, S. Hoyas, M. P. Simens, and Y. Mizuno. Turbulent boundary layers and channels at moderate Reynolds numbers. *J. Fluid Mech.*, 657:335–360, 2010.

[70] B. L. Jones, E. C. Kerrigan, J. F. Morrison, and T. A. Zaki. Flow estimation of boundary layers using DNS-based wall shear information. *Int. J. Control*, 84(8):1310–1325, 2011.

[71] J-N Juang and R. S. Pappa. An eigensystem realization algorithm for modal parameter identification and model reduction. *J. Guid. Cont. Dyn.*, 8(5):620–627, 1985.

[72] J. Kim and T. R. Bewley. A linear systems approach to flow control. *Annu. Rev. Fluid Mech.*, 39:383–417, 2007.

[73] J. Kim, S. Hahn, J. Kim, D. Lee, J. Choi, W. Jeon, and H. Choi. Active control of turbulent flow over a model vehicle for drag reduction. *J. Turb.*, 5(019), 2004.

[74] K. Kim, M. Kerr, A. Beskok, and S. Jayasuriya. Frequency-domain based feedback control of flow separation using synthetic jets. In *Proceedings of the 2006 American Control Conference*, pages 5318–5323, 2006.

[75] S. Kim, H. Choi, and J. Y. Yoo. Effect of local forcing on backward-facing step flow with laminar separation. *J. Turb.*, 8(6):1–23, 2007.

[76] R. King. Optimal closed-loop approaches in flow control. In *Reduced-order modelling for flow control*. SpringerWienNewYork, 2011.

[77] M. Kiya and K. Sasaki. Structure of large-scale vortices and unsteady reverse flow in the reattaching zone of a turbulent separation bubble. *J. Fluid Mech.*, 154:463–491, 1985.

[78] M. Kiya, M. Shimizu, and O. Mochizuki. Sinusoidal forcing of a turbulent separation bubble. *J. Fluid Mech.*, 342:119–139, 1997.

[79] S. Krajnović. Large eddy simulation of the flow over a three-dimensional hill. *Flow Turbul. Combust.*, 81:189–204, 2008.

[80] S. Krajnović. Large eddy simulation of flows around ground vehicles and bluff bodies. *Phil. Trans. R. Soc. A*, 367:2917–2930, 2009.

[81] S. Krajnović and L. Davidson. Numerical study of the flow around a bus-shaped body. *J. Fluid Eng.*, 125(3):500–509, 2003.

[82] S. Krajnović and L. Davidson. Flow around a simplified car, part 1: large eddy simulation. *J. Fluids Eng.*, 127:907–918, 2005.

[83] A. H. M. Kwong and A. P. Dowling. Active boundary-layer control in diffusers. *AIAA J.*, 32(12):2409–2414, 1994.

[84] S. Lall, J. E. Marsden, and S. Glavaški. Empirical model reduction of controlled nonlinear systems. In *Proceedings of the IFAC World Congress*, pages 473–478, 1999.

[85] S. Lardeau, M. Leschziner, and T. Zaki. Large Eddy Simulation of Transitional Separated Flow over a Flat Plate and a Compressor Blade. *Flow Turbul. Combust.*, 88:19–44, 2012.

[86] H. Le, P. Moin, and J. Kim. Direct numerical simulation of turbulent flow over a backward-facing step. *J. Fluid Mech.*, 330:349–374, 1997.

[87] I. Lee and H. J. Sung. Multiple-arrayed pressure measurement for investigation of the unsteady flow structure of a reattaching shear layer. *J. Fluid Mech.*, 463:377–402, 2002.

[88] K. H. Lee, L. Cortelezzi, J. Kim, and J. Speyer. Application of reduced-order controller to turbulent flows for drag reduction. *Phys. Fluids*, 13(5):1321–1330, 2001.

[89] A. Leonard. Energy cascade in large-eddy simulations of turbulent fluid flows. *Avd. Geophys.*, 18A:237–248, 1974.

[90] M. A. Leschziner and S. Lardeau. Simulation of slot and round synthetic jets in the context of boundary layer separation. *Phil. Trans. R. Soc. A*, 369:1495–1512, 2011.

[91] Y. Z. Liu, W. Kang, and H. J. Sung. Assessment of the organization of a turbulent separated and reattaching flow by measuring wall pressure fluctuations. *Exp. Fluids*, 38:485–493, 2005.

[92] L. Ljung. *Matlab System Identification Toolbox, User's Guide*. The Mathworks Inc., USA, 1997.

[93] L. Ljung. *System Identification: Theory for the User*. Prentice Hall, Upper Saddle River, NJ, 1999.

[94] T. S. Lund, X. Wu, and K. D. Squires. Generation of turbulent inflow data for spatially-developing boundary layer simulations. *J. Comput. Phys.*, 140:233–258, 1998.

[95] Z. Ma, S. Ahuja, and C. W. Rowley. Reduced order models for control of fluids using the eigensystem realization algorithm. *Theor. Comput. Fluid Dyn.*, 25:233–247, 2009.

[96] D. G. Mabey. Analysis and correlation of data on pressure fluctuations in separated flow. *J. Aircraft*, 9(9):642–645, 1972.

[97] D. C. McFarlane and K. Glover. *Robust controller design using normalized coprime factor plant descriptions*. Springer-Verlag, 1989.

[98] M. McGuiness. *Flow with a separation bubble–steady and unsteady aspects*. PhD thesis, Cambridge University, 1978.

[99] V. J. Modi, S. St. Hill, and T. Yokomizo. Drag reduction of trucks through boundary-layer control. *J. Wind Eng. Ind. Aerod.*, 54/55:583–594, 1995.

[100] B. C. Moore. Principal component analysis in linear systems: controllability, observability, and model reduction. *IEEE Trans. Automat. Contr.*, 26(1):17–32, 1981.

[101] A. S. Morgans and A. P. Dowling. Low-order modeling for transonic helicopter noise. *AIAA J.*, 42(12):2416–2428, 2004.

[102] S. Murakami, A. Mochida, and H. Kazuki. Three-dimensional numerical simulation of air flow around a cubic model by means of large-eddy simulation. *J. Wind Eng. Ind. Aerod.*, 25:291–305, 1987.

[103] A. S. Neto, D. Grand, O. Métais, and M. Lesieur. A numerical investigation of the coherent vortices in turbulence behind a backward-facing step. *J. Fluid Mech.*, 256:1–25, 1993.

[104] J. Neumann. On time-dependent behaviour of controlled turbulent flow with separation and reattachment. *Proc. Appl. Math. Mech.*, 3:44–47, 2003.

[105] F. Nicoud and F. Ducros. Subgrid-scale stress modelling based on the square of the velocity gradient tensor. *Flow. Turbul. Combust.*, 62:183,200, 1999.

[106] H. Nyquist. Regeneration Theory. *Bell System Tech. J.*, 11(1):126–147, 1932.

[107] H. Park, D. Lee, W-P Jeon, S. Hahn, J. Kim, J. Kim, J. Choi, and H. Choi. Drag reduction in flow over a two-dimensional bluff body with a blunt trailing edge using a new passive device. *J. Fluid Mech.*, 563:389–414, 2006.

[108] M. Pastoor, L. Henning, B. R. Noack, R. King, and G. Tadmor. Feedback shear layer control for bluff body drag reduction. *J. Fluid Mech.*, 608:161–196, 2008.

[109] M. Pastoor, R. King, B. R. Noack, A. Dillmann, and G. Tadmor. Model-based coherent-structure control of turbulent shear flows using low-dimensional vortex models. In *33rd AIAA Fluids Conference and Exhibit*, 2003. Paper 2003-4261.

[110] A. Qubain. *Active Control of a Turbulent Bluff Body Wake*. PhD thesis, Imperial College London, 2009.

[111] European Commission Report. Results of the review of the community strategy to reduce CO_2 emissions from passenger cars and light commercial vehicles. Technical report, European Commission, 2007.

[112] C. M. Rhie and W. L. Chow. Numerical Study of the Turbulent Flow Past an Airfoil with Trailing Edge Separation. *AIAA J.*, 21(11):1525–1532, 1983.

[113] W. Rodi, J. H. Ferziger, M. Breuer, and M. Pourquié. Status of large eddy simulation: results of a workshop. *J. Fluids Eng.*, 119:248–262, 1997.

[114] F.W Roos and J.T. Kegelman. Control of coherent structures in reattaching laminar and turbulent shear layers. *AIAA J.*, 24(12):1956–1963, 1986.

[115] A. Roshko. On the drag and shedding frequency of two-dimensional bluff bodies. Technical report, National Advisory Committee for Aeronautics, 1954.

[116] A. Roshko. Perspectives on bluff body aerodynamics. *J. Wind Eng. Ind. Aerod.*, 49:79–100, 1993.

[117] A. Roshko and J. C. Lau. Some observations on transition and reattachment of a free shear layer in incompressible flows. In *Proceedings of 1965 Heat Transfer and Fluid Mech. Inst*, 1965.

[118] C. W. Rowley and V. Juttijudata. Model-based control and estimation of cavity flow oscillations. In *44th IEEE Conference on Decision and Control & European Control Conference*, pages 512–517, 2005.

[119] R. Ruderich and H. H. Fernholz. An experimental investigation of a turbulent shear flow with separation, reverse flow, and reattachment. *J. Fluid Mech.*, 163:283–322, 1986.

[120] P. Sagaut. *Large eddy simulation for incompressible flows*. Springer-Verlag, third edition, 2006.

[121] H. Schlichting and K. Gersten. *Boundary Layer Theory*. Springer, 8th edition, 2000.

[122] U. Schumann. Subgrid scale model for finite difference simulations of turbulent flows in plane channels and annuli. *J. Comput. Phys.*, 18:376–404, 1975.

[123] A. Seifert, O. Stalnov, D. Sperber, G. Arwatz, V. Palei, S. David, I. Dayan, and I. Fono. Large trucks drag reduction using active flow control. In Fred Browand, Rose McCallen, and James Ross, editors, *The Aerodynamics of Heavy Vehicles II: Trucks, Buses, and Trains*, volume 41 of *Lecture Notes in Applied and Computational Mechanics*, pages 115–133. Springer Berlin / Heidelberg, 2009.

[124] S. Siegel, K. Cohen, and T. McLaughlin. Numerical simulations of a feedback-controlled circular cylinder wake. *AIAA J.*, 44(6):1266–1276, 2006.

[125] L. W. Sigurdson. The structure and control of a turbulent reattaching flow. *J. Fluid Mech.*, 298:139–165, 1995.

[126] R. L. Simpson. Turbulent boundary-layer separation. *Annu. Rev. Fluid Mech.*, 21:205–234, 1989.

[127] J. Smagorinsky. General circulation experiments with the primitive equations. I. The basic experiment. *Mon. Weather Rev.*, 91(3):99–164, 1963.

[128] G. Sovran, T. Morel, and W. T. Mason, editors. *Aerodynamic drag mechanisms of bluff bodies and road vehicles.* Plenum Press, 1978.

[129] P.G. Spazzini, G. Iuso, M. Onorato, N. Zurlo, and G. M. Di Cicca. Unsteady behavior of back-facing step flow. *Exp. Fluids*, 30:551–561, 2001.

[130] O. Stalnov, I. Fono, and A. Seifert. Closed-loop bluff-body wake stabilization via fluidic excitation. *Theor. Comput. Fluid Dyn.*, 25:209–219, 2011.

[131] G. R. Tabor and M. H. Baba-Ahmadi. Inlet conditions for large eddy simulation. *Comput. Fluids*, 39:553–567, 2010.

[132] M. Tanner. A method for reducing the base drag of wings with blunt trailing edge. *Aeronaut. Quart.*, 23:15–23, 1972.

[133] L. Temmerman. *Large Eddy Simulation of separating flows from curved surfaces.* PhD thesis, University of London, 2004.

[134] L. Temmerman, M. A. Leschziner, C. P. Mellen, and J. Fröhlich. Investigation of wall-function approximations and subgrid-scale models in large eddy simulation of separated flow in a channel with streamwise periodic constrictions. *Int. J. Heat Fluid Fl.*, 24:157–180, 2003.

[135] E. Touber and M. A. Leschziner. Near-wall streak modification by spanwise oscillatory wall motion and drag-reduction mechanisms. *J. Fluid Mech.*, 693:150–200, 2012.

[136] T. R. Troutt, B. Scheelke, and T. R. Norman. Organized structures in a reattaching separated flow field. *J. Fluid Mech.*, 143:413–427, 1984.

[137] P. G. Tucker and S. Lardeau. Applied large eddy simulation. *Phil. Trans. R. Soc. A*, 367:2809–2818, 2009.

[138] V. Uruba, P. Jonáš, and O. Mazur. Control of a channel-flow behind a backward-facing step by suction/blowing. *Int. J. Heat Fluid Fl.*, 28:665–672, 2007.

[139] Y. Utturkar, R. Mittal, P. Rampunggoon, and L. Cattafesta. Sensitivity of synthetic jets to the design of the jet cavity. In *40th AIAA Aerospace sciences meeting and exhibit*, 2002.

[140] G. M. C. Van Raemdonck. *Design of Low Drag Bluff Road Vehicles*. PhD thesis, Technische Universiteit Delft, 2012.

[141] B. Vukasinovic, Z. Rusak, and A. Glezer. Dissipative small-scale actuation of a turbulent shear layer. *J. Fluid Mech.*, 656:51–81, 2010.

[142] B. Wasistho and K. D. Squires. Prediction of turbulent separation over a backward-facing smooth ramp. *J. Turb.*, 6, 2005.

[143] D. Wee, T. Yi, A. Annaswamy, and A. F. Ghoniem. Self-sustained oscillations and vortex shedding in backward-facing step flows: Simulation and linear instability analysis. *Phys. Fluids*, 16(9):3361–3373, 2004.

[144] H. Werner and H. Wengle. Large-eddy simulation of turbulent flow over a square rib in a channel. In *Advances in Turbulence II*, pages 418–423. Springer-Verlag, 1989.

[145] F. M. White. *Viscous fluid flow*. McGraw Hill, 3rd edition, 2005.

[146] C. J. Wood. Visualization of an incompressible wake with base bleed. *J. Fluid Mech.*, 29(2):259–272, 1967.

[147] S. Yoshioka, S. Obi, and S. Masuda. Organized vortex motion in periodically perturbed turbulent separated flow over a backward-facing step. *Int. J. Heat Fluid Fl.*, 22:301–307, 2001.

[148] K. Zhou, J. C. Doyle, and K. Glover. *Robust and optimal control*. Prentice Hall, Englewood Cliffs, New Jersey, 1996.

[149] M. Zhu, A. P. Dowling, and K. N. C. Bray. Flame Transfer Function Calculations for Combustion Oscillations. In *ASME Turbo Expo*, 2001. 2001-GT-0374.